Time-Resolved Spectroscopy of Transition Metal Complexes

Dissertation
zur
Erlangung des Doktorgrades (Dr. rer. nat.)
der
Mathematisch-Naturwissenschaftlichen Fakultät
der
Rheinischen Friedrich-Wilhelms-Universität Bonn

vorgelegt von
Tobias Unruh
aus Euskirchen

Bonn, 2024

Angefertigt mit Genehmigung
der Mathematisch-Naturwissenschaftlichen Fakultät der
Rheinischen Friedrich-Wilhelms-Universität Bonn

1. Gutachter: Prof. Dr. Peter Vöhringer
2. Gutachter: Prof. Dr. Alexander C. Filippou

Tag der Promotion: 08. Januar 2024
Erscheinungsjahr: 2024

Wir müssen wissen — wir werden wissen

David Hilbert

Ich versichere, dass ich die vorliegende Arbeit unter Einhaltung der Regeln guter wissenschaftlicher Praxis selbstständig verfasst, keine anderen als die angegebenen Quellen und Hilfsmittel benutzt und die Zitate kenntlich gemacht habe.

Viernheim, den 04. September 2023

Danksagung

Zunächst möchte ich meine tiefe Dankkbarkeit gegenüber all denjenigen ausdrücken, die mich auf die eine oder andere Weise bei der Fertigstellung dieser Arbeit begleitet haben.

Zuerst möchte ich meinem wissenschaftlichen Mentor und Doktorvater, Herrn Prof. Dr. Peter Vöhringer, danken für die freundliche Aufnahme im Arbeitskreis, für die Betrauung mit diesem interessanten und überaus abwechslungsreichen Forschungsprojekt, für aufschlussreiche und angeregte Diskussionen sowie für den fachliche Rat. In diesem Zuge möchte ich mich gleichermaßen ebenfalls bei Dr. Jörg Lindner bedanken, der mir nicht weniger bei praktischen Fragen, bei der täglichen Laborarbeit und fachlichen Fragen und Problemen stets helfend zur Seite stand. Mit ihrer Gründlichkeit und der kritischen Auseinandersetzung mit wissenschaftlichen Fragestellungen haben sie beide mich sehr geprägt und zu einem verantwortungsbewusstem, kritisch denkendem Naturwissenschaftler erzogen und auch dafür gebührt ihnen mein herzlicher Dank. Meinem guten Kollegen Dr. Luis Ignacio Domenianni möchte ich außerdem danken für die großartige und umfangreiche Unterstützung, sei es bei praktischen Arbeiten im Labor, für angeregte Diskussionen, fachliche Inspiration und für wertvolle Kommentare und Verbesserungsvorschläge bei der Durchsicht der Arbeit. Muchas Gracias, Luis, außderdem für die zahlreichen Kniffe und Tricks bei der Justage der optischen Aufbauten, die du stets auf Lager hattest und bereitwillig geteilt hast. Ich konnte viel von dir lernen und habe es sehr genossen gemeinsam im Labor zu arbeiten. Nichtsdestotrotz war stets auch Zeit für zahlreiche entspannte Unterhaltungen und Späße und auch dafür möchte ich ausdrücklich Danke sagen. An einer entspannten Arbeitsatmosphäre und den notwendigen Spaß am Arbeitplatz hatten stets auch meine geschätzten Büro-Kollegen, Inga Majer, Paul Brünker und Dr. Steffen Straub einen großen Anteil. Auch wenn es manchmal anders erschien, wurde in unserem Büro allerdings nicht nur gescherzt und gelacht, sondern auch naturwissenschaftliche Diskussionen geführt und für das alles möchte ich auch euch allen danken. Besonders erwähnen möchte ich an dieser Stelle meinen Kollegen Dr. Steffen Straub, der mich bereits noch zu meiner Zeit als Masterand angelernt hat und von dem ich den entsprechenden experimentellen Aufbau und eine Menge fachliches Know-How übernehmen konnte. Hervorheben möchte ich zudem meine Kollegen Annette Schäfermeier und Reinhold Fligg für ihren hervorragende Einsatz zur Bereitstellung und Instandhaltung der Laborinfrastruktur. Sicherlich nicht zu kurz kommen dürfen in diesem Zusammenhang auch die Kollegen

aus den Werkstätten des Instituts, allen voran Herr Daniel Poetes, Herr Heinz-Peter Königshoven und Herr Rolf Paulig, die immer einen guten Vorschlag parat hatten, um selbst die verrücktesten Ideen zu realisieren und auf diese Weise das Leben im Labor vielfach vereinfacht und viele Projekte überhaupt erst ermöglicht haben. Ihnen allen gebührt dafür mein herzlicher Dank. Allen übrigen hier nicht namentlich erwähnten Mitgliedern der Arbeitsgruppe Vöhringer möchte ich für die angenehme Atmosphäre und für die herzliche Aufnahme danken. Ich habe mich sehr wohlgefühlt und die Zeit als Mitglied der Arbeitsgruppe sehr genossen und werde mich gerne an die gemeinsame Zeit zurückerinnern.

Über alle Maße möchte ich jedoch auch all den Menschen danken, die mich von Anfang an auf dieser langen Reise begleitet haben und ohne die ich dieses Ziel nicht alleine hätte erreichen können; meiner Familie und meinen Freunden. Danke Mama, danke Papa, dass ihr mich von Anfang an bei meinem Unterfangen unterstützt habt, mir das Chemiestudium ermöglicht habt, mich aufgebaut und ermutigt habt und mir vorgelebt habt mit Beharrlichkeit und Ehrgeiz meine Ziele zu verfolgen. Liebe Freunde, auch ihr habt einen großen Anteil an dieser Arbeit. Mit euch konnte ich stets abseits der Arbeit eine schöne Zeit verbringen und Energie tanken für die tägliche, manchmal etwas kräftezehrende Forschungsarbeit.

Euch allen noch einmal meinen herzlichen Dank!

Contents

1. Introduction **1**

2. Chemistry of Azide Compounds **5**
2.1. Structure and Bonding 5
2.2. Photochemistry of Azide Compounds 8
2.2.1. Redoxneutral Azide Ligand Dissociation 9
2.2.2. Photoreductive Azidyl Radical Formation 9
2.2.3. Nitrene Formation via Dinitrogen Extrusion 10
2.2.4. Photooxidative Azide Cleavage 13

3. Theoretical Background **17**
3.1. Stationary Infrared Spectroscopy 17
3.2. Ultrafast Time-Resolved Infrared Spectroscopy 18

4. Experimental Setup **23**
4.1. Stationary Spectroscopy 23
4.2. UV-Pump Mid-Infrared-Probe Spectroscopy 23

5. Photophysics and Photochemistry of trans-Bis(acetylacetonato)azido pyridine cobalt(III) **29**
5.1. Synthesis 29
5.2. Molecular and Spectroscopic Properties 31
5.2.1. Single Crystal X-Ray Diffraction Studies 31
5.2.2. NMR Spectroscopy 33
5.2.3. FTIR Spectroscopy 34
5.2.4. UV/Vis Spectroscopy 38
5.3. Investigations on Thermal Ground State Dynamics 42
5.3.1. Spectral Dynamics 42
5.3.2. Kinetic Analysis 46
5.3.3. Theoretical Investigation 50
5.4. Time-Resolved Spectroscopy 53
5.4.1. UV-Pump mIR-Probe Spectroscopy 53
5.4.2. UV-Pump nUV-to-Vis-Probe Spectroscopy 60
5.4.3. Discussion 64

6. Photophysics and Photochemistry of Diazido[1,2-bis(diphenylphosphino)-ethane]nickel(II) 69
6.1. Synthesis . . . 69
6.1.1. Dichlorido[1,2-bis(diphenylphosphino)ethane]nickel(II) . . . 70
6.1.2. Diazido[1,2-bis(diphenylphosphino)ethane]nickel(II) . . . 70
6.2. Molecular and Spectroscopic Properties . . . 72
6.2.1. Single Crystal X-Ray Diffraction Studies . . . 72
6.2.2. FTIR Spectroscopy . . . 74
6.2.3. UV/Vis Spectroscopy . . . 77
6.3. UV-Pump mIR-Probe Spectroscopy . . . 80
6.3.1. Experimental . . . 80
6.3.2. Discussion of Time-Resolved Spectra . . . 81
6.3.3. Kinetic Analysis . . . 86

7. Conclusion and Outlook 89

8. Bibliography 95

A. Glossary 103

B. List of Chemicals 105

C. Theoretical Calculations 106
C.1. $Co(acac)_2(N_3)(py)$ . . . 106
C.1.1. $trans-Co(acac)_2(N_3)(py)$ . . . 106
C.1.2. $cis-Co(acac)_2(N_3)(py)$ . . . 111
C.1.3. $trans-Co(acac)_2(N_3)$ . . . 114
C.1.4. $cis-Co(acac)_2(N_3)$ . . . 116
C.2. $Ni(dppe)_2(N_3)_2$ . . . 118
C.2.1. $Ni(dppe)_2(N_3)_2$ $(S = 0)$ . . . 118
C.2.2. $Ni(dppe)_2(N_3)_2$ $(S = 1)$ . . . 122
C.2.3. $Ni(dppe)_2(N_3)(N)$ $(S = 0)$ . . . 125
C.2.4. $Ni(dppe)_2(N_3)(N)$ $(S = 1)$ . . . 128

1. Introduction

Life on earth as we know it would not be possible without light. In its early stage, earth was a hostile place with a primordial atmosphere that did not support higher forms of life. It is only thanks to the advent of photosynthesis some 3.4 billion years ago, that enabled enrichment of oxygen in the atmosphere by prehistoric organisms over the course of millions of years. This process ultimately then paved the way to the development of complex, living creatures including mankind.[1] Naturally, scientists have been intrigued by the process of photosynthesis as the foundation of our very existence for several hundreds of years already, since it features the chemical activation of thermodynamically highly stable water (H_2O) and carbon dioxide (CO_2) molecules; a process sought-after for several decades already.[2–4] For example, as early as more than 100 years ago Ciamician already envisioned the utilization of sunlight for the activation of chemical compounds leading into a sustainable and ecofriendly future.[5]

Amid the dramatic effects of climate change and increasing fossil fuels prices as well as the devastating effect of exhaustive exploitation of natural resources and yet still further increasing carbon dioxide emissions worldwide,[6] a fundamental transformation of our way of life is of utter importance. Hence, approaches to mimic the natural process of photosynthesis have attracted particular attention. Therefore, research aiming at the development of artificial photosynthesis is of great interest both from a economical and ecological as well as from a social perspective since it bears the potential to change our lifestyle to become more sustainable. Thus, approaches to utilize solar energy for the chemical activation of the greenhouse gas carbon dioxide by means of suitably tailored systems are especially compelling and have been investigated in detail over the last few decades.[7]

Inspired by nature, which utilizes the earth-abundant metals manganese and calcium in the oxygen evolving complex (OEC) of photosystem II for this purpose,[8] many of these artificial systems developed and presented in the recent past are based on transition metals. This class of compounds, in general, exhibits a plethora of possible electronic and structural motives. Hence, carefully tuning the system to enable the desired reactivity is a frequently applied approach in this field and bears the potential to enable artificial photosynthesis.

One of the archetypes of these systems, that exhibits carbon dioxide reduction chemistry, is the highly credited ruthenium tris(bipyridine) cation ($[Ru(bipy)]^{2+}$) as reported by Lehn and coworkers[9] already in the early 80s. Following up on these find-

ings, until today researchers have developed systems that exhibit similar CO_2 reduction photochemistry based on earth abundant, hence comparably cheap, transition metals such as for instance iron, cobalt and nickel.[10–12]

Thus, in order to gain a deeper understanding, that may boost the development of improved, highly efficient systems, a profound knowledge about the primary processes occurring in transition metal complexes following electronic excitation is pivotal. In fact, owing to the large variety of possible photochemical and photophysical pathways, in addition with the potential to tune these properties – within a certain range – to one's requirements, the photochemistry of these systems has been of paramount interest in the last few decades.

Often the relevant sequence of photochemical and photophysical processes is rather complex and occurs on tremendously fast timescales of barely a few nanoseconds. Hence, in order to deepen the understanding of these systems, it is mandatory to apply techniques that are capable to track the fate of the system after excitation. In this context, time-resolved spectroscopy is the method of choice to elaborate the subtleties of the underlying mechanisms. Following the development of flash photolysis by Porter and coworkers,[13,14] thanks to the advent of lasers, the achievable temporal resolution of time-resolved spectroscopic experiments improved from the micro- to the femtosecond regime over the course of only a few decades. What is today known as pump-probe spectroscopy, has opened up a multitude of new opportunities. This spectroscopic technique enables experimentalists to prepare a system in a non-equilibrium configuration, often an excited state and monitor the fate of the system by investigating its spectroscopic characteristics. Thus, nowadays on the femtosecond timescale, even the very nature of the involved states and intermediates is in principle spectroscopically observable. A particularly powerful method in this regard entails probing the characteristics of the excited sample by infrared (IR) radiation owing to the structure sensitivity of IR spectroscopy, i.e., the time-resolved spectrum is governed by the distinct absorptions of selected functional groups and molecular entities and is therefore sensitive to the chemical nature of the excited state or potential new species formed under the impact of the excitation.

In this particular work, ultraviolet-pump mid-infrared-probe spectroscopy, throughout the following pages referred to as UV/mIR spectroscopy, was applied for the investigation of two transition metal azido complexes in particular. This is motivated by the fact, that the photolysis of azide compounds is known to be a viable route to nitrenes, systems with only six electrons in the valence shell of the nitrogen atom, or to the formation of high-valent transition metal nitrido complexes, respectively. Here, the prior is particularly interesting both from a conceptual perspective owing to the peculiar electron sextet that gives rise to different potential spin configurations that, in turn, has massive impact on the overall behavior of the system, as well as from a synthetic point of view. Thus, the electron deficiency on the nitrogen renders these systems po-

tent reagents for a series of useful reactions. Nitrido complexes, on the other hand, can be regarded as model systems to understand reactive intermediates in catalytic cycles. Thus, for instance, an iron nitrido intermediate is believed to play a crucial role in the commercially highly relevant Haber-Bosch ammonia synthesis in industry.[15,16] Moreover, as was shown in our work group, the photolysis of a suitable iron azido system, for example, entails the formation of a high-valent iron(V) nitrido species.[17–23] Owing to its isoelectronic structure to the invoked iron(IV) oxo species in the catalytic cycle of enzymes of the cytochrome P450 class,[24–26] that enables selective carbon-hydrogen bond activation in nature, this may lead to a better understanding of the factors that govern the reactivity of high-valent iron complexes in general. In fact, azido complexes constitute ideal candidates to be studied by this experimental technique as many of these systems are known to be photolabile, i.e., the azide ligand tends to decompose upon excitation. Therefore, their photochemical reactivity can be selectively triggered by a suitable pump pulse in the ultraviolet (UV) range of the electromagnetic spectrum. The consequent processes can then conveniently be tracked by monitoring the corresponding intense and highly characteristic vibrational absorption bands of the azide moiety in the mid-infrared (mIR).

In the present thesis, first, the electron-rich, d^6 low spin compound *trans*-bis(acetylacetonato)azidopyridinecobalt(III) (*trans*$-\mathrm{Co(acac)_2(N_3)(py)}$, *trans*-**[1]**) as a model for octahedral, azido complexes was investigated and its photophysical and photochemical behavior was scrutinized. Apart from the complex excited state dynamics, the system was shown to also be subject to thermal ground state dynamics in solution and investigations to explore these have been conducted likewise. Secondly, UV/mIR spectroscopy was applied to study the square planar d^8 nickel complex, diazido[1,2-bis(diphenylphosphino)ethane]nickel(II) ($\mathrm{Ni(dppe)(N_3)_2}$, **[2]**) and the insight derived from these investigations will be presented. This latter project especially, was inspired by the research of Hennig and coworkers[27–29] in the 90s who, by indirect means, namely trapping experiments, established that this compound is prone to collapse upon irradiation under formation of a highly reactive nitrene and release of dinitrogen ($\mathrm{N_2}$). The photophysical and photochemical pathway that gives rise to the observed behavior, however, has not been understood in detail so far, in part, owing to the ultrafast nature of the underlying processes and the fleeting nature of the states and reactive species in this sequence.

In summary, the following pages should be considered as a small contribution to gain an improved, general understanding of the factors that govern the photochemistry of transition metal complexes. Thus, the results presented herein may provide guidance and inspiration to experimentalists as how to design and tailor systems that ultimately may enable the ecologically highly desirable utilization of solar light in the context of chemical synthesis.

2. Chemistry of Azide Compounds

To set the ultrafast spectroscopic investigations on the photochemical and photophysical properties of *trans*-$Co(acac)_2(N_3)(py)$ and $Ni(dppe)(N_3)_2$ presented in this work into a larger context, in the following selected aspects of the chemistry of azide compounds will be discussed.

Transition metal ions tend to form a large variety of coordination complexes. The availability and the involvement of metal *d*-orbitals in chemical bonding opens up a multitude of different coordination schemes, coordination numbers and spatial arrangements of the atoms. Moreover, variations in the electronic structure that give rise to open-shell or closed-shell, i.e., paramagnetic or diamagnetic, complexes diversify the number of possible configurations even further and cases are known, in which slight alterations to the spin configuration have a tremendous effects on the observed molecular structure and, accordingly, the properties of a system.[30] Thus, a profound understanding of the underlying aspects that govern the bonding situation is pivotal in order to rationalize the chemical and physical behavior of these systems.

Among these systems, over the course of several decades the chemistry of transition metal azide complexes, systems that feature a N_3^- anion ligated to a metal center, has attracted wide-spread interest, due to the peculiar properties of the N_3 moiety which will be discussed in more detail throughout the following chapter.

2.1. Structure and Bonding

The chemistry of azide complexes is largely governed by the peculiarities related to the chemical bonding of the N_3 group. Its electronic and structural properties should therefore be treated in some detail to rationalize the observed chemical behavior.

In accordance with fundamental chemical concepts such as valence bond theory[31–33] and the valence shell electron pair repulsion model (VSEPR),[34,35] the isolated azide anion by itself adopts $D_{\infty h}$ symmetry,[36] i.e., a linear geometry ($\angle(N-N-N) = 180°$) with two N–N bonds which are equal in length. Usually bond distances of roughly 1.154 Å are observed with minor variations depending on the exact nature of the counter ion.[37]

In spite of the fact, that the azide ion is a thermodynamically unfavored species,[38] the respective alkaline, earth alkaline and ammonium salts are usually considered relatively stable. Contrary to this comparably high inertness of these ionic azides, compounds that contain essentially covalently bound N_3 groups exhibit vastly different

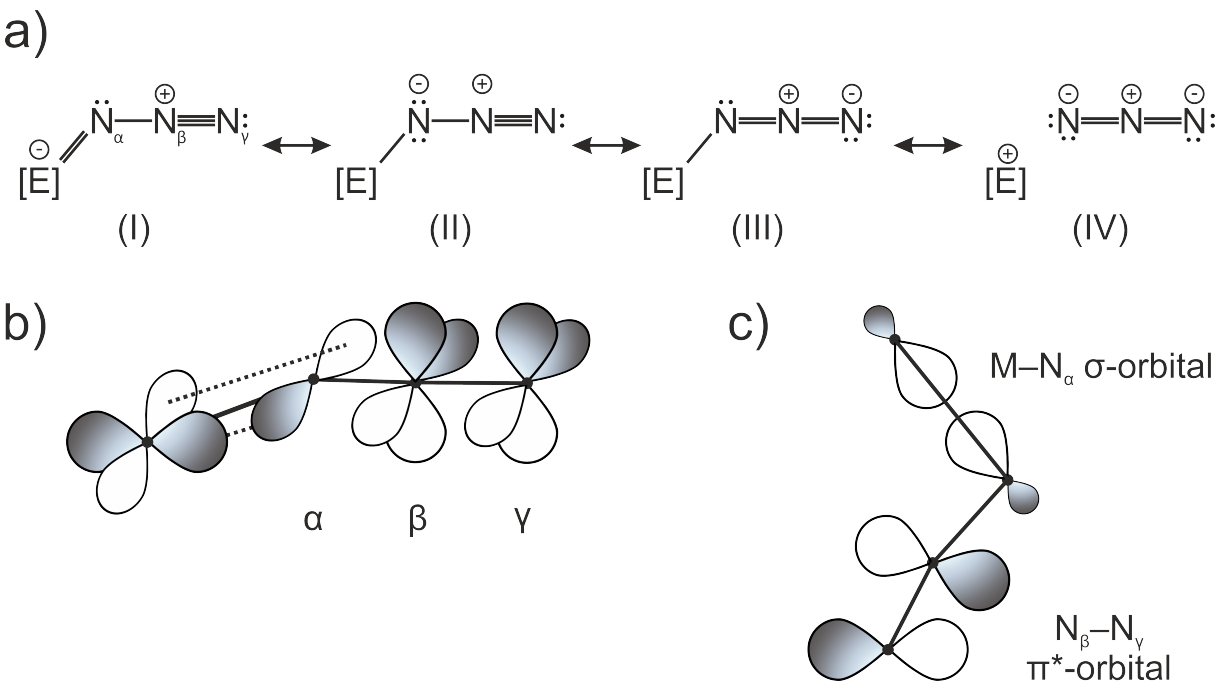

Figure 2.1.: *Structure and bonding in azido complexes. The electronic structure can be described by several mesomeric resonance structures a). Realization of metal azide π-bonding occurs by interaction of metal d-orbitals and p-orbitals on the nitrogen b). Depending on the strength of the negative hyperconjugation effect between the metal nitrogen σ-bond and the antibonding π-orbital as sketched in c), the N_β-N_γ bond is elongated in comparison with a common nitrogen-nitrogen triple bond as resonance structures (I) and (II) might suggest.*

chemical behavior. Many characteristics and the factors that govern their reactivity, can be understood based on the knowledge about the simplest representative of this class of compounds, hydrazoic acid (HN_3), the conjugate acid of the azide anion.[39] Here, the spectacular determination of its X-ray structure[40] should be highlighted in particular, since it demonstrated all to clear many of the structural peculiarities discussed in the following. The significance of this work becomes apparent amid the fact that HN_3 is a highly endothermic molecule manifesting itself by its explosive nature and high reactivity[39] which, in fact, is a common feature shared among most covalent azides.[41]

The tendency towards spontaneous detonation of many azide compounds is nowadays well-understood on the basis of thermodynamics and chemical bonding. The electronic structure of the N_3 moiety attached to a transition metal or a main group element E can be described by several resonance structures as depicted in Fig. 2.1a).[37,39,41] Following usual conventions the nitrogen atoms of the azido fragment throughout the following are denoted by Greek letters (c.f. structure (I) in Fig. 2.1a)). In fact, the actual electronic configuration should be considered as a superposition of either of the depicted structures. Albeit, structures (II) and (III) are thought to give the dominant contributions,[33,37] the exact weights of either of the structures to the actual electronic configuration is determined by the nature of the fragment E the azido group is attached to.

Nonetheless, the mesomeric structures illustrate the dipolar character of the N_3 moiety which, in fact, renders it a potent reactant in 1,3-dipolar additions to suitable dipo-

larophiles such as olefins, alkynes or carbon disulfide[37,42] enabling a synthetic approach to a variety of five-membered heterocycles. Especially the reaction with alkyne substrates is well-known in the literature as Huisgen cycloaddition[43] which ultimately paved the way to modern copper catalyzed 'click' chemistry as popularized by Sharpless.[44–46] Due to its versatility and simplicity, up to today it has been widely and successfully applied for instance in the field of drug discovery and development[47,48] and was therefore acknowledged by the Nobel prize in chemistry in 2022.

Apart from the observed reactivity, the asymmetry of the charge distribution across the N3 fragment also manifests itself in its structure. As was shown by Evans and coworkers,[49–51] with increasing difference between the ionization potential of the metal and the electron affinity of the azidyl ion (3.05 eV), the $M-N_\alpha$ bond becomes more and more covalent in nature.[52] Consequently, the orbital interaction between the metal *d*-orbital and the π-orbital on the N_α atom, which is schematically depicted in Fig. 2.1b), is increased[37] which in turn weakens the $N_\alpha-N_\beta$ π- bond. Thus, in case of covalent azido compounds of the main group elements and transition metals, usually an elongation of the $N_\alpha-N_\beta$ in comparison with the $N_\beta-N_\gamma$ bond is observed, i.e., the overall contribution of resonance structure (I) (c.f. Fig. 2.1) is higher.[39] In fact, this asymmetry is a very characteristic feature and is therefore often discussed as a marker to deduce the degree of covalency of the metal-azido bond. However, other than suggested by mesomeric formula (I), the bond lengths of either of the two bonds, are significantly shorter ($N_\alpha-N_\beta$, 1.440 Å) or significantly longer ($N_\beta-N_\gamma$, 1.098 Å) than typical nitrogen-nitrogen single or triple bonds, respectively.[53–55] Klapötke and coworkers rationalized this observation by a negative hyperconjugation effect[53,56] which is schematically depicted in Fig. 2.1c). Donation of electron density from the $M-N_\alpha$ σ-bond into the antibonding $N_\beta-N_\gamma$ π^*-orbital of appropriate symmetry, reduces the respective bond order from the extreme case of 3 to a somewhat lower value.

Moreover, also the $E-N_\alpha-N_\beta$ bonding angle has been the subject of fundamental discussions. In fact, it is observed, that the bonding angle usually amounts to a value of slightly below 120°[36] indicating that upon ligation the N_α atom adopts sp^2-hybridization. In this configuration, the first sp^2-hybrid orbital emerges in σ-bonding to the metal, a second one into σ-bonding to N_β, whereas a free electron pair resides in the third sp^2-hybrid orbital. Here, the increased spatial demand of the lone pair according to the VSEPR can be invoked to rationalize the slight compression of the $E-N_\alpha-N_\beta$ angle. The *p*-orbital, however, that is perpendicular to the $E-N_\alpha-N_\beta$ plane is available for π-bonding with the remaining two nitrogen atoms. Interestingly, a linear coordination mode, i.e., a configuration where $\angle(E-N_\alpha-N_\beta) = 180°$ is usually not observed. Müller argued that this observation is a clear indication that in case of the isolated azide, the free electron pair resides in the *s*-orbital. If the atomic orbitals hybridized to a appreciable amount, on the terminal atoms doubly occupied *sp*-orbitals should be available that would cause the azide ion to preferably coordinate in a linear fash-

ion. Consequently, upon ligation the degree of π-delocalization is decreased and the π-electrons tend to be more localized on the N_β and the N_γ atoms.[36]

Additionally, upon bonding to a metal center, also the linear geometry of the azido moiety is disturbed. Often a slight but significant bending with N−N−N angles of $(172 \pm 3)^\circ$ is observed as schematically shown in Fig. 2.1c). Because of that, in the literature the structure is frequently described as adopting a *trans*-bent configuration since the terminal nitrogen atom and the metal center bent away from the $N_\alpha - N_\beta$ bond in a *trans* fashion[53,57] in part due to the partial loss of π-delocalization upon coordination.

2.2. Photochemistry of Azide Compounds

Besides its reactivity, the peculiar thermodynamic, structural and electronic properties have direct implications also on the photophysical and photochemical behavior of the azido unit. In fact, many of the reactivity patterns connected to the thermodynamically highly favored decomposition of the azide moiety, can also selectively be triggered by light and in some cases even be directed towards a specific reaction outcome by the exact illumination conditions such as for instance the wavelength of light. Therefore, for several decades already the photochemistry of azido systems has been the subject of detailed studies and has been reviewed in great detail in the literature.[58]

Over the course of the years several common patterns connected to the photochemical reaction pathways have been identified which are summarized in Fig. 2.2 and will be discussed in the following.

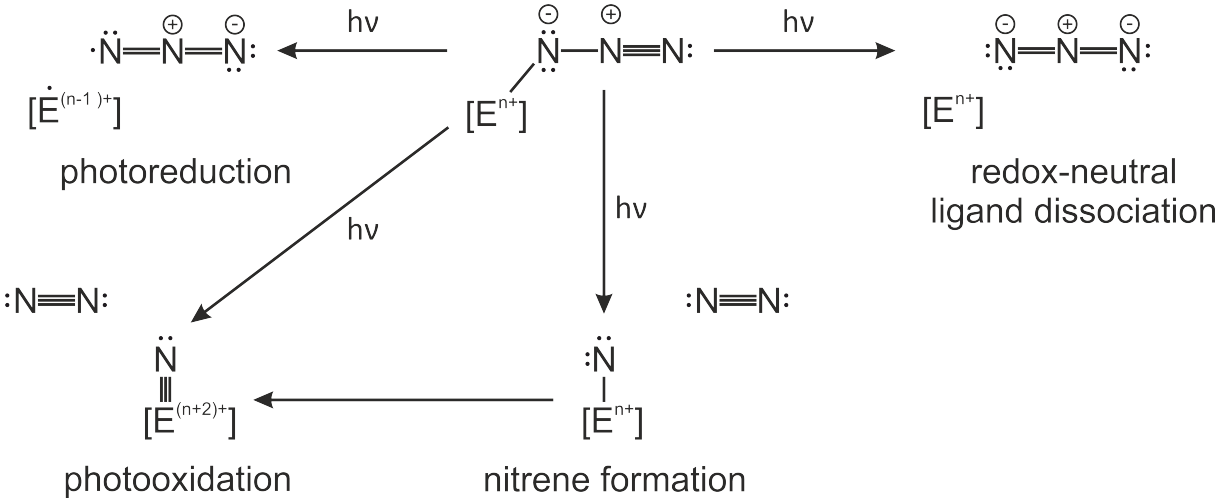

Figure 2.2.: *Overview of frequently observed photochemical reaction pathways observed in azido complexes. Under the impact of a photon of suitable energy, the azide group may be cleaved off in a redox-neutral fashion (upper right) or, alternatively, involving homolytic $M-N_\alpha$ bond cleavage leading to a formal reduction of the metal fragment (upper left). Photochemically induced $N_\alpha - N_\beta$ bond fission, in turn, enables the formation of metal nitrenes or metal nitrides, which entail formal oxidation of the metal center (lower part). The latter can be formed either directly or via a nitrene as an fleeting intermediate during the reaction sequence.*

2.2.1. Redoxneutral Azide Ligand Dissociation

The simplest of the possible photochemical reactions is realized by redoxneutral heterolytic cleavage of the $M-N_\alpha$ bond. Hence, this pathway essentially entails the extrusion of an intact azide anion from the complex thereby furnishing an undercoordinated transition metal complex fragment. Owing to the vacancy in the coordination shell, the thus obtained fragment often exhibits Lewis acidic properties and therefore tends to ligate suitable molecules from its surrounding. It is therefore not surprising, that this reaction pathway is frequently observed in solvents that both exhibit sufficient donor abilities themselves and moreover are sufficiently polar to stabilize the negative charge of the released azide anion such as for instance acetonitrile (CH_3CN) or dimethyl sulfoxide ($(CH_3)_2SO$).

In fact, this pattern was frequently observed in our workgroup, for instance by Flesch *et al.*[59] in case of the cobalt triazido complex *mer*$-[Co(dien)(N_3)_3]$ or by Torres-Alacan *et al.*[18] when exciting the complex cation $[Fe(cyclam)(N_3)_2^+]$ at lower photon energies, respectively. Either way, the photolysis led to release of azide anions and formation of the respective dimethyl sulfoxide and acetonitrile complexes, which were identified by their transient infrared absorption spectra. Another, unexpected example of this reaction channel was reported by Becalska and coworkers[60] for optical excitations into the *d-d* transition bands of the square-planar d^8-complex *trans*$-(Et_3P)_2Pt(N_3)_2$.

2.2.2. Photoreductive Azidyl Radical Formation

Moreover, also the release of azidyl radicals ($N_3\bullet$) from suitable azido complexes is commonly observed upon excitation. In contrast to the previously discussed pathway, this reactivity is brought about by homolytic $M-N_\alpha$ bond cleavage. Summarizing several known examples, it was pointed out that in most cases, this pathway is channeled through the initial population of a ligand-to-metal charge transfer (LMCT) state that relocates electron density from the azide ligand onto the metal center[58,61] and therefore formally entails photoreduction of the metal. Accordingly, the LMCT state of the respective systems can be considered as a complex bearing an azidyl radical ligand. If the stability of the system in the excited state however, is not high enough and the state is sufficiently long-lived, it can collapse by dissociating an azidyl radical. However, the ultimate fate of the azidyl radicals is often only vaguely known since due to its radical character it tends to undergo a variety of abstraction reactions giving rise to multiple potential reaction products. Likewise, it is well-established that azidyl radicals may alternatively also recombine in a secondary step that ultimately leads to formation of dinitrogen.

The exact mechanism that ultimately leads to the formation of dinitrogen, however, has been the subject of controversial discussions. For instance, based on spectroscopic findings, Vogler *et al.* interpreted the results of the photolysis of $Pt(N_3)_2(PPh_3)_2$ in

terms of the intermediate formation of the pseudohalogen N_6 species formed from radical combination of two fleeting azidyl radicals.[62] The nature of the putative intermediate has been the subject of extended fundamental discussions and theoretical studies with, in part, contradictory results concerning its structure and thermodynamic stability.[54,63] In addition to the radical combination pathway, it was also suggested that the azidyl radical itself may collapse to form dinitrogen and an isolated nitrogen atom. This unusual reactivity was shown in low temperature matrices on photolyzed samples of $[Pt(CN)_4(N_3)_2]^{2-}$ by the characteristics of the free nitrogen atom in the electron paramagnetic resonance (EPR) spectrum.[64] Regardless of the exact mechanism, it can be summarized, that if not trapped by any kind of abstraction reaction, ultimately the azidyl radical decays via suitable reaction channels which finally yield dinitrogen.

One of the ground breaking reports that unequivocally established the feasibility of this overall photochemical reaction sequence was provided by Rehorek and coworkers[65] proving previous claims by Endicott and Ferraudi[66–68] on the involvement of azidyl radicals in the photolysis of $[Co(CN)_5(N_3)]^{3-}$. Employing EPR spin trapping studies, it was established by direct means that this system degrades upon UV photoexcitation under release of $N_3\bullet$ and reduction of the central Co^{3+} ion to Co^{2+}. As Endicott and coworkers had already shown before, the reaction ultimately leads to the formation of dinitrogen that results from a subsequent thermal follow up reaction of the azidyl radicals and is released from the system, albeit with a minute quantum yield in the sub-percent range. Detailed studies on further Co(III) system, such as $Co(acac)_2(N_3)(NH_3)$ carried out by Reed and coworkers,[69,70] likewise demonstrated a similar photoreductive behavior and established that this pathway is frequently observed for low-spin trivalent cobalt. Similarly, studies conducted in our workgroup on the high-spin complex $[Fe(cyclam-ac)(N_3)]^{+}$ demonstrated this pathway to be also feasible for Fe(III) systems, although in this particular case a certain wavelength dependency on the followed reaction pathway was observed.[17]

In fact, these findings are in line with a general trend observed over several prominent examples in the literature. Thus, as a rule of thumb it can be stated that the photoreductive pathway is a favorable process in cases where the central transition metal features two comparably stable oxidation states that are interconvertible via one-electron reduction or oxidation, respectively. Thus, unsurprisingly, this reaction channel is frequently observed for Mn(III), Fe(III), and Co(III) systems which following this pathway, are reduced to Mn(II), Fe(II) or Co(II), accordingly.

2.2.3. Nitrene Formation via Dinitrogen Extrusion

As discussed in section 2.1, owing to the increased degree of localization of the π-electrons upon bonding to a transition metal or a main group element, the relative weight of resonance structure (I) that features a triple bond, is increased. Consequently, the structural rearrangements that would be required to cleave the $N_\alpha - N_\beta$ bond and

to release the $N_\beta - N_\gamma$ fragment as a dinitrogen molecule (N_2), are comparably small. Therefore, the azide group is often described as being preconfigured for decomposition under release of dinitrogen.[39] From a thermodynamic perspective, this is actually a highly favorable process, especially in light of the fact, that the extreme stability of N_2 itself, renders this reaction some additional driving force. Therefore, heterolytic cleavage of the $N_\alpha - N_\beta$ bond, is a frequently observed fragmentation pathway for these kinds of compounds which can be triggered either thermally or photochemically. Indeed, this has rendered azide compounds useful reagents in synthetic chemistry. For instance, this reactivity is exploited in the Staudinger reaction or the Curtius rearrangement for the synthesis of organic amines or isocyanates, respectively.[71]

This reaction is particularly interesting also from a conceptional perspective owing to the peculiar nature of the remaining metal-nitrogen moiety, $[M]-N_\alpha$. Since the valence shell of the nitrogen atom is occupied by six electrons only, i.e., the octet rules is not full-filled, the nitrogen is highly electron deficient rendering it a potent reactant. Consequently, there has also been a pronounced theoretical interest in the exceptional electronic structure of nitrenes, which, in fact, requires some additional discussion and will be reviewed in the following.

Electronic Structure of Nitrenes

In general, the overall spin quantum number $S = \sum s_i$ of nitrenes can adopt two possible values; S = 0 or S = 1. Accordingly, this class of compounds is usually grouped into singlet or triplet nitrenes, respectively. However, the corresponding electron sextet on the nitrogen can be realized in several ways which are sketched in Fig. 2.3. In the most straightforward way, the triplet state, the electronic structure is characterized by two singly occupied *p*-orbitals with the spin vectors of the electrons being aligned parallel, thereby maximizing the overall spin moment (I).

Inverting the spin of one of the unpaired electrons, however, yields a singlet configuration, that owing to the diradical character is denoted as open-shell singlet (II). The simplest singlet configuration, however, can be realized by electron pairing thereby leaving one *p*-orbital vacant (III, closed-shell singlet). Moreover, and less intuitively, another open-shell singlet configuration can also be realized as the superposition of two apparently closed-shell determinants which gives rise to Open-shell singlet B (IV).[72]

The particular electronic configuration also manifests itself in the reactivity of nitrenes. Thus, for instance in case of triplet nitrenes, the chemical behavior is essentially governed by the two unpaired electrons in the valence shell, i.e., these systems can be regarded as diradicals and react accordingly. As is typical for radicals, triplet nitrenes are prone to undergo abstraction and insertion reactions but on the other hand are relatively unreactive towards Lewis bases,[58] owing to the spin forbidden nature of an electrophilic addition to a potential substrate.

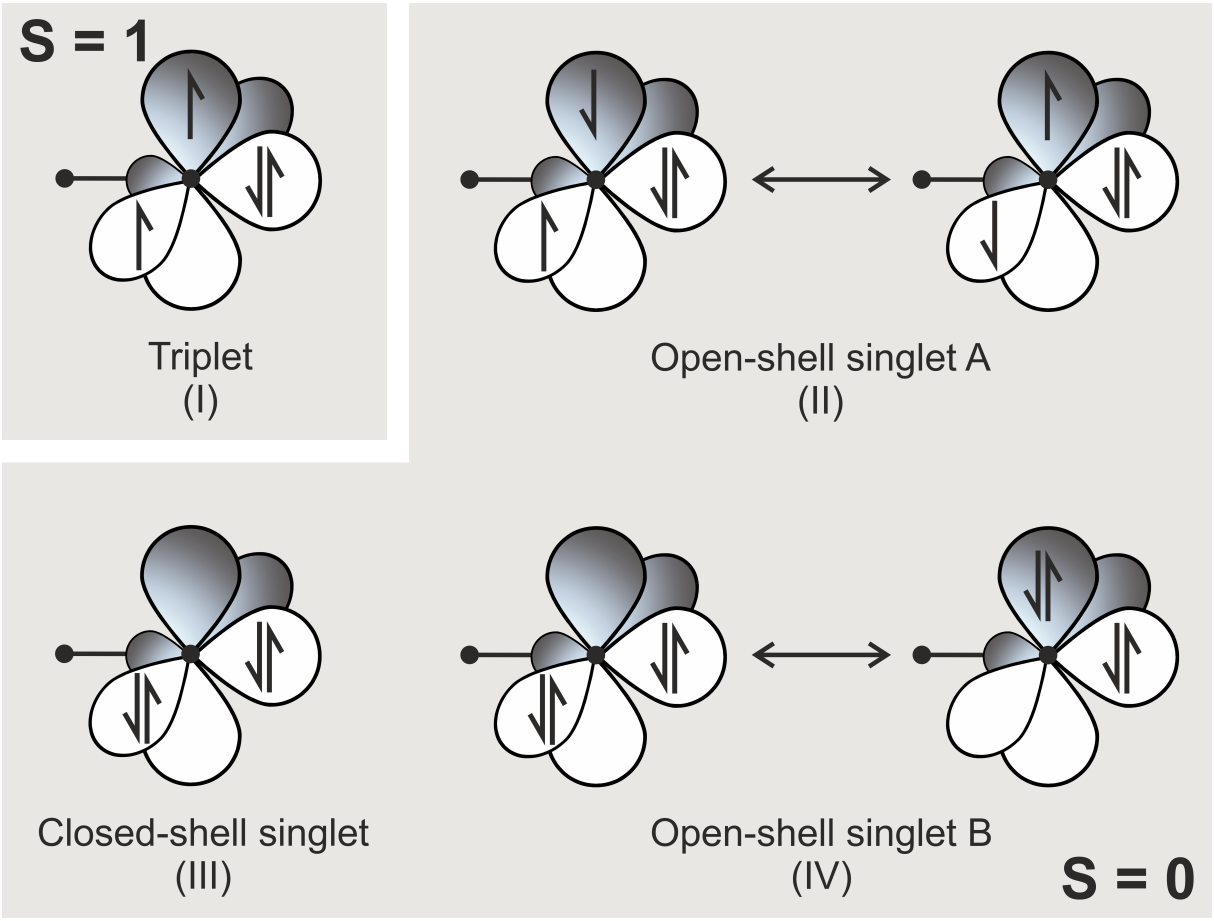

Figure 2.3.: *Representation of possible electronic configurations of nitrene systems. The electron sextet configuration can be realized either in a singlet or triplet state, which essentially differ by the overall total spin of $S = 0$ or $S = 1$, respectively. A parallel alignment of the spins of two unpaired electrons gives rise to the triplet state $(S = 1)$ (I). Distribution of two electrons with opposing spin across two p-orbitals in turn results in an open-shell singlet(II); the overall spin moment is $S = 0$, but the electrons are unpaired which has direct implications on the reactivity. Electron pairing of all the electrons, however, gives rise to a closed-shell singlet configuration leaving one nitrogen p-orbital vacated (III).*

Concerning the energetic ordering of the possible spin configurations, in most cases, it is observed that the electronic ground state of the respective nitrene species is a triplet.[58,72] This is well in line with Hund's rule, that states that the electronic ground state of a given system usually is composed such as to maximize the total spin moment.

Frequently, however, nitrene formation is initiated from a substrate featuring a different spin configuration as is often the case for organic compounds or square planar d^8 complexes, for instance, that exhibit a singlet ground state. Thus, prior to the formation of a triplet nitrene, an intersystem crossing (ISC) event is required, i.e., an overall change of the spin multiplicity is necessary. Usually this process is spin forbidden[53,73] and exceptions to this rule are only brought about by spin-orbit coupling effects rendering this process usually comparably slow. Still, in case of hydrazoic acid, for instance, it was shown by sophisticated multireference complete active space self-consistent field (CASSCF) calculations, that the transition state towards the formation of the simplest of the nitrenes, imidogene (NH), should be considered as a superposition of a singlet and a triplet state[72,74] that might facilitate this process.

Transition Metal Nitrenes

The photolysis of azido precursor compounds was identified very soon already as a viable route to interesting transition metal nitrene species. Pioneering work on the application of this reactivity in this field, was conducted already half a century ago when this pathway was identified to grant access to these systems. One of the very first examples was provided by Reed and Ferraudi in the early 70s who reported on the photochemical generation of a rhodium nitrene,[66,75] and Kane-Maguire invoked the intermediate formation of a ruthenium nitrene compound following an analogous approach.[76] Another instructive example of this reaction pathway was reported by Lane and Basolo on the formation of an iridium nitrene species upon photolysis of a suitable iridium(iii) precursor azido complex.[77] Detailed studies on nickel azido systems were likewise conducted by Hennig and coworkers in the 90s. Based on results obtained from trapping reaction studies, they indirectly established the intermediate formation of a nickel nitrene in the course of the photolytic decomposition of closed-shell, square planar nickel(II) diazido phosphine systems. For example, when conducting the photolysis under carbon monoxide (CO) pressure, the formation of the respective isocyanate complexes was observed as detected from the characteristic IR vibration band of the isocyanato ligand. Similarly, also by indirect means, i.e., by detection of an iminophosphorane photoproduct, obviously resulting from insertion chemistry of the electron deficient nitrogen species into the nickel phosphorus bond, Vreeken and coworkers demonstrated the formation of a related intermediate upon photolysis of a mononickel azide complex containing a phosphorus-nitrogen-phosphorus (PNP) pincer ligand backbone.[78] Interestingly however, Klein and Haller reported on the formation of imido and iminophosphorane bridging systems upon photolysis of Ni(Cl)(PMe3)2(N3) which still, undoubtedly must result from an intermediate nickel nitrene species.[79] Ngai and coworkers, moreover, presented some indications of the intermediate formation of a singlet nitrene during the course of the photolysis of Ni(tet)(N3) that was derived from the ultimate formation of the respective photoproducts.[80] Summing up these studies, it is evident that up to now, the intermediacy of nickel nitrene species has been proven mostly by indirect means due to the extreme reactivity of the respective species. Hence, to provide direct proof of these species and to deduce the photochemical mechanism leading to their formation, spectroscopic techniques that are fast enough to probe the properties of these fleeting intermediates are required and the necessity of femtosecond spectroscopic investigation has been invoked.[58]

2.2.4. Photooxidative Azide Cleavage

Apart from the nitrene formation pathway, in selected cases the extrusion of dinitrogen instead furnishes a nitrido species, i.e. the system can formally be regarded as a transition metal fragment to which a triply negatively charged N^{3-} ligand is coordinated.

This process entails a formal increase in the oxidation state of the metal by two units. Accordingly, this reaction is often referred to as photooxidative azide cleavage.[19,22] As a general trend, Chatt pointed out, that this pathway is in principle only feasible if +n and +(n+2) are reasonably stable oxidation states of the central transition metal and the overall electron count of the metal is sufficiently high.[81]

In fact, it is the high oxidation state of the metal that often renders transition metal nitrido complexes potent reagents, for instance in oxidations and nucleophilic additions. Therefore, they are frequently encountered as key intermediates in several catalytic transformations.[16] Moreover, these systems are also particularly interesting because of the electronic structure of these systems. In fact, the nitrido ligand is among the strongest π-donor ligands, hence in order to stabilize the nitrido ligand, vacant *d*-orbitals of suitable geometry are required that can accept electron density. Owing to this effect, it has been rationalized by Berry[82] that nitrido complexes of transition metals that adopt tetragonal geometry can only be realized up to group 8. Due to the isoelectronic structure of the oxo (O^{2-}) a similar rationale holds for oxo complexes. Since in tetragonal geometry neither nitrido nor oxo systems of later transition metal complexes were observed up to now, the term 'oxo wall' has been coined.

Besides its π-donor capacities, the nitrido ligand also exerts a pronounced *trans* effect which is often even that strong that no effective bonding of a ligand *trans* to the N^{3-} ligand can be realized. This effect is evident from the fact, that many nitrido complexes feature a vacant coordination site trans to the nitrido ligand giving rise to pentacoordinated, and hence formally undercoordinated, systems that do not conform to the 18 valence electron rule.[58]

The photooxidative formation of nitrido complexes was identified already quite early. Thus, for instance, already in the late 80s Arshankow and Poznyak demonstrated the formation of a chromium (V) nitride system from a suitable chromium(III) azido salene complex by direct isolation and characterization of the product of the photolysis by electron paramagnetic resonance and infrared spectroscopy.[83,84] In this case, the authors could established that preceding the ultimate formation of the nitrido system, a nitrene is formed in the first place. Owing to the high electron deficiency of the nitrene and a sufficiently high electron count on the Cr(III) center, the metal can be oxidized, thereby alleviating the electron deficiency on the nitrogen. Likewise, this reaction pathway was proven to be followed in case of the $[Fe(cyclam)(N3)2]^{+}$ complex by Torres-Alacan by means of time-resolved step-scan mid-infrared spectroscopy in our work group. Moreover, this finding was further corroborated by trapping reactions. Thus, in presence of suitable reactants such as carbon monoxide or tributylphosphine the formation of isocyanate and iminophosphorane gave undoubted evidence of the intermediacy of such a species.

Following the previously stated rule, in general, it is not surprising that this process is frequently observed for transition metals of groups 6 to 8 and several further examples

have been reported for the generation of high-valent complexes of transition metals such as iron,[18] ruthenium[85] and manganese.[86]

Nonetheless, it should be noted, that in some cases the electronic situation is in fact not as clear as it might seem at first glance. Since the nitrido ligand belongs to the class of redox-noninnocent ligands, it can be subject to inner-complex redox reactivity. Hence, in some cases the description as a nitridyl radical is more appropriate as spectacularly demonstrated by Scheibel and coworkers in case of an iridium complex. Albeit the system can formally be described as a Ir (V) system, electronic structure calculations and EPR spectroscopy reveal that the oxidation state of the metal is closer to +IV in reality due to one electron oxidation and formation of a nitridyl ligand. Another example was provided by Tran who based on reactivity studies could demonstrate the intermediacy of a titanium nitridyl species in their reaction sequence.[87]

3. Theoretical Background

Absorption of light by matter plays a vital role for many processes in nature. This phenomenon is observed basically for a wide range of the electromagnetic spectrum and entails the population of excited states. Following the rules of quantum mechanics, these energy levels are discrete, i.e., only photons of appropriate energies can induce transitions between states. Since the physical and chemical characteristics, such as for instance its color, are ultimately define by the energy levels of a system, spectroscopic investigations measuring the attenuation of light as a function of the photon frequency are of fundamental importance in developing a profound understanding for the properties of a sample. Therefore, nowadays, spectroscopy has developed to become a versatile tool and is routinely applied in analytical laboratories.

3.1. Stationary Infrared Spectroscopy

Among the many different techniques available, especially infrared (IR) spectroscopy, that relies on the observation of vibrational excitations of the system of interest, has evolved to be a very useful tool in the characterization of chemical compounds. Owing to the fact, that the absorptions in an IR spectrum often can be assigned to the vibrations of certain moieties of the molecular system, referred to as a local modes, vibrational spectroscopy has the advantage over other techniques of being structure sensitive[88] and therefore allows for derivation of information about the molecular connectivity.

As with many other techniques, the spectroscopic information is derived from the attenuation of light by a sample which can be quantified by the optical density $OD(\tilde{\nu})$ related to Beer's law according to

$$OD(\tilde{\nu}) = \log\left(\frac{I_0(\tilde{\nu})}{I(\tilde{\nu})}\right) = \epsilon(\tilde{\nu}) \cdot c \cdot d. \tag{3.1}$$

Here, $I_0(\tilde{\nu})$ and $I(\tilde{\nu})$ refer to the intensities of the incident and the transmitted light, respectively. The optical density at a given wavenumber $\tilde{\nu}$, in turn, is proportional to the optical path length d, the concentration of the analyte c and the frequency dependent molar decadic extinction coefficient $\epsilon(\tilde{\nu})$.

In the framework of IR spectroscopy, molecular vibrations are usually treated by the anharmonic oscillator model whose solution to the respective Schrödinger equation yields energy levels $E(\nu)$ given by

$$E(\nu) = \left(\nu + \frac{1}{2}\right)\omega_e - \left(\nu + \frac{1}{2}\right)^2 \omega_e \cdot x_e, \tag{3.2}$$

where the vibrational quantum number of the respective state is termed ν and the normal frequency and the anharmonicity constant of the vibration are denoted by ω_e and x_e, respectively. Hence, with increasing ν the energy levels shift closer together. Apart from the general selection rule, requiring a change in dipole moment due to the vibration, no particular selection rules apply within this model, i.e., transitions between arbitrarily spaced energy levels are in principle possible. However, the more intense excitations still entail transitions with $\Delta\nu = \pm 1$.[89–91] Thus, the required energy for a $\nu \rightarrow \nu + 1$ transition can be derived from Eq. 3.2 to be

$$\Delta E(\nu) = \omega_e \left[1 - 2x_e(1 + \nu)\right]. \tag{3.3}$$

As is evident, with increasing vibrational quantum number of the lower lying state involved in such a $\Delta\nu = \pm 1$ transition, for $\nu \geq 1$ the required energy of these so-called 'hot transitions' gradually decreases.

3.2. Ultrafast Time-Resolved Infrared Spectroscopy

As elaborated on in the previous chapter, frequently highly reactive intermediates are encountered in photochemical reactions. Often, their detection imposes a special challenge, especially if their lifetimes are short. For decades, the investigation of the underlying reaction mechanisms was limited to the detection of the resultant reaction products or matrix isolation studies at ultralow temperatures to suppress the thermal reactivity of the intermediates.

Nowadays, however, time-resolved spectroscopy has developed to become the method of choice for their unequivocal identification under ambient conditions which in addition to the frequency takes time as a second independent variable into account. In early times, such investigations were restricted to the milli- to microsecond scale[92,93] due to technical limitations such as for instance the relatively slow electronics utilized in such an experiment. The advent of lasers and the application of nonlinear optics, however, has enabled experimentalists to investigate physical and chemical processes on previously unprecedented timescales, nowadays ranging down even to the attosecond range.[94–96]

Since atomic motions usually occur on this ultrashort timescale, this technique bears the potential of direct observation of the primary events involved in chemical reactions such as bond breaking or bond formation. Pioneering work on this technique, nowadays referred to as femtosecond spectroscopy, in the context of chemistry, was conducted by A. Zewail[97] and the corresponding theoretical body in great was developed by Mukamel.[98] Beyond the sole detection of key reaction intermediates, provided suffi-

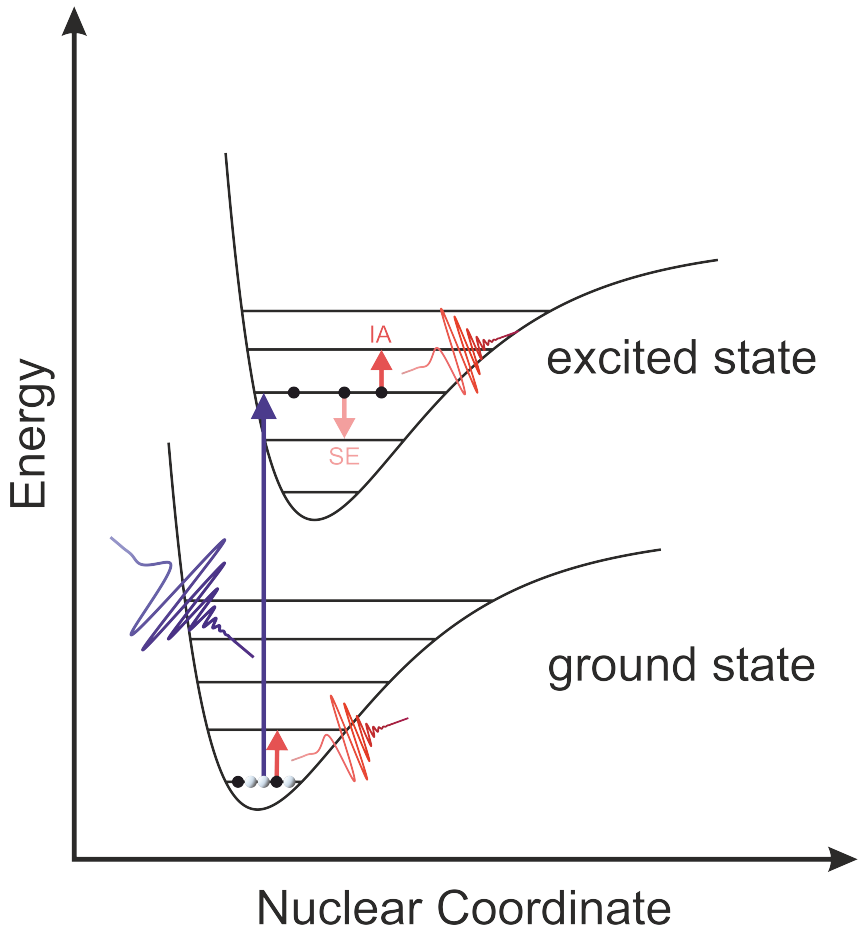

Figure 3.1.: *Schematic representation of the underlying principle of ultrafast UV-pump mid-infrared-probe spectroscopy. Under the impact of a UV pump photon (blue arrow), a certain number of molecules is promoted to the excited state surface. A delayed mid-infrared pulse sent into the sample shortly thereafter (in red), can then induce vibrational excitations on the excited state potential energy surface, which require a different energy in comparison with the ground state and give rise to induced absorption (IA) bands in a time-resolved spectrum. Likewise, the impact of a photon can induce vibrational deexcitation by stimulated emission (SE).*

ciently high time resolution, in cases that feature the involvement of excited states such as for instance photochemical reactions, also the detection of these 'doorway' states is in principle possible and enables scientist to develop a profound understanding about the factors that govern the reactivity of a system. The general principle relies on applying a perturbation to the sample by an ultrashort pump pulse. This transfers the system to an excited state whose spectral properties can then be monitored by a probe pulse sent into the sample after an appropriate time delay which, in femtosecond spectroscopy, is optically delayed relative to the excitation pulse.

Especially in the field of photochemistry, UV-pump mid-infrared-probe spectroscopy has proven particularly useful and is frequently applied since it enables derivation of structure related information of the excited state that ultimately paves the way to the resulting reaction products and the chemical nature of the latter. The basic underlying principle of UV/mIR spectroscopy is illustrated in Fig. 3.1. A pump pulse in the UV range, schematically depicted in blue, transfers a portion of the molecules (black dots) to the excited state potential energy surface (PES) thereby depleting the ground state

(indicated as grayish dots). Within the framework of the Born-Oppenheimer approximation, the motion of the electrons occurs on a timescale several orders of magnitude faster than the nuclear motion.[99] Hence, upon excitation the molecular geometry remains essentially unchanged.

Usually, the molecular geometries on the ground and the excited state PES surface are different due to population of higher lying non-bonding or even anti-bonding molecular orbitals that overall weaken the chemical bonds of the system. Moreover, the alterations to the spatial charge distribution directly effect the dipole moment of the system and hence its vibrational spectrum.[100] Therefore, the electronically excited state is usually prepared in a vibrationally highly excited fashion. However, since the nuclear coordinates are not altered by the electronic excitation, the excitation is described to undergo a vertical Franck-Condon transition. Here, the probabilities for the transitions to the respective vibrational levels on the excited state PES are governed by the Franck-Condon factors that are proportional to the squared overlap integrals of the vibrational wavefunctions of the ground and the excited state.[101–103]

Thus, an IR probe pulse (in red) sent into the sample after a given delay t can interact with the previously prepared excited state. This interaction with the probe pulse can occur via two kinds of mechanisms. Firstly, the highly excited vibrational molecule can be excited even further. Alternatively, the molecule may be deexcited, i.e., transferred to a lower energy level via the process of stimulated emission[104] (c.f. Fig. 3.1) with the overall measured signal being the sum of the two contributions.

In the context of time-resolved spectroscopy, the fundamental property of interest is denoted as the differential optical density, $\Delta OD(\tilde{\nu})$, calculated as the difference between the spectrum of the pure ground state sample $OD_{\text{w/o pump}}(\tilde{\nu})$, depicted schematically in an inverted fashion in blue in Fig. 3.2, and that of the sample after being exposed to the pump pulse, $OD_{\text{w/ pump}}(\tilde{\nu}, t)$ (cf. red spectrum in Fig. 3.2), according to

$$\Delta OD(\tilde{\nu}, t) = OD_{\text{w/ pump}}(\tilde{\nu}, t) - OD_{\text{w/o pump}}(\tilde{\nu}) = \log\left(\frac{\frac{I_0}{I(\tilde{\nu},t)}}{\frac{I_0}{I(\tilde{\nu})}}\right) = \log\left(\frac{I(\tilde{\nu})}{I(\tilde{\nu}, t)}\right). \quad (3.4)$$

Here, accordingly $I(\tilde{\nu})$ and $I(\tilde{\nu}, t)$ refer to the intensities of the transmitted light measured in the absence and after exposure to the UV excitation pulse. Noteworthy, the exact spectrum of the probe pulse is not required. However, it is usually still recorded to account for pulse-to-pulse fluctuations of the laser system.

The differential optical density which is shown as the gray trace in Fig. 3.2 can adopt both positive and negative values. In this context, negative signals are denoted as 'transient' or 'ground state bleaches' (GSB) since the sample becomes optically more transparent in this certain frequency range owing to the depletion of the ground state. Conversely, the sample becomes less transparent for light at frequencies that correspond to transitions of the newly created species or states and the resultant positive signals are

accordingly termed 'transient' or 'induced absorptions' (IA). Usually for either of the two types of signals, their amplitudes, central frequencies and linewidths change over time. This may be attributed to the inherent transient nature of the respective species, i.e., the decay of the corresponding absorption, or the emergence of new species or states resulting from the ensuing photophysical and photochemical processes. Especially the frequently observed shifting along the frequency axis and narrowing of the transient absorption band often can be understood in terms of excited state dynamics such as dissipation of the excessive vibrational energy via intramolecular vibrational energy redistribution (IVR), which entails the redistribution of vibrational energy to lower lying vibrational normal modes.[105] Alternatively, coupling to the energy continuum of the solvent, allows for vibrational relaxation via interaction with the surrounding of the analyte. In general, this dissipation of excess vibrational energy is referred to as vibrational cooling since this process leads to a decrease of the internal temperature of the molecule.[106] In a time-resolved UV/mIR spectrum, this process often manifests itself by a successive blueshifting and reshaping of the induced absorption signals. Usually, molecules tend to accumulate in the well, i.e., in the ground state, of the excited state PES prior to fluorescent relaxation.[107] Therefore, as the population returns to the vibrational ground state on the excited state PES over time, the probe induced vibrational reexcitations become more energy intense due to the anharmonicity of the molecular vibration (c.f Eq. 3.3). Hence, the induced absorptions often tend to reshape and shift to higher energies with increasing t. Still, it should be noted, that vibrational relaxation via emissive pathways would also be possible in principle. However, in bulk media this process is of subordinate role, since the collision frequency between the solute and and the solvent usually exceeds the respective fluorescence lifetime by orders of magnitude, and thus enables much faster energy dissipation to the molecular surrounding by intermolecular energy transfer.

Any bimolecular processes beyond the most basic interactions with the surrounding solvent shell of the analyte require diffusive processes of both involved particles and are usually to slow to be observed in the femtosecond to picosecond range, even for diffusion controlled reactions.[108] Therefore, from a kinetic perspective all the observed processes are either unimolecular or, in case of solvent interactions due to the large excess of the solvent, at least pseudo-unimolecular occurring in a sequential or competing manner.[109] Hence, the solution of the underlying differential rate equations can be expressed as a sum of single-exponential decays according to

$$\Delta OD(\tilde{\nu} = \text{const.}, t) = \Delta OD_{\infty} + \sum_{i} A_i \cdot \exp\left(\frac{t}{\tau_i}\right) \tag{3.5}$$

where i is the number of involved processes responsible for the spectral evolution, τ_i refers to the time constant of this process and A_i represents the amplitude. Note, that A_i itself may be a function of the time constants τ_i, itself.

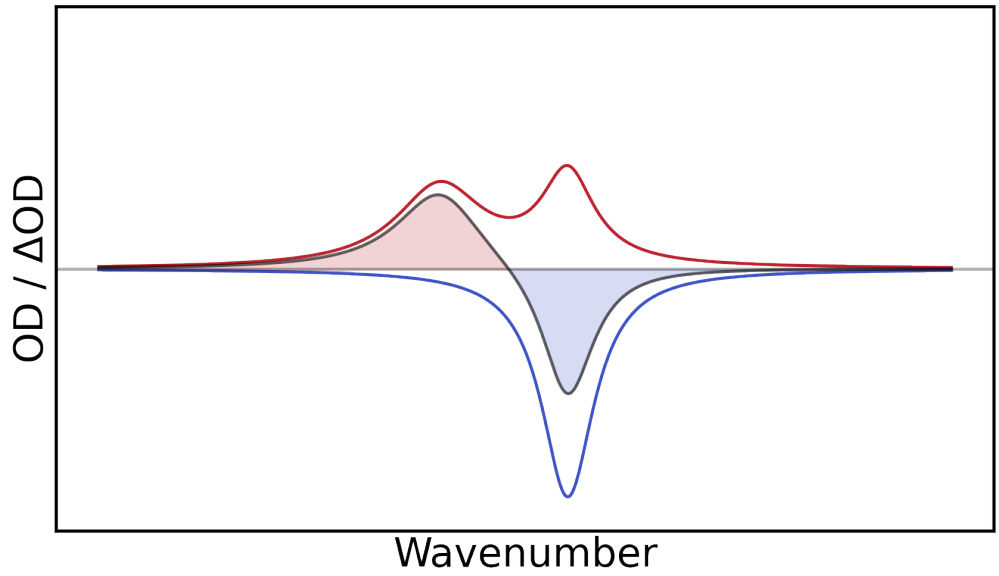

Figure 3.2.: *Schematic visualization of the signal contributions to the observed pump-probe spectrum (in gray). The pump-probe spectrum constitutes the difference between the spectrum of the sample after excitation (red line) and that of the parent (inverted, blue line). Owing to the population of excited states, the absorption characteristics of the sample change. This gives rise to increased or decreased absorption, respectively, in certain ranges of the spectrum which manifests itself in the occurrence of induced absorptions (IA, positive signals, shaded in red) and ground state bleaches (GSB, negative signals, shaded in blue) in the transient spectrum.*

Especially in the context of transition metal chemistry, UV-pump mid-infrared-probe spectroscopy is perfectly suited to unravel the primary processes occurring upon exposure to light. The photochemistry of these systems is often rather complex and features a multitude of different potential doorway states, such as metal-to-ligand charge transfer (MLCT), ligand-to-metal charge transfer (LMCT), ligand centered (LC) and ligand field (LF) states.[100] Therefore, the structural information that can be contributed by UV/mIR spectroscopy are of utter importance. Unsurprisingly, several authors have demanded for applications of this technique in this field for developing an improved understanding[58] of the processes that determine the photochemical behavior of these systems.

4. Experimental Setup

4.1. Stationary Spectroscopy

Prior to the conduction of any sophisticated time-resolved spectroscopic investigation, a thorough understanding of the behavior of the system of interest in its ground state is mandatory. Therefore, the chemical systems investigated in this work were thoroughly characterized by standard spectroscopic and analytical techniques beforehand. Unless stated otherwise, stationary spectroscopic measurements were conducted in liquid solution and at ambient conditions as described in the following.

Vibrational spectra were measured on a commercial Fourier transform infrared (FTIR) spectrometer (Thermo Fisher Nicolet 5700). Routinely, spectra were measured with a spectral resolution of $0.5\,\mathrm{cm}^{-1}$ and averaging over 64 scans. For suppression of signals due to absorptions of water vapor and carbon dioxide in the beam path, prior to any measurement the sample chamber of the spectrometer was thoroughly purged with dry air and the automatic atmospheric correction of the data acquisition software was applied. For the measurement, the solution of the sample in an appropriate solvent was provided in an optical cell consisting of two calcium fluoride windows (CaF_2, Korth Kristall) fixed by two parallel metal sheets. The windows were held apart by an amalgamated lead spacer at a certain distance that ensures the desired optical thickness of the sample. Depending on the solubility of the sample and the extinction coefficients of the solvent, the separation of the CaF_2 windows was adjusted accordingly to achieve a satisfactory absorbance level.

Measurements of electronic absorption spectra in the ultraviolet to visible range (UV/Vis) were carried out on a dual-beam Shimadzu UV-160 spectrometer at a spectral resolution of 1 nm in the range from 200 nm to 1000 nm. Spectra were collected in quartz glass cuvettes (Hellma QS) with an optical path length of 1 mm and were referenced with respect to the solvent. To this end, a cuvette filled with the pure solvent was placed in the optical path of the reference beam to obtain the sole electronic absorption spectrum of the sample.

4.2. UV-Pump Mid-Infrared-Probe Spectroscopy

The femtosecond ultraviolet-pump mid-infrared-probe spectroscopic investigations in the picoseconds to nanoseconds regime presented in this work, were carried out on a

home-built experimental setup as schematically laid out in Fig. 4.1. In short, the technical realization of the measurements will be described.

The experiment can be operated either by one or two identical Ti:sapphire lasers (Solstice Ace, Newport) depending on the exact experimental requirements such as the range of desired pump-probe delays to cover. The front-end lasers provide light pulses centered at 800 nm with pulse durations of about 50 fs at a repetition rate of 1 kHz. The pump and the probe light are generated via nonlinear optical processes. This approach nowadays has become a standard method and is routinely applied in this field. Therefore, a detailed elaboration on the underlying physical principles is beyond the scope of this thesis and the interested reader is referred to the literature.[110–112]

For the generation of the mid-infrared probe light, a fraction of the front end's output with an optical power of about 300 mW is directed into a a home-built optical parametrical amplifier (OPA) whose design is based on a setup by Hamm and coworkers. In short, it enable the splitting of 800 nm pump photons (p) into signal (s) and idler (i) photons such that $\nu_p = \nu_s + \nu_i$. The latter two are subsequently subject to difference frequency generation which yields the required mid-infrared probe pulses that were utilized in the ultrafast spectroscopic studies. A detailed technical description of the OPA was provided in the literature previously and will therefore be omitted here.[113–115]

Measurement of UV-Pump mIR-Probe Spectra

The thus generated mid-infrared beam is used to probe the excited state dynamics or photochemical processes in a time-resolved UV-pump mIR-probe experiment. Prior to any measurement the experimental setup has to be tuned carefully to ensure it functions properly by setting for instance the temporal and spatial overlaps of the beams correctly. A schematic drawing of the relevant optical components is provided in Fig. 4.1 and its operation is described in the following.

The required UV excitation light, (uv) is generated as per requirements. Based on the desired wavelength the generation of the pump light can be realized by several different nonlinear optical processes. For all the studies presented in this work, however, UV excitation at a wavelength of 266 nm was applied. For this purpose, the 800 nm fundamental beam was subject to third-harmonic generation (THG), i.e., a first frequency doubling step in a nonlinear phase I β-barium borate (BBO) crystal followed by sum-frequency mixing of the resultant light at 400 nm with a second fraction of the laser system's fundamental.

For excitation of the sample, the pump beam is directed into the measurement cell. To this end, first, the beam passes a chopper disk, C, whose rotational frequency is matched to the repetition rate of the laser and by its design ensures that every other pump pulse is blocked. This way, it is possible to measure the intensity of the IR probe light on the detector with and in absence of the pump light, $I_{\text{w/ pump}}(\tilde{\nu})$ and $I_{\text{w/o pump}}(\tilde{\nu})$, respectively, which allows the calculation of the differential optical density $\Delta\text{OD}(\tilde{\nu})$ as

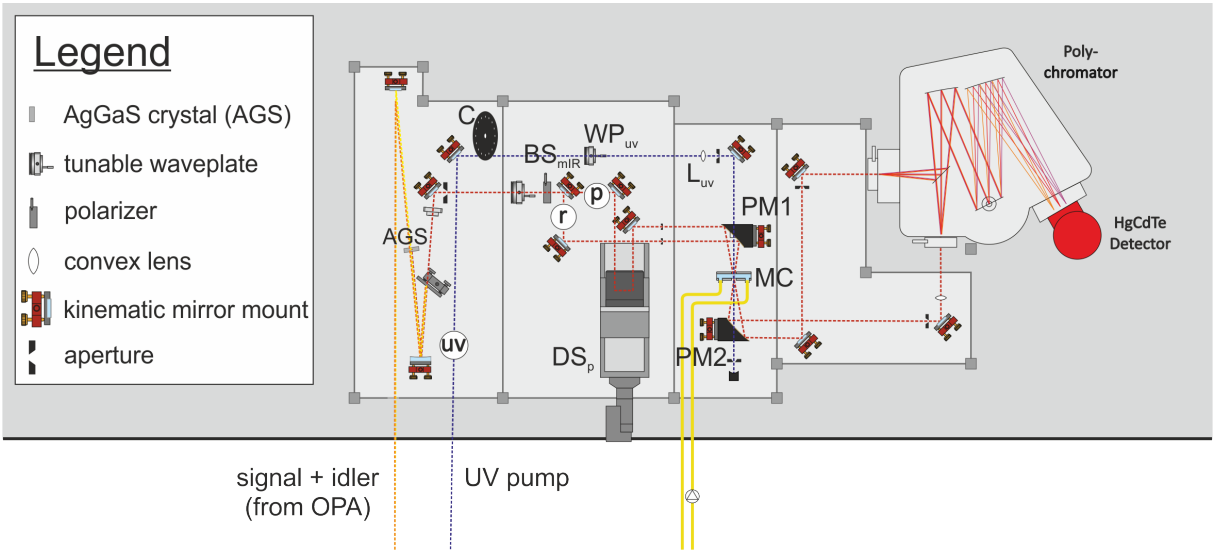

Figure 4.1.: *Schematic drawing of the optical setup of the UV-pump mid-infrared-probe experiment for the collection of time-resolved pump-probe spectra used throughout this work. Abbreviations: BS = beam splitter/dichroic mirror, L = lens, DS = delay stage, PM = parabolic mirror, AGS = silver gallium sulfide crystal, C = chopper disk, WP = waveplate, MC = measurement cell*

described in Chapter 3. To cancel out signal contributions brought about by rotational diffusion, the polarization of the pump beam is then rotated by the magic angle of 54.7° with respect to the probe light using a tunable half-wave plate (WP_{uv}). Subsequently, the pump light is focused into the sample cell MC by a convex lens (L_{uv}, f=400 mm). To realize homogeneous illumination and to avoid excessive sample decomposition that may lead to deposition on the windows of the measurement cell, the focal point is set slightly behind the cell. This way it is also ensured that a sufficiently large sample volume is excited and that only illuminated sample is probed. In fact, sample decomposition is frequently encountered during exhaustive exposure of the sample of interest to UV light. To prevent distortion of the measured signals due to the deposition of photoproducts on the windows, in addition a flow-through cell is used which allows for constant exchange of the sample by a gear pump. The assembly of the measurement cell, in turn, consists of two calcium fluoride windows (Korth Kristalle) held apart by an amalgamated lead spacer that determines the optical thickness of the sample and is chosen as required.

To probe the response of the sample to the UV excitation, the mIR beam is first directed onto a 50:50 beam splitter, BS_{mIR}, to create two replica pulses. Whereas the transmitted probe beam, (p), is used to monitor the spectral changes induced by the pump pulse, the reflected reference beam, (r), is utilized for internal calibration to account for fluctuations of the laser output power. Subsequently, the probe beam is directed over a motorized translation stage equipped with a corner cube (DS_p) to introduce an optical delay with respect to the pump pulse. A pair of two gold off-axis parabolic mirrors, PM1 and PM2 is then used first to steer and focus the reference and the probe mIR pulses into the excited sample volume at an angle of incident of 5° relative to the UV beam and then for recollimation of the beams. Either of the two beams subsequently

are directed and focused onto the entrance slits of a HORIBA Jobin Yvon iHR320 polychromator equipped with a liquid nitrogen cooled 2 × 32 pixels mercury cadmium telluride (MCT) detector (Infrared Associates MCT-6400). Readout of the electric signals is realized by a home-built 64 channel amplifier and three AD cards (DT 3016, Data Translation) in a computer.

The stage used in this experiment to ensure the temporal delay of the probe pulse is limited to a maximum travel range of 30 cm and thus sets an upper limit to the accessible pump-probe delays. Taking a double pass approach, i.e., directing the beam over the delay stage at a slight vertical displacement, which translate into an effective additional path length of 1.2 m (2×(2×30 cm)), a maximum pump-probe delay of roughly 4 ns can be realized. However, although simply using an even longer delay stage might seem as a feasible solution to this problem, it is important to stress out, that controlling the collimation of the probe beam over extended distances constitutes a real experimental challenge and therefore is only applicable to pump-probe delays in the regime of femtoseconds to a few nanoseconds. Therefore, unfortunately, due to technical and optical limitations, the measurement of time-resolved spectra at pump-probe delays above 4 ns simply by optically delaying the probe pulse via the delay stage is impracticable.

Yet, often the relevant photophysical and photochemical processes of interest occur on timescales that cover several orders of magnitude from the picosecond up to the microsecond regime. In these cases, even longer pump-probe delays were of interest. To get access to these time regimes the system had to be driven by a dual laser configuration. For this purpose, two regenerative amplifiers (RGA) (Newport Solstice Ace) were pumped by the same mode-locked Ti:Sapphire seed laser (Newport Spectra Physics Mai Tai) that is operated at a repetition frequency of 83 MHz. After stretching, amplification and recompression of the pulses, dramatic increases in the pulse energies and alterations to the repetition rate can be realized. Here, the output of the first RGA is used for generation of the UV pump light, while the output of the second one is converted to provide the mid-infrared probe light. Using a digital delay generator (DG535, Stanford Research Systems, Inc.) connected to the mode-locked seed laser, the pulse to enter the second RGA can be selected. This way the probe pulses can be delayed electronically with respect to the other laser system in increments of the repetition period of the seed laser of 11.83 ns (1/83 MHz). In principle, this enable virtually arbitrarily long delays between both system, the only limitation being the constant repetition frequencies of the two RGA systems of 1 kHz that sets the maximum realizable delay in the range of 1 ms.

However, for special cases it was realized that the key events in the photophysical or photochemical mechanism occur in the intermediate time range from 4 ns to 11.83 ns that is accessible by neither of the aforementioned approaches. Instead, in order to cover this range of pump-probe delays, the optical path of the pump beam was shortened by a well-defined amount. This way, it is ensured that the pump pulse reaches the

sample at an even earlier point in time relative to the probe pulse. Thereby, the delay between the two is effectively increased by a constant value $\Delta\tau$ that is related to the shortening in the optical path. To be as precise as possible, in the respective cases, the delay introduced by this approach can be determined using a fast oscilloscope whose trigger is provided by the probe pulse. This additional time delay can then directly be measured and constitutes a constant offset that is additive to the delay introduced by the movement of the delay stage. Following this approach, the effective time window can be stretched to delays as long as roughly 10.5 ps.

Although the full range of pump-probe delays can not be measured in a single run, still following these three approaches pump-probe spectra can essentially be measured from the femtosecond to the microsecond regime and thus span at least 9 orders of magnitudes.

5. Photophysics and Photochemistry of trans-Bis(acetylacetonato)azido pyridine cobalt(III)

As a representative of electron rich octahedral azido complexes, in this work the photophysical and photochemical properties of the system *trans*-bis(acetylacetonato)azidopyridinecobalt(III) (*trans*-$Co(acac)_2(N_3)(py)$, where acac = acetylacetonato, py = pyridine) (*trans*-[**1**]) were explored in more detail. From a photochemical perspective, this complex is particularly interesting since the acetylacetonato moiety is known to be a redox-noninnocent ligand[116] and can hence engage into intracomplex redox chemistry. This in turn, can have direct implications on the excited state dynamics because of the availability of additional charge-transfer states that should be readily accessible. This in turn may alter the overall photoreactivity, especially concerning the azido moiety. To elaborate on this influence, time-resolved spectroscopic investigations were conducted on the system. The results of these studies have been published[117,118] and will be presented in greater detail the following.

5.1. Synthesis

The complex was synthesized following a procedure devised in the literature by Boucher and Herrington[119] with minor modifications. An overview of the starting materials used for the chemical syntheses, their sources and purities is compiled in Appendix B. All materials were used as received without any further purification.

In a 500 mL round bottom flask 4.0152 g of anhydrous bis(acetylacetonato) cobalt(II) (15.6 mmol, 1.00 eq., pink powdery solid, $C_{10}H_{14}CoO_4$) were suspended in 300 mL of demineralized water. 2.0312 g of sodium azide (31.2 mmol, 2.00 eq., colorless crystalline solid, NaN_3) were added to the pink aqueous suspension while stirring vigorously followed by the subsequent addition of 4.0 mL of pyridine (49.5 mmol, 5.2 eq., pale yellow liquid, C_5H_5N).

Then, 3.5 mL of an aqueous solution of hydrogen peroxide (35 %) (49.5 mmol, 3.2 eq., colorless liquid, H_2O_2) was added dropwise which led to darkening of the solution. After the addition was finished, the solution was stirred vigorously at room temperature for 2 h. Once the reaction was complete, to precipitate the product further, the

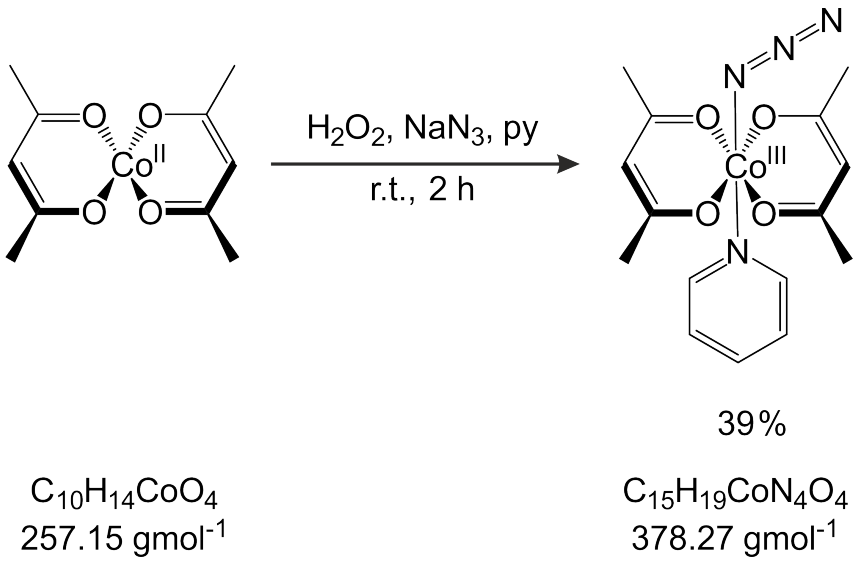

Figure 5.1.: *Synthesis of trans−[Co(acac)2(N3)(py)]. Starting from the Co(II) source, the target complex is readily obtained in a trans selective fashion via oxidation by hydrogen peroxide in presence of the pyridine and the azide ligands.*

dark solution was concentrated by removal of 125 mL of water on a rotary evaporator. Subsequently, the dark precipitate was filtered off and dried at 50 °C in vacuo.

For further purification, the crude product was then dissolved in just enough chloroform (roughly 80 mL) and reprecipitated by slow addition of a fourfold amount of *n*-hexane. The precipitate was allowed to settle down and was subsequently filtered off from the solution.The yellow-brownish solid compound was then washed with *n*-hexane (2×20 mL) and subsequently dried under vacuum at 50 °C for 5 h. The product was obtained as a brown powdery solid in 39 % yield (2.3261 g) with respect to the starting cobalt(II) complex.

Analytical Characterization

Elemental Analysis: *Anal. Calcd.* for $C_{15}H_{19}CoN_4O_4$: C, 47.63; H, 5.06; N, 14.81. Found: C, 46.11; H, 5.00; N, 14.54.

^{1}H-NMR: (500 MHz, $CDCl_3$, 298 K): δ (ppm) = 2.18 (s, 12H, acac, $COCH_3$), 5.36 (s, 2H, acac, $CO(CH)CO$)), 7.42 (m, 2H, py, $C_{3,5}H$)), 7.86 (m, 1H, py, C_4H)), 8.52 (m, 2H, py, $C_{2,6}H$)

^{13}C-NMR: (500 MHz, $CDCl_3$, 298 K): δ (ppm) = 26.7 ($COCH_3$, acac), 98.0 ($CO(CH)CO$, acac), 124.3 ($C_{3,5}$, py), 138.5 (C_4, py), 152.3 ($C_{2,6}$, py), 190.2 (CO, acac)

IR: (22 °C, CH_2Cl_2): $\tilde{\nu}$ (cm^{-1}) (ϵ, $L\,mol^{-1}\,cm^{-1}$) = 1356 (473) ($\nu_s(N_3^-)$), 1384 (1274) ($\delta_s(CH_3)$, acac), 1430 (324) ($\delta_{as}(CH_3)$, acac), 1452 (583) ($\delta(CH_3)$, acac), 1487 (155) ($\delta_{in-plane}$ (ring), py), 1522 (3258) (ω(C−H) + ν_{as}(C=C=C) (A'), acac), 1575 (1609)

(ν_{as}(CO) (A''), acac), 1608 (170) (ν_s(C≡C), py), 2021 (2965) ($\nu_{as}(N3^-)$)

UV-Vis: (22 °C, CH_2Cl_2): λ_{max} (nm) (ϵ, L mol^{-1} cm^{-1}) = 268 (19000) ($\pi_{acac} \rightarrow d^*_{x^2-y^2}$), 334 (10940) ($\pi_{azide} \rightarrow d_{z^2}$), 450 (1310) ($^1A_g \rightarrow^1 E(1)/^1B_{2g}$) 575 (278) ($^1A_g \rightarrow^1 E(1)$)

5.2. Molecular and Spectroscopic Properties

5.2.1. Single Crystal X-Ray Diffraction Studies

By means of single crystal X-ray diffraction, it was possible to determine the molecular structure of the complex in the solid state. Suitable crystals were obtained as clear red plates grown from a saturated solution of *trans*-[**1**] in dichloromethane at 4 °C within a few hours. X-ray diffraction measurements were carried out on a Bruker X8-Kappa Apex II diffractometer using Mo-K_α radiation ($\lambda = 0.710\,73$ Å).

The complex molecule was found to crystallize in space group $P2_1/n$ of the monoclinic crystal system including one dichloromethane solvent molecule in the asymmetric unit. Crystallographic data of *trans*-[**1**] are compiled in Tab. 5.1 and the experimentally determined solid state molecular structure is depicted in Fig. 5.2. Several structural parameters such as selected bond length, bond angles and dihedrals of the molecular geometry in the crystalline phase are presented in Tab. 5.2.

Table 5.1.: *Crystallographic parameters of trans-*[*1*] *as determined from single crystal X-ray diffraction. The system was observed to crystallize in the monoclinic crystal system with Z = 4 molecules in the unit cell. Specification of crystal axes and angles in the unit cell according to usual conventions.*

crystallographic parameter	*trans*-[**1**]
crystal system	monoclinic
space group	$P2_1/n$
a / Å	11.1873(4)
b / Å	14.5307(5)
c / Å	13.4946(5)
α / °	90
β / °	114.2370(10)
Z	4

The observed structure reveals, that the synthesis furnishes the complex in a *trans* configuration with the azide and the pyridine ligand occupying opposing sides of the coordination octahedron across the cobalt center. Thus, the complex adopts C_s symmetry with the pyridine, the azide ligand as well as the cobalt central ion lying on the σ_s mirror plane.

Table 5.2.: *Structural parameters of trans-[**1**] as determined from single crystal X-ray diffraction. Bond lengths are in Å, bond angles and dihedral angles are in °.*

structural parameter	*trans*-[**1**]
$N_\beta - N_\gamma$	1.156
$N_\alpha - N_\beta$	1.206
$N_\alpha - Co$	1.948
$N(py) - Co$	1.957
$N_\alpha - N_\beta - N_\gamma$	177
$N_\beta - N_\alpha - Co$	117
$N_\alpha - Co - N(py)$	178
$O(1) - Co - O(2)$	96
O(1)–Co–O(1′)	84
C(1)–O(1)–O(1′)–C(1′)	152
$O(1) - Co - N(py) - C(py)$	–40
$N_\beta - N_\alpha - N(py) - C(py)$	176

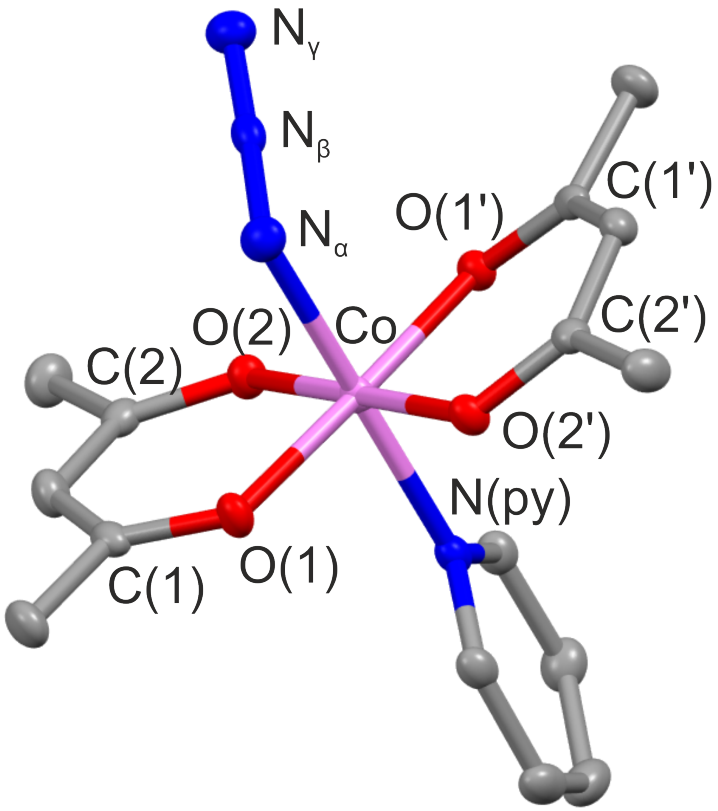

Figure 5.2.: *Molecular structure of trans-[**1**] as determined from single crystal X-ray diffraction. Hydrogen atoms are omitted for clarity. Carbon in gray, nitrogen in blue, oxygen in red and cobalt in violet.*

Interestingly, the two improper dihedral angles C(1)–O(1)–O(1′)–C(1′) and C(2)–O(2)–O(2′)–C(2′) deviate significantly from 180°, i.e., the two acetylacetonate ligands do not lie in one plane but are to some extent tilted away from a perfectly planar arrangement towards the hemisphere of the azido ligand. Most likely, this geometry is adopted in order to reduce the steric stress otherwise encountered due to the close vicinity to the pyridine ligand.[1]

The slight discrepancy between the bond lengths of the $N_\alpha - N_\beta$ (1.206 pm) and the $N_\beta - N_\gamma$ (1.156 pm) bonds should be stressed out particularly. As pointed out in section 2.1, an elongation of the $N_\alpha - N_\beta$ bond is a commonly observed feature of highly unstable azido compound and is often regarded to facilitate the cleavage of the azide moiety releasing dinitrogen from the complex. Still, opposed to other literature-known azido compounds, in this case the relative elongation is still comparably small which may be taken as an indication of relatively high thermal and photochemical stability. This interpretation is also corroborated by the fact that the complex was observed to exhibit no explosive properties but instead could be heated to temperatures as high as 170 °C before thermal decomposition set in. Still, many of the structural features discussed before (c.f. section 2.1) are likewise observed here. Thus, the regular $Co - N_\alpha - N_\beta$ angle amounts to 117° and thus is well in the regular range. Moreover, here the azido ligand also deviates from perfectly linear arrangement by 4°.

5.2.2. NMR Spectroscopy

As revealed by the X-ray diffraction studies discussed above, the system adopts a *trans* configuration, thus rendering the complex C_s symmetric. The cobalt ion exhibits a d^6-electron configuration in the complex. As in almost all cases for Co(III) systems, the inherent ligand field splitting is sufficiently high to outrule the effects due to the ligands and thus usually a low-spin configuration is energetically favored. In fact, only in few selected cases a high-spin configuration for Co(III) is reported.[30] Thus, the diamagnetic character of the complex renders it suitable for nuclear magnetic resonance spectroscopy (NMR). The proton ^{1}H-NMR of the complex was recorded in a deuterochloroform ($CDCl_3$) solution. It should be pointed out, that the measurement was conducted with a freshly prepared solution (no older then a few minutes) because the spectrum as shown in Fig. 5.3 was observed to change over time.

In total, five resonances are observed which occur at 2.18 ppm, 5.36 ppm, 7.42 ppm, 7.86 ppm and 8.52 ppm, respectively. Here, the high-field signal at 2.18 ppm can readily be attributed to the methyl resonances of the acetylacetonate ligands. Although, owing to the C_s symmetry, the methyl groups are only pairwise equivalent, apparently the chemical shifts are still sufficiently similar to let the signals collapse into a single reso-

[1] Interestingly, except of the Truhlar meta hybrid mPW1B95 functional, frequently applied density functionals fail to correctly describe this arrangement. Therefore, for the system at hand this level of model chemistry was employed for quantum chemical calculations.

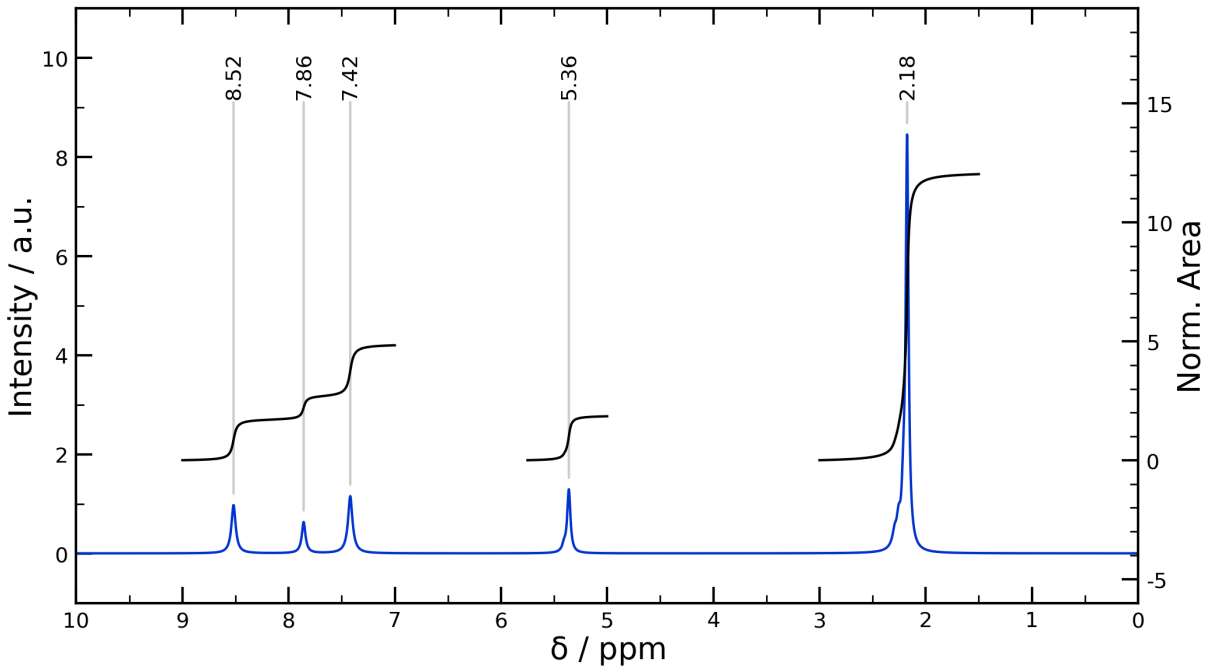

Figure 5.3.: *NMR spectrum of trans-*[*1*] *recorded in liquid $CDCl_3$ solution. For clarity residual solvent peaks have been removed. Owing to the trans configuration of the complex all methyl resonances collapse into a single peak at 2.18 ppm that integrates to 12 protons. The methine resonances are observed at 5.36 ppm at a relatively large chemical shift due to the electron withdrawing nature of the adjacent carbonyl groups. The resonances of the protons in ortho, meta and para position of the pyridine ligand, however, are observed in the typical range for aromatic protons and peak at 8.52 ppm, 7.42 ppm and 7.86 ppm, respectively.*

nance whose integral weight equals 12 protons. Notably, at the resolution the spectrum was recorded at no ^{4}J couplings to the protons of the methine CH groups are observed, hence the signal appears as a simple singlet. Similarly, the resonances of the methine protons, i.e., the hydrogen atoms of the C-H moiety in between the two carbonyl groups, are found at 5.36 ppm. The resonances which can be attributed to the hydrogen atoms of the pyridine ligands are observed shifted well into the deep field in the typical range from 7 ppm to 9 ppm for aromatic protons. Whereas, the signal of the protons in *meta* positions with respect to the nitrogen heteroatom, i.e., at C3 and C5, occurs at 7.42 ppm, the resonance due to the protons in *ortho* positions is observed at 8.52 ppm. The peak at 7.86 ppm, however, integrates to one proton only and is therefore readily assigned to the hydrogen atom in *para* position. Overall, the *trans* configuration of the complex is also corroborated by the NMR spectrum of the compound as symmetrically equivalent moieties collapse into common signals, hence giving rise to a comparably simple spectrum.

5.2.3. FTIR Spectroscopy

Moreover, the complex of interest was investigated by means of vibrational spectroscopy. For this purpose, a solution of *trans*-[**1**] in dichloromethane ($c = 13.7\,mmol\,L^{-1}$) was freshly prepared and its FTIR spectrum shown in Fig. 5.4b) was measured as described before (c.f. section 4.1).

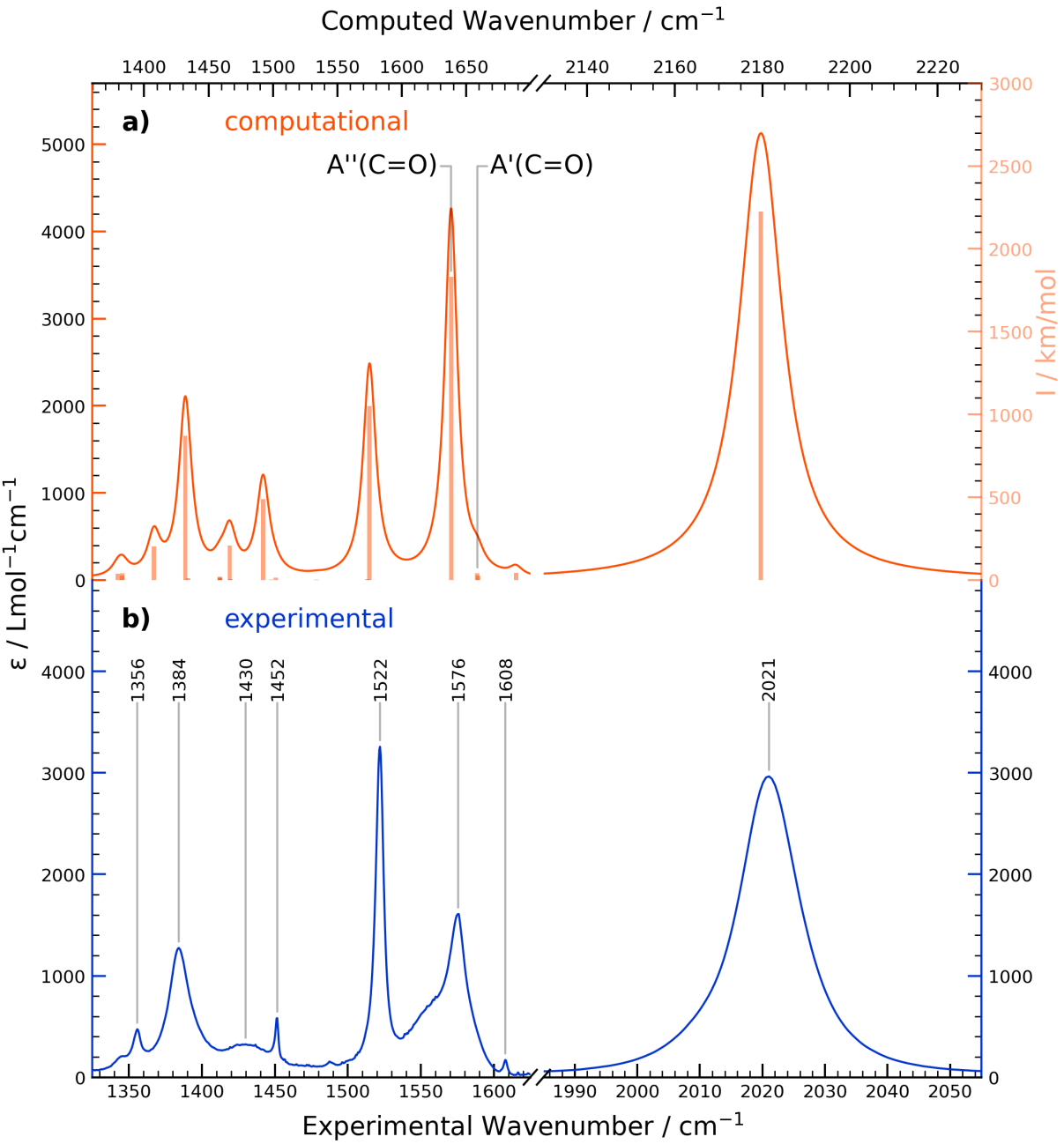

Figure 5.4.: *FTIR spectrum of a freshly prepared solution of trans-[**1**] in liquid dichloromethane at room temperature (20 °C) (b) and comparison with computed IR spectrum (a). Note the axis break in the abcissa. For clarity only the spectral ranges of the carbonyl stretching and the asymmetric azide stretching mode are shown.)*

The assignment of vibrational bands presented in Tab. 5.3 was based on knowledge from the literature[120] and was further corroborated by density functional theoretical (DFT) calculations on the mPW1B95/def2-TZVP level of theory in ORCA 5.0.2. Opposed to standard functionals, Truhlar's meta-hybrid functional proved to perform particularly well in the prediction of the molecular structure and was therefore also employed to evaluate the vibrational spectrum. A simulated spectrum (c.f. Fig. 5.4a)) was obtained from the computed transition frequencies and transition moments assuming Lorentzian lineshapes with a full width at half-maximum (FWHM) of 12 cm^{-1}. The spectrally most prominent normal modes of the compound are visualized in Fig. 5.5.

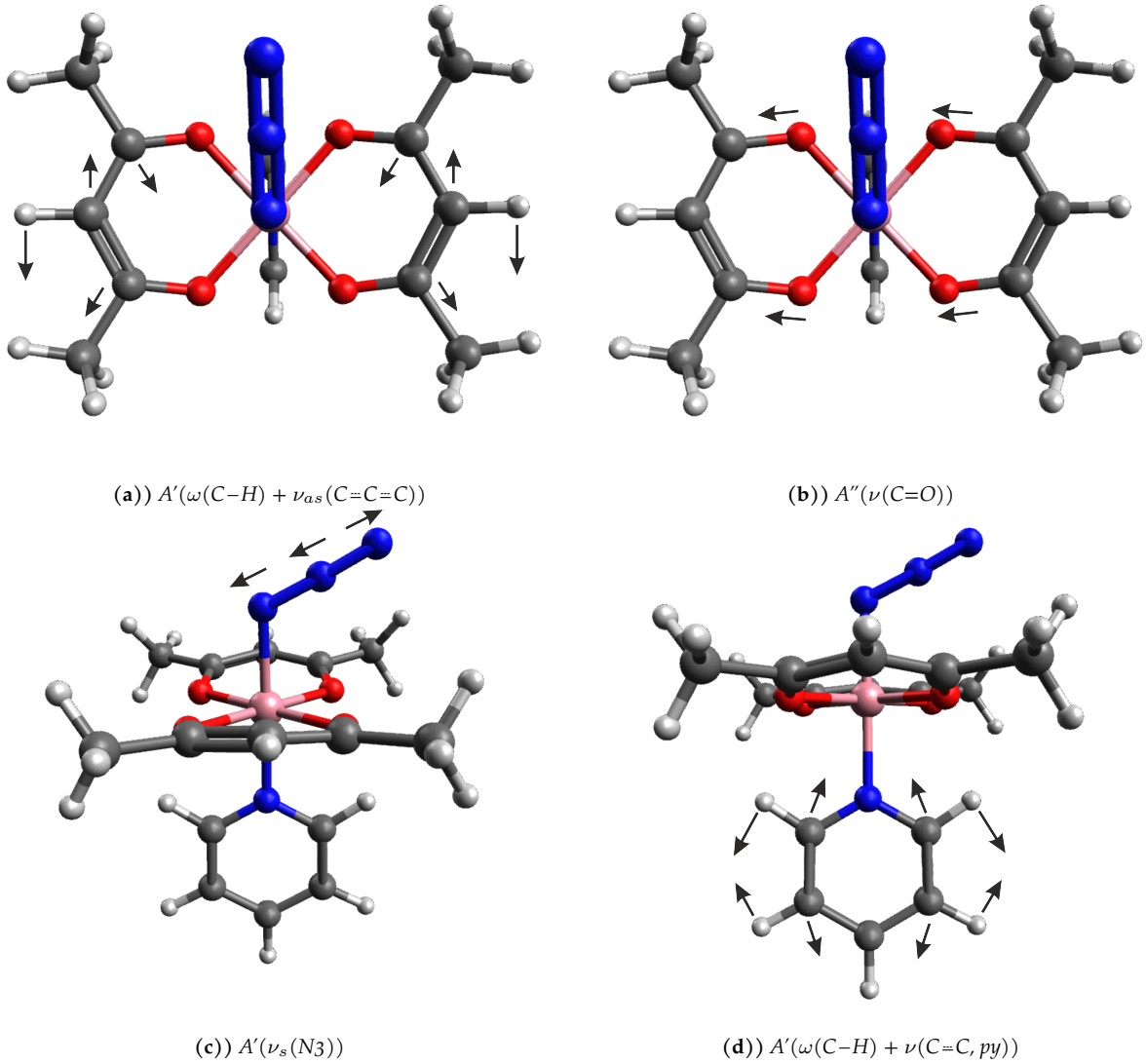

Figure 5.5.: *Representation of selected normal modes of trans-*[***1***]*. Displacement vectors indicate the motion of atoms during a certain vibrational motion. Atom coloring: Cobalt in violet, nitrogen in blue, oxygen in red, carbon in gray and hydrogen in white.*

The C_s symmetry of the molecule ascertained both by X-ray crystallography and NMR spectroscopy likewise has direct implications on the vibrational spectrum of the compound. Thus, within this point group the vibrational normal modes of the molecule can be divided into two classes. In accordance with group theoretical conventions, vibrations whose atomic displacements preserve the C_s symmetry are classified as A′, whereas normal modes that are antisymmetric with respect to the mirror plane in between the two acac ligands belong to the class A″.

The experimental liquid phase spectrum is dominated by three particular absorption peaks which are located at 1522 cm^{-1}, 1575 cm^{-1} and 2021 cm^{-1}. Especially, the two former bands are very characteristic and are frequently observed in the infrared spectra of metal complexes containing coordinated acetylacetonato ligands and are visualized in Fig. 5.5a) and Fig. 5.5b), respectively. Here, the sharp peak at 1522 cm^{-1} arises from a combination of the in-plane wagging of the inner methine (CH) group

and the asymmetric stretch of the acac backbone C=C=C and is of A' symmetry. The band at 1575 cm^{-1}, however, can be classified as A''(ν(C=O)),[120] i.e., it is brought about by the antisymmetric combination of the carbonyl stretching modes of the acac ligands across the cobalt center. Still, a closer inspection of this band reveals a peculiar shape of its absorption profile. In particular, it appears as if the peak exhibits a shoulder at its low frequency edge. This peculiarity may be explained by the molecular geometry of the system. Hence, according to its X-ray structure and further corroborated by theoretical calculations, the two acac ligands are expected to tilt to some extent towards the azido ligand thereby generating an almost boat-like geometry. In the ideal case of a perfectly planar arrangement of the acac ligands, the $Co(acac)_2$ unit should exhibit an inversion center that within this geometry would clearly prohibit any A'(ν(C=O)) mode to be IR active. These qualitative considerations are corroborated by the theoretical calculations which predict the A'(ν(C=O)) to exhibit only a minute transition dipole moment. However, due to this inclination and probably further fostered by solvent effects, the transition dipole moment of these vibrational modes is slightly increased to some extent which may give rise to the peculiar shape of the band.

The peak of the very characteristic asymmetric vibration of the azide ligand (c.f. Fig. 5.5c)) in turn is observed at 2021 cm^{-1}. This band is located in the typical range of terminally coordinated azide ligands[120] and that of similar compounds of the type $Co(acac)_2N_3L$ (where L is any another ligand). Besides that, also the symmetric azide band is observable and is located at 1385 cm^{-1} in a range well known for this molecular group. In line with usual observations, the corresponding peak is rather weak, owing to the fact that the change in dipole moment induced by this vibration is much lower. Apart from that, a few more absorptions can be identified which essentially are related to the pyridine or the less specific normal modes of the acac ligands and their assignment is given in Tab. 5.3.

Table 5.3.: *Pronounced vibrational normal modes of trans-[**1**]. The assignment of the experimentally observed peaks was corroborated by quantum chemical calculations on the mPW1B95/def2-TZVPP level. Calculated frequencies are presented for comparison.*

		$\tilde{\nu}$ / cm^{-1}			
mode	sym.	exp.	comp.	ϵ / $L\,mol^{-1}\,cm^{-1}$	I / $km\,mol^{-1}$
$\nu_s(N3)$	A′	1356	1408	473	203
$\delta(CH3)$	A′	1384	1432	1274	872
$\delta(CH3)$	A″	1430	1466	324	210
$\delta_{as}(CH3)$	A′	1452	1492	583	488
$\omega(C{-}H) + \nu_{as}(C{=}C{=}C)$	A′	1522	1575	3258	1052
$\nu(C{=}O)$	A″	1575	1638	1609	1832
$\nu(C{=}O)$	A′	—	1659	—	42
$\omega(C{-}H) + \nu(C{=}C, py)$	A′	1608	1689	170	44
$\nu_{as}(N3)$	A′	2021	2180	2965	2224

5.2.4. UV/Vis Spectroscopy

To explore the electronic structure of *trans*-[**1**], the UV/Vis spectrum of the complex was recorded in dichloromethane solution ($c = 0.33\,mmol\,L^{-1}$). The measurement was conducted as described before (c.f. section 4.1), and the experimentally observed spectrum is depicted in Fig. 5.6 b). To support the peak assignment and to investigate the exact nature of the transitions observed in the experimental spectrum, time-dependent density functional theory (TDDFT) on the ωB97X-D/def2-TZVPP level of theory was applied. Based on these results, the spectrum of the compound was simulated assuming Gaussian lineshapes with a FWHM of $5000\,cm^{-1}$ which is shown in Fig. 5.6a). Moreover, selected difference densities[121] employed to ascertain the nature of the observed transitions are plotted in Fig. 5.7. The overview of the most prominent absorption bands and their assignment is provided in Tab. 5.4.

In general, the UV/Vis spectrum can be divided into two parts based on the energy at which pronounced absorptions are observed. Here, the lower energy region below $25\,000\,cm^{-1}$ (above 400 nm) essentially is governed by *d-d*-excitations of the metal center which are observable in the spectrum and peak at 450 nm and 575 nm, respectively. In line with usual observations, the extinction coefficients attributed to these bands are rather small and amount to no more than $300\,L\,mol^{-1}\,cm^{-1}$ owing to the small transition dipole moments. In fact, these transitions are usually considered to be Laporte forbidden, because of the identical parity of the involved atomic orbitals.[91,122–124] Notwithstanding, it should be noted, that this consideration strictly speaking only holds for centrosymmetric complexes. Still, to a good approximation the *d*-orbitals of the metal can reasonably well be treated independently of the rest of the electronic structure. Hence, it is only due to the interaction with the ligands that this selection rule is weakened to

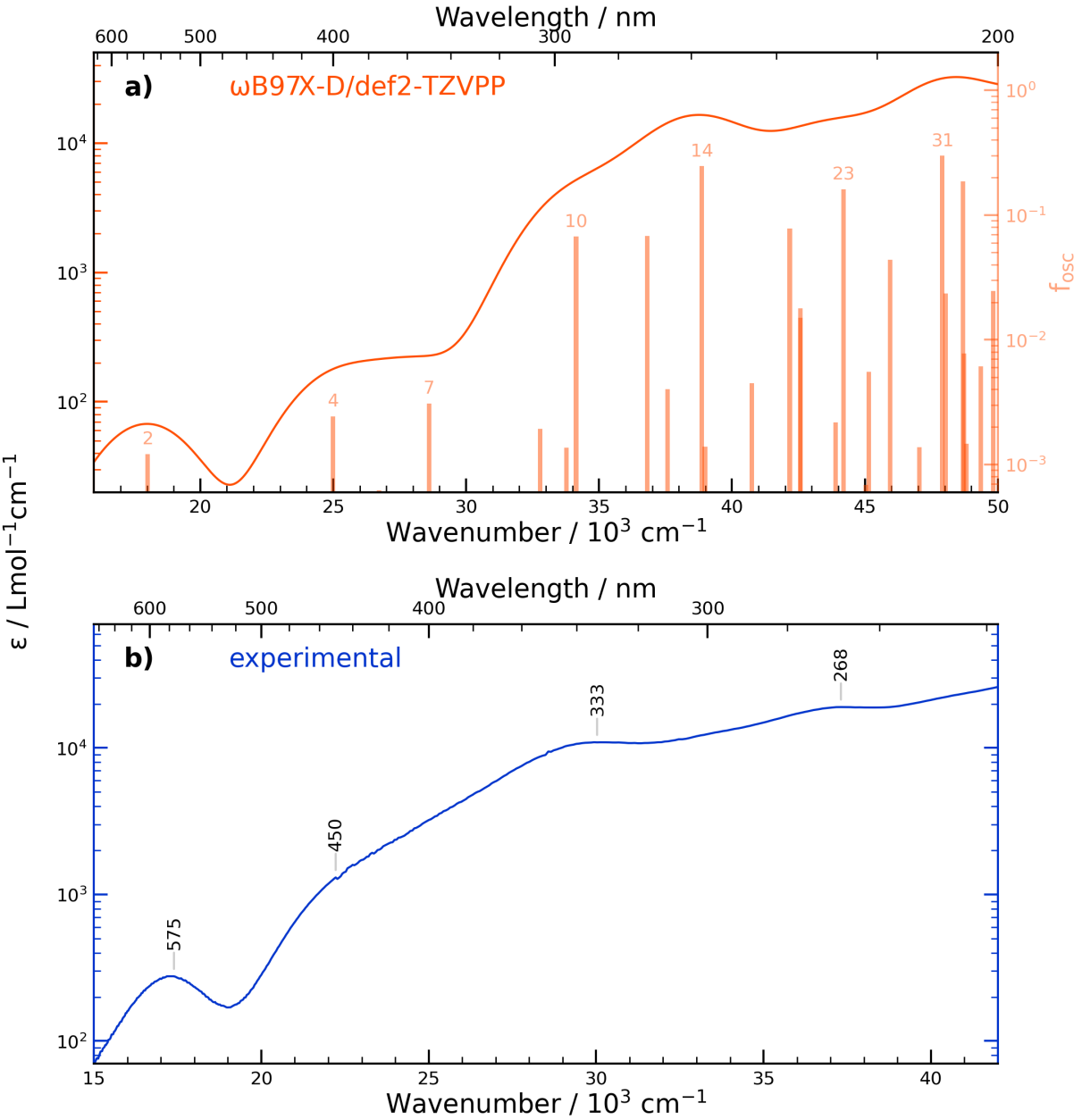

Figure 5.6.: *UV/Vis spectrum of a freshly prepared solution of trans-*[**1**] *in liquid dichloromethane at room temperature (20 °C) (b) and comparison with computational TDDFT spectrum (ωB97X-D/def2-TZVPP) (a).*

some extent, thereby rendering these transitions some non-zero transition dipole moment albeit the transitions are still weak in nature.

As is evident from the fact, that the NMR spectrum of *trans*-[**1**] can readily be measured without any complications, the cobalt center apparently exhibits a low-spin d^6-electron configuration. In the recent past, the electronic structure of such Co(III) low-spin systems was more thoroughly scrutinized by a complete active space self-consistent field treatment in combination with second order *n*-electron valence perturbation theory (CASSCF/NEVPT2).[125] As stated before, to a good approximation the d-electrons can be treated independently and therefore the findings of this study can be transferred to the system at hand to likewise rationalize the electronic structure of the metal center.

Table 5.4.: *Electronic transitions of trans-[**1**] as observed in the experimental UV/Vis spectrum and comparison with results from TDDFT calculations on the ωB97X-D/def2-TZVPP level.*

root	λ_{max} / nm		intensity	
	exp.	comp.	ϵ / L mol^{-1} cm^{-1}	f_{osc} (comp.)
23	268	227	19000	0.1598
14	334	258	10940	0.2486
4	450	399	1310	0.0026
2	575	555	278	0.0012

Accordingly, the *d-d*-transitions peaking at 575 nm and 450 nm thus can be assigned to transitions of the ^{1}E(1) $\leftarrow$ ^{1}A$_g$ and ^{1}E(1)/^{1}B$_{2g}$ $\leftarrow$ ^{1}A$_g$ types, respectively, which in fact was further corroborated by the TDDFT calculations mentioned before. In silico, these two bands are found as roots 2 and 4. In particular, root 4 corresponding to the peak at 450 nm in the experimental spectrum can be classified as the transition to a metal centered excited state, ^{1}MC, based on the theoretically calculated difference transition density (c.f. Fig. 5.7b)).

Overall, the spectrum is still dominated by strong absorptions in the ultraviolet spectral range above 25 000 cm^{-1} (below 400 nm) of which the absorption features peaking at 334 nm and 268 nm are the most prominent. According to the theoretical results, this range of the spectrum is essentially governed by charge transfer transitions. In particular, the band peaking at 334 nm that features a strong extinction coefficient of roughly 10 940 L mol^{-1} cm^{-1} was found to correspond to an azide-to-cobalt charge transfer transition based on theoretical results (root 14, c.f. Fig. 5.7d)). More precisely, upon excitation electron density from the azide π-orbital oriented in the Co−N=N=N plane is promoted into the vacant d_{z^2}-orbital on the metal, and is therefore denoted as ^{1}LMCT$_{\text{azide}}$. Transitions located at even higher energy, in turn, were found to exhibit essentially acac-to-cobalt charge transfer character. Especially the absorption observed at 268 nm in the experimental spectrum, that corresponds to root 23 in the calculation (c.f. Fig. 5.7e)), exhibits a large extinction coefficient of about 19 000 L mol^{-1} cm^{-1} and is therefore identified as a strongly allowed transition. Based on the analysis of the corresponding difference transition density, this excitation involves redistribution of electron density from the *p*-orbitals on the acac oxygen atoms into the antibonding $d_{x^2-y^2}$-orbital of the metal.

As is evident, several electronic states can in principle be prepared optically. As already alluded to, this most likely, also has implications on the photophysics and photochemistry of the system which will in detail be scrutinized later in this work.

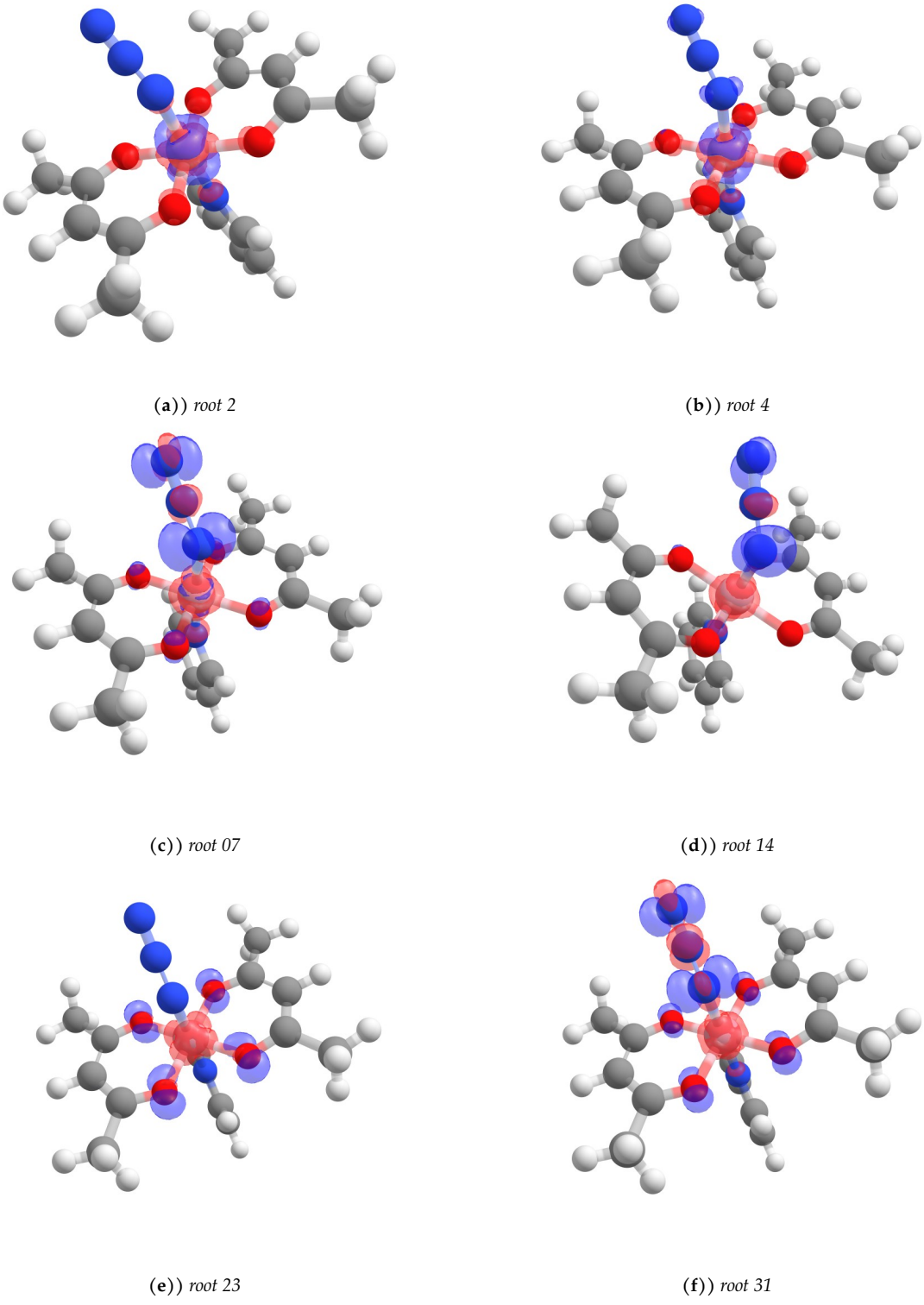

(**a**)) *root 2*

(**b**)) *root 4*

(**c**)) *root 07*

(**d**)) *root 14*

(**e**)) *root 23*

(**f**)) *root 31*

Figure 5.7.: *Difference densities attributed to selected roots as computed on the ωB97X-D/def2-TZVPP level at an iso level of 0.0065 electrons/Å^3. Shaded in red are areas that contain excessive electron density in comparison to the ground state of the molecule. Areas from which electron density is removed, in turn, are colored in blue.*

5.3. Investigations on Thermal Ground State Dynamics

When the complex *trans*-[**1**] is brought into solution, at ambient temperature soon significant spectral changes were detected both in the NMR and the FTIR spectrum confirming previous reports by Boucher and Herrington. Based on their NMR studies these authors concluded that this evolution is brought about by a stereochemical isomerization. Indeed, reports in the literature indicate that *trans*-[**1**] may also exist in its corresponding *cis* form with respect to the relative orientation of the pyridine and the azido ligand, i.e., an apical and an axial position are occupied by either of the two ligands. The latter stereoisomer was reported to form spontaneously in solution from *trans*-[**1**] establishing a thermal equilibrium between the two stereoisomers as deduced by NMR studies.[126] To further scrutinized this phenomenon and to evaluate it from a thermodynamic as well as from a kinetic viewpoint, this process was investigated in more detail by FTIR spectroscopy and the insight to these questions is presented in the following.

5.3.1. Spectral Dynamics

When the complex *trans*-[**1**] is brought into solution at ambient temperature, soon significant spectral changes can be observed both in the NMR as well as in the FTIR spectrum. This process was scrutinized in more detail in 1,2-dichloroethane (EDC) solution in order to clarify the nature of this process. Here, opposed to the stationary measurements presented in section 5.2.3, EDC was chosen as the solvent due to advantageous optical and thermal properties of this solvent for these particular investigations. It should be noted, that changing the solvent was found to have only a minor influence on the peak positions, hence solvent induced peak shifts, if at all, were barely larger than a few wavenumbers for all bands across the spectrum

Prominent spectral changes were observed in particular in the carbonyl and the azide stretching region. For visualization, selected spectra recorded at 20 °C over the course of several hours are plotted in Fig. 5.8 . Here, a gradual blueshift of the azide stretching band initially located at 2019 cm^{-1} by roughly 4 cm^{-1} is observable over time. Interestingly, this spectral evolution gives rise to an isosbestic point (indicated by an asterisk) at 2021 cm^{-1}, i.e., at this exact spectral position the optical density remains constant over time while the rest of the spectrum evolves. This is often taken as an indication of a clean interconversion between two species whose extinction coefficients match exactly at this frequency.[127] In addition, a newly emerging signal is observed in the carbonyl stretching region of the acac ligand at 1589 cm^{-1} which appears as a shoulder blueshifted with respect to the A''(ν(C=O)) peak. The latter, indeed, is also subject to a subtle frequency shift accompanied by a slight decay of the low frequency wing of the band below 1575 cm^{-1}. Here, likewise another isosbestic point (marked by *) can be identified at 1578 cm^{-1}.

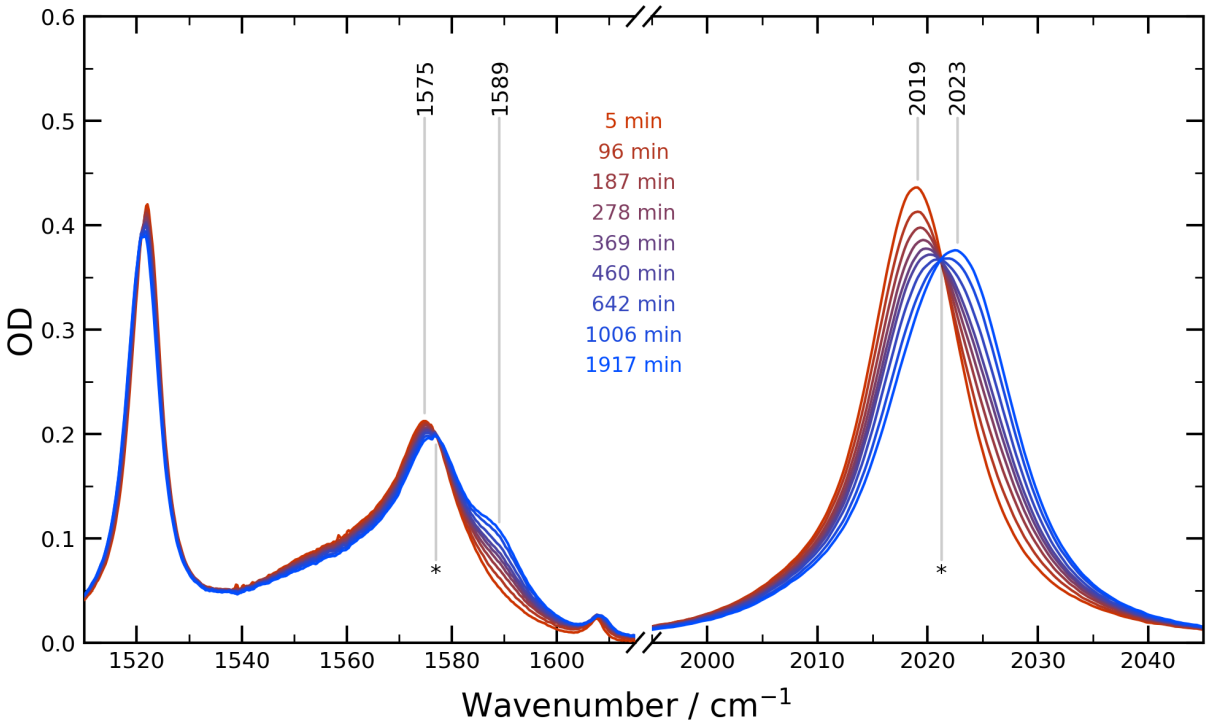

Figure 5.8.: *Temporal evolution of the spectrum of a solution of trans-*[**1**] *in dichloroethane at 20 °C. Clearly visible is the evolution of a pronounced shoulder at 1589 cm^{-1} and a clear blue shift of the azide stretching band from 2019 cm^{-1} to 2023 cm^{-1}. Isosbestic wavenumbers at 1578 cm^{-1} and 2021 cm^{-1} are marked by asterisks.*

Especially the newly emerging signal in the carbonyl stretching region of the spectrum is particularly conclusive since it indicates a symmetry breakage upon formation of the new species. Thus, the local D_{2h} symmetry or the overall C_s symmetry of the complex is lost. As pointed out in section 5.2.2, the C_s symmetry of the system, in fact, greatly simplifies its NMR spectrum and any symmetry breakage in the system should clearly manifest itself in the spectrum since the chemical equivalence of the methyl groups is no longer given. This was indeed observed before by NMR studies conducted by Boucher and Herrington.[126] Based on their findings, these authors concluded that *trans*-[**1**] is subject to stereochemical isomerization, i.e., a rearrangement of the ligand sphere that furnishes the complex in it *cis* configuration according to the following reaction

$$\textit{trans}\text{–}\mathrm{Co(acac)_2N3py} \rightleftharpoons \textit{cis}\text{–}\mathrm{Co(acac)_2N3py}. \tag{5.1}$$

In *cis*-[**1**], the azido and the pyridine ligand adopt both an apical and an axial coordination site, hence lowering the overall symmetry of the system to C_1. As a consequence neither of the four methyl groups of the acac ligands are chemically equivalent any longer. Therefore they appear as separate resonances and should therefore easily be identified in the NMR spectrum which indeed was verified on samples that were kept in solution over several hours. Owing to this symmetry breakage, the rationalization for the absence of the A′(ν(C=O)) band in the FTIR spectrum of *trans*-[**1**] due to cancellation of the dipole vectors as discussed in section 5.2.3, is no longer valid.

Hence, upon formation of *cis*-**[1]**, the in-phase combination of the carbonyl stretching modes experiences a significant gain in transition dipole moment. This should result in the emergence of a new band in this spectral range which indeed is observed experimentally and hence lends some additional credence to the interpretation put forth by Boucher and Herrington.[126] Moreover, by calculating integral ratios of signals corresponding to either of the two stereoisomers, these authors were also able to deduce equilibrium constants K_{eq} for a set of selected temperatures (c.f. Tab. 5.5). In particular, at 20 °C the equilibrium was already found to be shifted in favor of the *cis* isomer ($K_{eq}(T = 20\,°C) = 2.13$). Considering the temperature dependence of the equilibrium constant, the standard reaction free energy $\Delta G_r^{\ominus}$ given by,

$$\Delta G_r^{\ominus} = -RT \cdot \ln(K_{eq}) = \Delta H_r^{\ominus} - T \cdot \Delta S_r^{\ominus}, \tag{5.2}$$

can be determined.[91,128,129] Here, R and T refer to the universal gas constant and the absolute temperature, respectively. Besides that, $\Delta G_r^{\ominus}$ is likewise related to the standard reaction enthalpy and entropy, $\Delta H_r^{\ominus}$ and $\Delta S_r^{\ominus}$, respectively via[91,128,129]

$$\Delta G_r^{\ominus} = \Delta H_r^{\ominus} - T\Delta S_r^{\ominus}. \tag{5.3}$$

From a reevaluation of the data reported in the literature, these two thermodynamic quantities were determined as $\Delta H_r^{\ominus}$=13 kJ mol^{-1} and $\Delta S_r^{\ominus}$=50 J K^{-1} mol^{-1}, respectively. Albeit the formation of the *cis* isomer is slightly endothermic, the overall reaction is still exergonic at a temperature of 20 °C by $\Delta G_r^{\ominus} = -1.84$ kJ mol^{-1} and should therefore occur spontaneously given that the reaction barrier is not too high, which indeed is observed in the experiment. In fact, for temperatures above −16 °C, the endothermic nature of the reaction is already overcompensated by the entropic contribution, thus rendering the reaction exergonic. In turn, by proper choice of the experimental conditions, i.e., cooling below this temperature, the thermal stereochemical scrambling can in principle be suppressed.

For any time t, the respective spectrum $OD(\tilde{\nu}, t)$ is given as the weighted sum of the pure component spectra $OD_{cis}(\tilde{\nu})$ and $OD_{trans}(\tilde{\nu})$ via

$$OD(\tilde{\nu}, t) = x_{cis}(t) \cdot OD_{cis}(\tilde{\nu}) + x_{trans}(t) \cdot OD_{trans}(\tilde{\nu}), \tag{5.4}$$

where x_{cis} and x_{trans} are the respective molar fractions of *cis*-**[1]** and *trans*-**[1]**, respectively, in the mixture whose sum equals unity. Owing to the isomeric purity of the starting material, it should be noted, that at $t = 0$ the spectrum essentially is identical to the pure component spectrum of the *trans* isomer, i.e., $OD(\tilde{\nu}, t = 0) \equiv OD_{trans}(\tilde{\nu})$. However, for $t \to \infty$, i.e., at quasi-infinite delay when no further evolution of the spectrum is observable, $OD(\tilde{\nu}, t \to \infty)$ effectively reflects the spectrum of the equilibrated mixture whose equilibrium constant is given as the ratio of the two molar fractions[91,128,129]

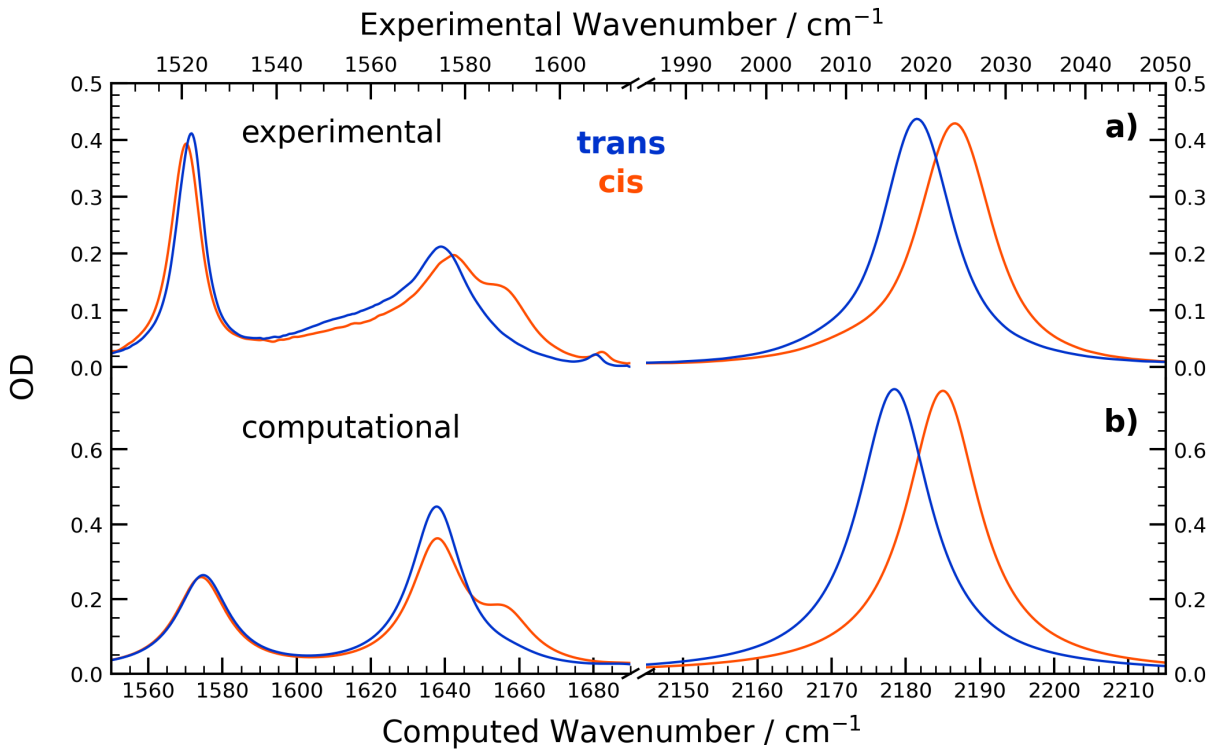

Figure 5.9.: *Experimental (top) and computational (bottom) pure component IR spectra of trans-***[1]** *and cis-***[1]** *in the spectral region of the carbonyl (acac) and the azide stretching region. Computational spectra were simulated assuming lorentzian lineshapes with full width at half maximum of 17 cm^{-1} (acac region) and 12 cm^{-1} (azide region), respectively.*

$$K_{eq} = \frac{x_{cis}(t \to \infty)}{x_{trans}(t \to \infty)} = \frac{x_{cis}(t \to \infty)}{1 - x_{cis}(t \to \infty)}. \tag{5.5}$$

Taking the above considerations into account, the pure component spectrum of the *cis* isomer can be calculated via

$$OD_{cis}(\tilde{\nu}) = \frac{1}{K_{eq}(T)} \cdot [(K_{eq}(T) + 1) \cdot OD(\tilde{\nu}, t \to \infty, T) - OD(\tilde{\nu}, t = 0)] \tag{5.6}$$

from a given series of spectra recorded at a certain temperature T.

Following this approach, the pure component spectrum of *cis*-**[1]** was calculated from the series of spectra recorded at $T = 20\,°C$ (c.f. Fig. 5.8) and is depicted in red in Fig. 5.9 (upper panel) alongside the spectrum of *trans*-**[1]** (blue trace). To corroborate the analysis, the computed vibrational spectrum of either of the two isomers is plotted in the lower panel for comparison. Indeed, an excellent agreement between the theoretical and the experimental spectra is found. Not only does the theoretical spectrum of *cis*-**[1]** correctly predict the emergence of the shoulder at 1589 cm^{-1} in the experimental spectrum (c.f. 1655 cm^{-1} in the computation) as reasoned before, but does also explain the blueshift of the azide stretching band which gives very convincing evidence to the interpretation presented here.

5.3.2. Kinetic Analysis

To assess this isomerization process from a kinetic perspective, the evolution of the optical density was tracked at selected key frequencies ($1572\,\mathrm{cm}^{-1}$, $1589\,\mathrm{cm}^{-1}$, $2017\,\mathrm{cm}^{-1}$, $2021\,\mathrm{cm}^{-1}$ and $2025\,\mathrm{cm}^{-1}$) in the spectra shown in Fig. 5.8, and the resultant kinetic traces are plotted in Fig. 5.10. It is evident, that at the isosbestic wavenumber of $2021\,\mathrm{cm}^{-1}$ essentially no change in optical density is observed, while the signals at the spectral positions of the newly emerging signals follow what appears to be a monoexponential behavior.

Thus, expressing the decay and growth kinetics according to the normalized optical density correlation function

$$C(\tilde{\nu},t) = \frac{OD(\tilde{\nu},t) - OD(\tilde{\nu},t\to\infty)}{OD(\tilde{\nu},t=0) - OD(\tilde{\nu},t\to\infty)}, \tag{5.7}$$

should result in a representation of the data that is describable by

$$C(t) = \exp\left(-\frac{t}{\tau_{eff}}\right) \tag{5.8}$$

with τ_{eff} being the effective time constant that combines the simultaneous action of both the forward and the backwards reaction. Fitting these kinetic traces and plotting in a logarithmic form as shown in Fig. 5.11, indeed results in straight lines that regardless of the exact wavenumber all share an identical time constant of (512 ± 3) min. This is well in line with the expected unimolecular nature of the *trans*-to-*cis* isomerization.

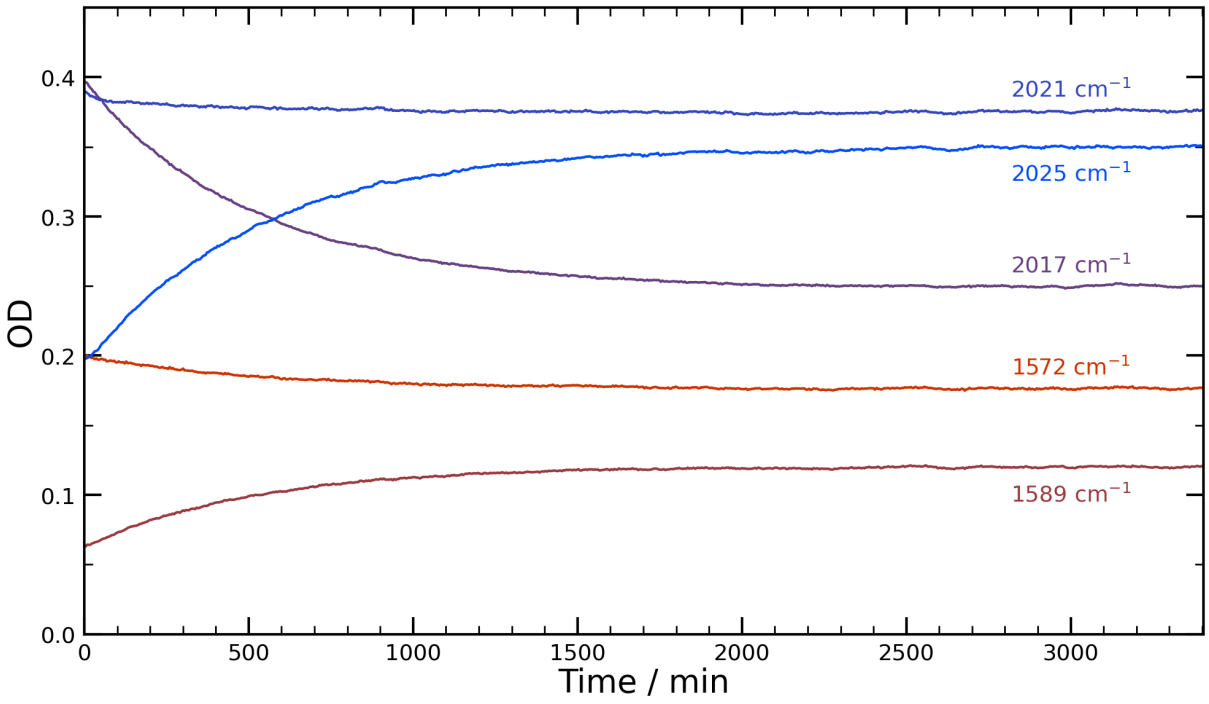

Figure 5.10.: *Kinetic traces taken from a series of FTIR spectra at selected probe frequencies at 20 °C. At 2021 cm^{-1} essentially no temporal evolution is observed, marking an isosbestic point in the series of time-dependent spectra. Clear changes, however, are seen in the carbonyl stretching region at 1589 cm^{-1}.*

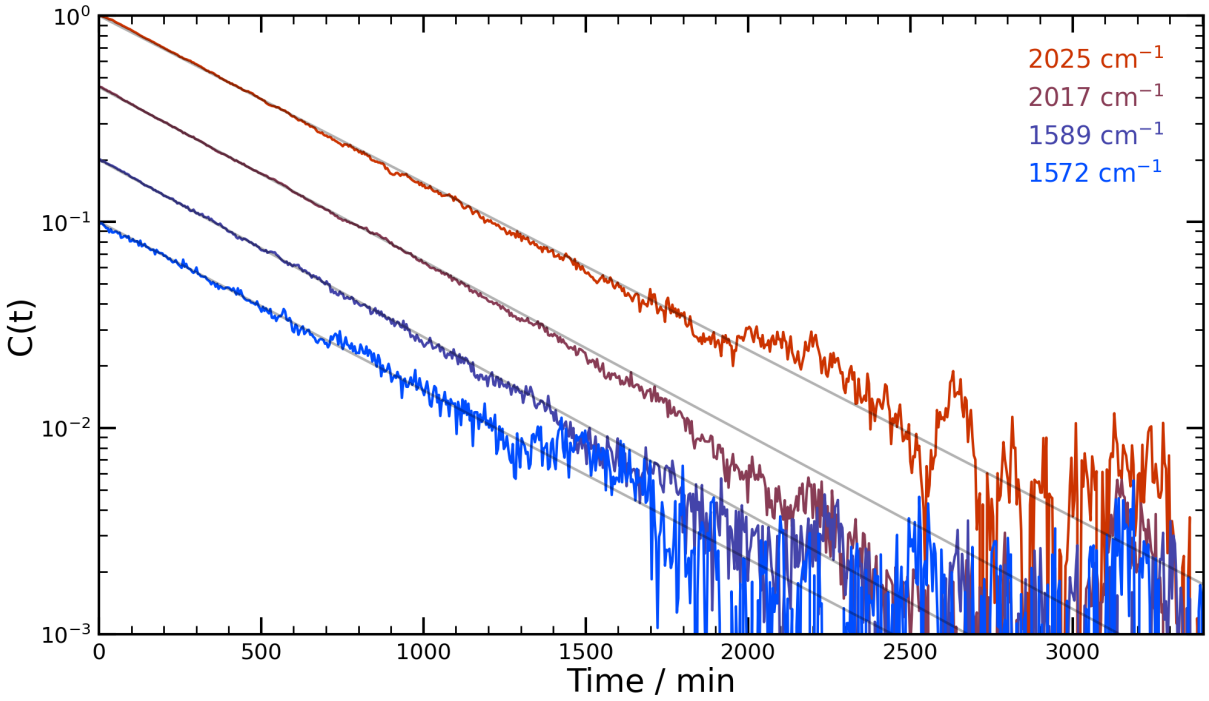

Figure 5.11.: *Evolution of the optical density correlation function $C(t)$ at 20 °C over time for selected probe frequencies. Traces are shifted vertically for clarity. For all the frequencies of interest a common effective time constant of 512 min is observed.*

It should be stressed out that the obtained time constants τ_{eff}, essentially describe the approach towards the chemical equilibrium and as such are related to the rate constants k_f and k_b of the two competing forward and backwards reactions (c.f. Eq. 5.1) via

$$\frac{1}{\tau_{eff}} = k_{eff} = k_f + k_b, \tag{5.9}$$

where the effective rate constant k_{eff} is simply the inverse of the observed effective time constant. It should be noted, that in case of a simple equilibrium between two species as in the present case, the ratio of the two involved rate constants is identical to the equilibrium constant,[91,128,129] i.e.,

$$K_{eq} = \frac{k_f}{k_b}. \tag{5.10}$$

Thus, Eq. 5.9 and Eq. 5.10 can be combined into the following system of equations

$$k_f = k_{eff} \cdot \frac{K_{eq}}{1 + K_{eq}} \tag{5.11}$$

$$k_b = \frac{k_{eff}}{1 + K_{eq}} \tag{5.12}$$

which allows for the determination of k_f and k_b given that k_{eff} and K_{eq} are known. Following this analysis, at ambient temperature (20 °C) the rate constants of the forward reaction and backward reaction were determined as $k_f = (2.21 \pm 0.02) \cdot 10^{-5}\,\mathrm{s}^{-1}$ and $k_b = (1.04 \pm 0.02) \cdot 10^{-5}\,\mathrm{s}^{-1}$.

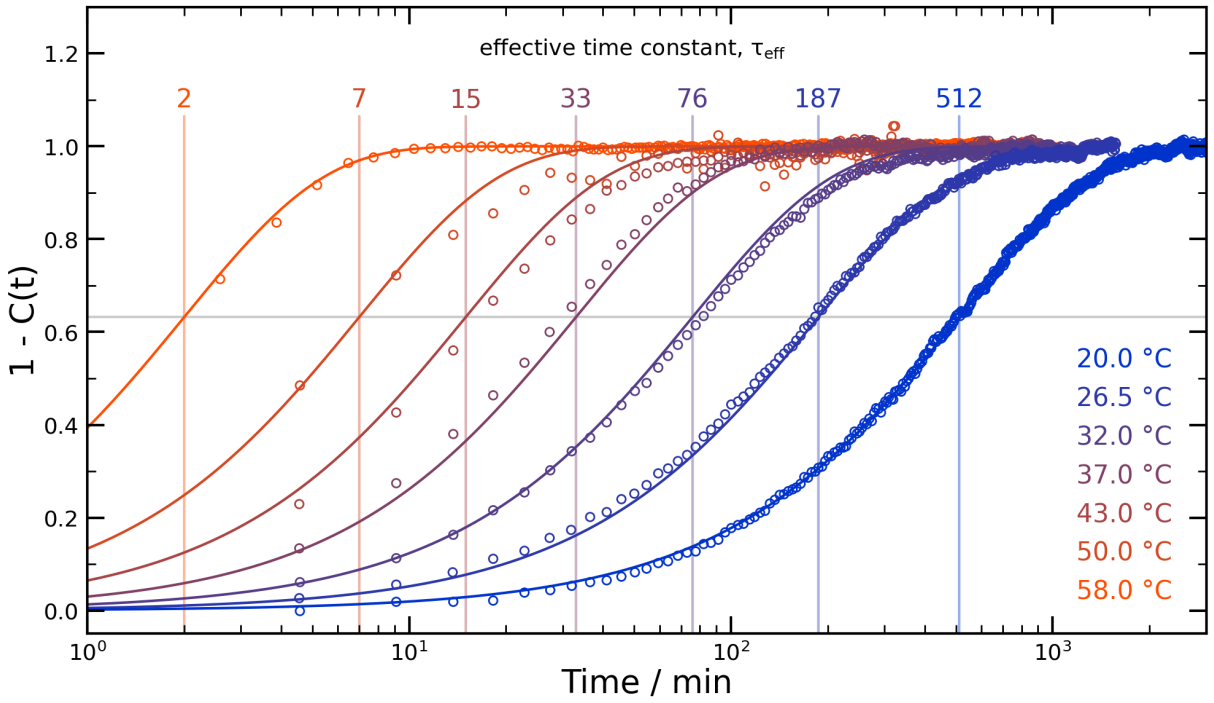

Figure 5.12.: *Kinetic build-up of cis-*[**1**] *as monitored by the evolution of the shoulder at 1589 cm^{-1}. The effective time constants (in minutes) required to reach the chemical equilibrium are denoted above the individual traces.*

To explore the temperature dependency of the reaction, studies were extended to a series of other temperatures. To this end, solutions of *trans*-[**1**] were allowed to equilibrate at temperatures of 26.5 °C, 32 °C, 37 °C, 43 °C, 50 °C and 58 °C continuously measuring the FTIR spectrum of the mixture as described before. To access the higher temperature ranges these studies were carried out in 1,2-dichloroethane instead, since measurements in dichloromethane or chloroform as employed in previous studies were not feasible owing to their low boiling points. Still, these solvents are sufficiently similar with regard to polarity and donor abilities, such that solvent effects on the literature-known equilibrium constants[126] and the overall FTIR spectrum (c.f. section 5.2.3) should be negligible.

Heating of the sample was ensured using a home-built temperature controlled socket into which the cell containing the freshly prepared solution was placed. The evolution of the signal at the shoulder emerging at 1589 cm^{-1} for the temperatures considered here is plotted in Fig. 5.12 in terms of the correlation function complement, 1 - $C(t,T)$, to emphasize the build-up due to formation of *cis*-[**1**] in the solution. Note, that the data are plotted on a logarithmic abscissa and the effective time constants, corresponding to the time at which the signals have grown to 63 % $(1 - e^{-1})$ of their maximum values are marked by vertical lines. In all cases the data can smoothly be fitted by monoexponential functions, shown as solid lined. Obviously, over the temperature range considered here of merely 40 °C a dramatic speed up of the observed process from 512 min up to 2 min and thus by several orders of magnitude is observed. Taking into account literature-known equilibrium constants, the rate constants k_f and k_b were calculated

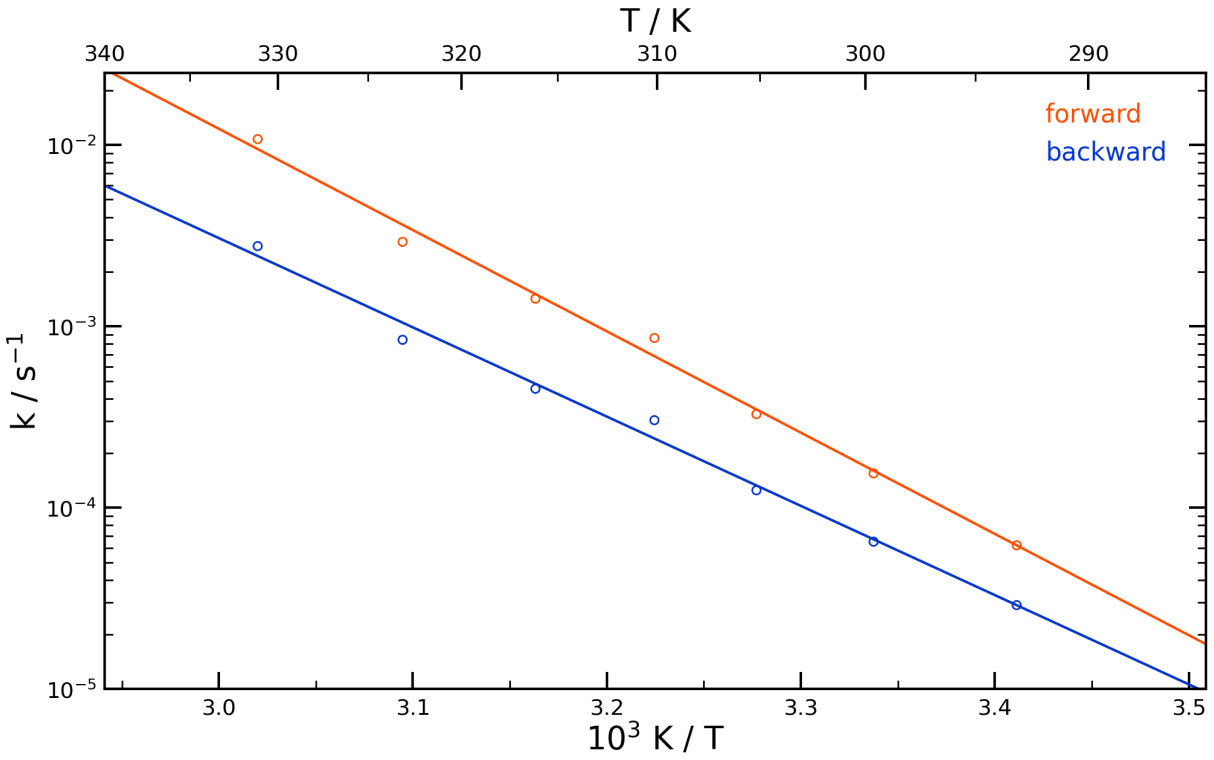

Figure 5.13.: *Arrhenius plot of rate constants of forward and backward reaction for the interconversion of trans-[**1**] to cis-[**1**]. The data appear to follow a well-behaved linear trend when plotted in a semi-logarithmic fashion. The activation energies of the forward and backward reaction can be estimated from the slope of a regression line and amount to 107 kJ mol^{-1} and 94 kJ mol^{-1}, respectively.*

according to Eq. 5.11 and Eq. 5.12 for all temperatures from the experimentally determined effective time constants and are compiled in Tab. 5.5.

The knowledge of the temperature dependency of the reaction rate constant, k, in turn, allows for an estimation of the energetic reaction barrier, E_A, based on Arrhenius' equation

$$k = A \cdot \exp\left(-\frac{E_A}{RT}\right), \tag{5.13}$$

where A is a constant preexponential factor,[91,128,129] specific to either of the two involved reactions. Plotting of the data compiled in Tab. 5.5 in a linearized fashion ($\ln(k)$ vs. $1/T$) shown in Fig. 5.13 indeed results in straight lines whose slope is directly proportional to the activation energy as is evident from Eq. 5.13. Hence, the reaction barriers are determined to amount to $E_{a,f}$ =(122 ± 8) kJ mol^{-1} and $E_{a,b}$ = (109 ± 8) kJ mol^{-1}, for the forward and the backwards reaction, respectively.

Table 5.5.: *Temperature dependence of the chemical equilibrium and rate constants of forward and backwards reaction of trans-[**1**] to cis-[**1**] interconversion.*

T / °C	K_{eq}	τ_{eff} / min	k_f / s^{-1}	k_b / s^{-1}
20.0	2.13	512.0 ± 0.6	$(6.24 \pm 0.01) \cdot 10^{-5}$	$(2.92 \pm 0.01) \cdot 10^{-5}$
26.5	2.39	187.0 ± 0.6	$(1.55 \pm 0.01) \cdot 10^{-4}$	$(6.50 \pm 0.02) \cdot 10^{-5}$
32.0	2.62	76.0 ± 0.4	$(3.28 \pm 0.02) \cdot 10^{-4}$	$(1.25 \pm 0.01) \cdot 10^{-4}$
37.0	2.84	33.0 ± 0.2	$(8.68 \pm 0.05) \cdot 10^{-4}$	$(3.05 \pm 0.02) \cdot 10^{-4}$
43.0	3.12	15.0 ± 0.2	$(1.42 \pm 0.02) \cdot 10^{-3}$	$(4.55 \pm 0.05) \cdot 10^{-4}$
50.0	3.47	7.0 ± 0.4	$(2.93 \pm 0.01) \cdot 10^{-3}$	$(8.47 \pm 0.04) \cdot 10^{-4}$
58.0	3.89	2.0 ± 0.1	$(1.08 \pm 0.01) \cdot 10^{-2}$	$(2.78 \pm 0.02) \cdot 10^{-3}$

5.3.3. Theoretical Investigation

Stereochemical isomerization of transition metal complexes is a phenomenon that is well-known in the literature and several mechanistically distinct pathways have been suggested. In general, either of the pathways can be distinguished by the fact whether the isomerization process entails a bond rupture event. In the present case of an octahedral complex, in principle two different scenarios are conceivable which are schematically sketched in Fig. 5.14.

One of the mechanisms that occurs without any bond breakage is known as Bailar twist mechanism.[130–132] Most conveniently, this mechanism can be understood by plotting the complex viewed along one of the C_3 axes of the idealized coordination octahedron. Hence, the ligands in the front and in the back of the plane span two triangles that are rotated relative to each other by 120°, hence the ligands are in a staggered conformation. An isomerization might potentially then occur via the rotation of one of the two faces about the C_3 axis. Consequently the complex has to pass through an eclipsed geometry in which the ligand atoms form the corners of a trigonal prism. This conformer, most likely is maximal in energy along the reaction coordinate, due to the unfavored steric repulsion, and hence constitutes the transition state of the isomerization. In the present case, accordingly the *trans*-to-*cis* isomerization of **[1]** can be regarded as the conversion of the anti into the gauche conformer in which the angle between the nitrogen atoms of the pyridine and the azido ligands when viewed along the axis of rotation amounts to roughly 60°.

Alternatively, isomerization can likewise occur via a stepwise mechanism involving intermediate dissociation of a ligand and has been reported for numerous systems.[133,134] Thus, the racemization is initialized by a bond breakage event. In fact, especially for electron rich octahedral complexes, this dissociation step is frequently observed in ligand substitution reactions which furnishes a pentacoordinated complex of square pyramidal geometry.[123,135,136] Given, that the lifetime of this intermediate is sufficiently high, it may undergo a molecular motion that scrambles the apical and and equatorial ligand via a process that can be regarded as an inverse Berry pseudorotation (c.f. Fig. 5.14). Opposed to the regular Berry pseudorotation mechanism as most prominently fea-

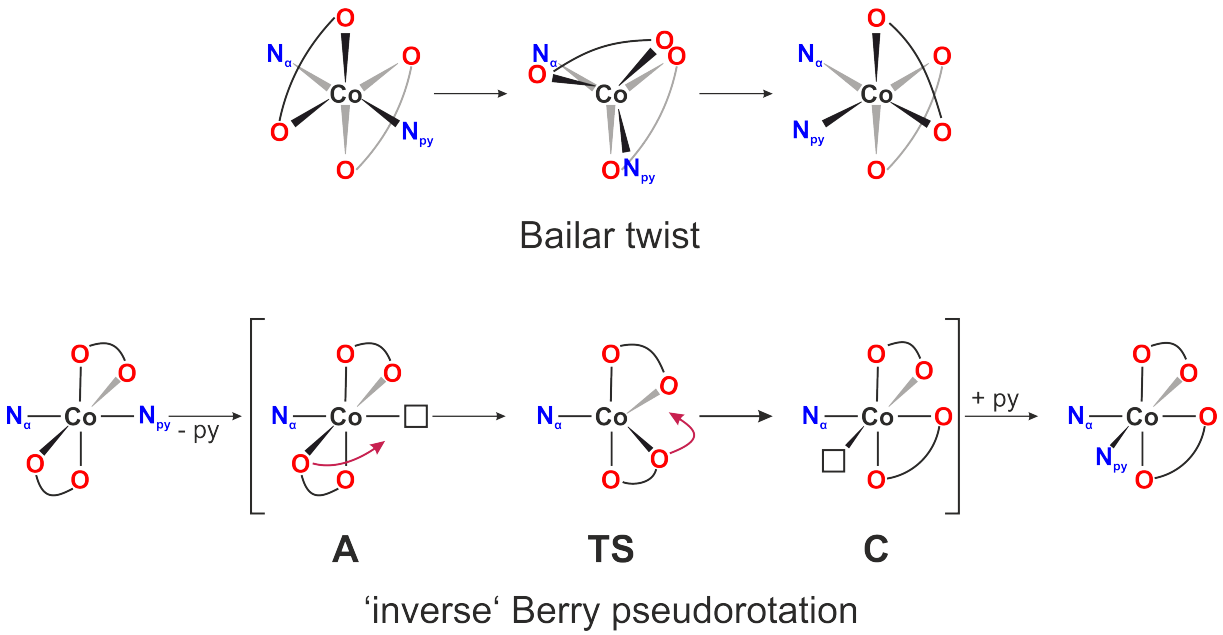

Figure 5.14.: *Possible reaction mechanisms for the racemization of trans-*[**1**]*. Whereas the Bailar twist mechanism (top) does not involve a bond rupture event, the sequential pathway (bottom) involves dissociation of pyridine under formation of a square-pyramidal intermediate that is subject to stereochemical scrambling via an 'inverse' Berry pseudorotation. Religation of pyridine, ultimately furnishes the cis isomer. According to theory, only the sequential mechanism (bottom) is feasible, most likely owing to highly unfavored steric repulsions between the ligands in the trigonal prismatic transition state of the Bailar twist mechanism.*

tured in the archetypical phosphorus pentaflouride (PF_5) compound,[137] here instead the transition state has approximate trigonal bipyramidal geometry.[138] Following the religation of the ligand to this highly Lewis acidic intermediate, thus the stereochemisty of the complex is effectively changed from *trans* to *cis*. In case of *trans*-[**1**] this mechanism can be realized via different channels. However, in this case, only dissociation of the pyridine ligand appears reasonable owing to insufficient stabilization of the highly polar intermediates that would arise from the dissociation of the azide ligand or from partial chelate opening, respectively, by the apolar solvent used in the investigations presented here.

To explore the energetic feasibility of either of the two pathways considered here, DFT calculations on the PW1B95/def2-TZVP level of theory were carried out. In a first step, the identification of a potential transition state of the Bailar twist mechanism was addressed. As was revealed in silico, no true saddle point could be identified, when starting from a trigonal prismatic transition state structure, that was created by simple rotation of one of the trigonal faces of the coordination octahedron by 60° as discussed above. Instead, in the calculation successively the pyridine is expelled from the complex resulting in a molecular structure in which it is only loosely bound via dispersive interaction. As it appears, in the eclipsed conformation the steric repulsions between the ligands are too high and the required transition state can therefore not be realized.

Thus, instead, the sequential mechanism involving pyridine dissociation was investigated. In fact, on the potential energy surface two distinct local minimum structures **A** and **C** were identified, in which the azide ligand adopts either the axial or a basal

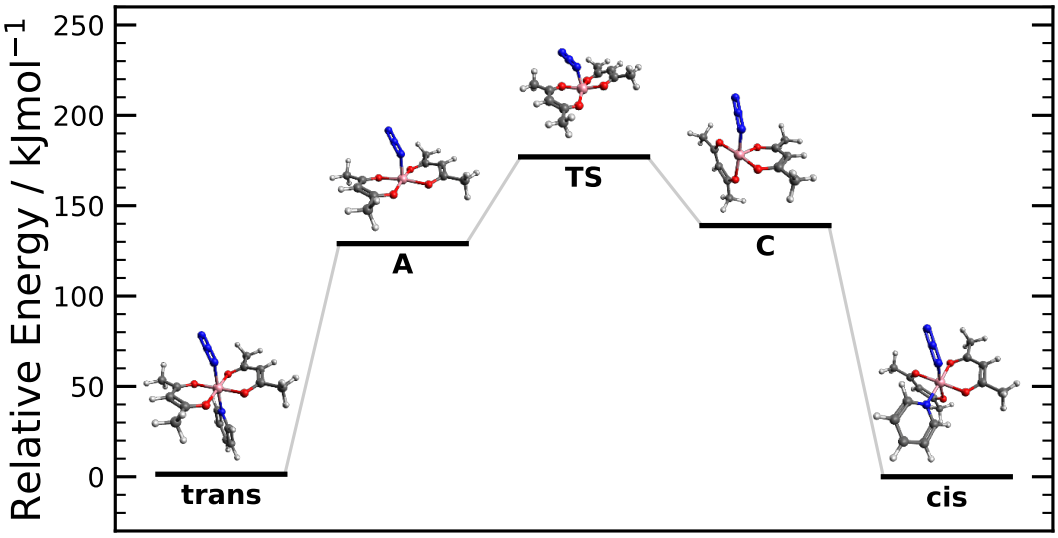

Figure 5.15.: *Simplified energy profile of the sequential isomerization mechanism of* $[Co(acac)_2(N_3)(py)]$. *Energies of intermediates are given relative to trans*$-[Co(acac)_2(N_3)(py)]$.

coordination site that are depicted in Fig. 5.15. It is obvious, that either of the two structures emerge without any major geometric distortions from the corresponding molecular structure of *trans*-**[1]** and *cis*-**[1]** simply by detachment of the pyridine ligand and the energy differences between them can be taken as estimates for the pyridine dissociation energies. Thus, in the former case, according to theory dissociation of pyridine from *trans*-**[1]** is uphill in energy by 129 kJ mol^{-1} whereas the religation of pyridine to structure **C** releases an energy of 139 kJ mol^{-1} as sketched in Fig. 5.15.

To identify the transition state interconnecting the two structures along the reaction coordinate, a transition state search was carried out in silico. Indeed, a molecular structure **TS** could be identified that exhibits distorted trigonal bipyramidal geometry as shown in Fig. 5.15 that emerges from **A** by rotation of one acac ligand out of the plane spanned by the oxygen atoms. This distortion starting from **A** requires additional 48 kJ mol^{-1}, or in total 177 kJ mol^{-1}, starting from *trans*-**[1]**. Remarkably, the theoretically determined pyridine dissociation energy of *trans*-**[1]** is very close to the experimentally determined activation energy for the overall *trans*-to-*cis* isomerization. Considering that theoretically calculated reaction energy barriers are often subject to high uncertainties,[139,140] even the total activation energy of 177 kJ mol^{-1} is still in satisfactory agreement with the experiment ($\sim$30 %).

Thus, taking the combined body of theoretical and experimental results into account, it is reasonable to conclude, that the observed isomerization of *trans*-**[1]** indeed occurs via a sequential mechanism that involves pyridine dissociation as its initial step. The resultant pentacoordinate intermediate is sufficiently long-lived to isomerize via

an 'inverse' Berry pseudorotation followed by religation of the ligand that concludes the overall reaction sequence and furnishes the respective *cis* isomer, *cis*-**[1]**.

5.4. Time-Resolved Spectroscopy

Having fully scrutinized the thermal behavior of *trans*-**[1]** in solution, with this knowledge subsequently femtosecond UV/mIR spectroscopic investigations were conducted on this compound to explore the ultrafast primary photochemical and photophysical processes brought about by excitation by ultraviolet light.

5.4.1. UV-Pump mIR-Probe Spectroscopy

UV-pump mid-infrared-probe spectroscopic measurements were conducted using the experimental setup and the procedure previously described(see section 4.2). The UV pump light at a wavelength of 266 nm was generated via third-harmonic generation of the 800 nm fundamental of the Ti:sapphire laser. Additionally, to suppress the beforementioned stereochemical scrambling of the compound, it was critical to control the temperature of the solution. This was achieved using a cooling bath (ice/sodium chloride mixture) in which the sample reservoir was kept at −15 °C throughout the course of the measurement.

Time-resolved spectra were recorded in the spectral ranges of the carbonyl stretching modes of the acac ligand (1490 cm^{-1} to 1620 cm^{-1}) and the antisymmetric azide stretch (1940 cm^{-1} to 2070 cm^{-1}), respectively. In the former case, the spectra were merged together from two different sets of measurements because of limitations with respect to the detectable wavelength range of the MCT detector and the spectral bandwidth of the probe pulse. Time-resolved spectra were collected for delays between the UV pump and the mid-infrared detection pulse ranging from −10 ps to 150 ps. Extending the delay range to even later times proved to be unnecessary, because all of the relevant ultrafast processes of the system occur within this observed time window.

Pump-probe spectra for selected delays are visualized in Fig. 5.16 (panel a) and b)). As can be seen, the spectra are governed by the presence of negative, ground state bleaching (GSB) signals occurring at the spectral positions corresponding to the characteristic absorptions of *trans*-**[1]** in the stationary FTIR spectrum (plotted in an inverted fashion in gray). This can readily be rationalized based on the considerations presented in section 3.2, i.e., the UV pump pulse transfers a portion of the molecules to excited vibronic states that feature a different spectroscopic fingerprint. Hence, the sample gains transmission at these frequencies manifesting itself by the occurrence of negative signals. Likewise, frequency redshifted induced absorptions (IA) initially peaking at 1517 cm^{-1}, 1538 cm^{-1} and 1975 cm^{-1} and corresponding to either of the GSB signals can be identified indicative of decreased transmittance of the sample resulting from the UV

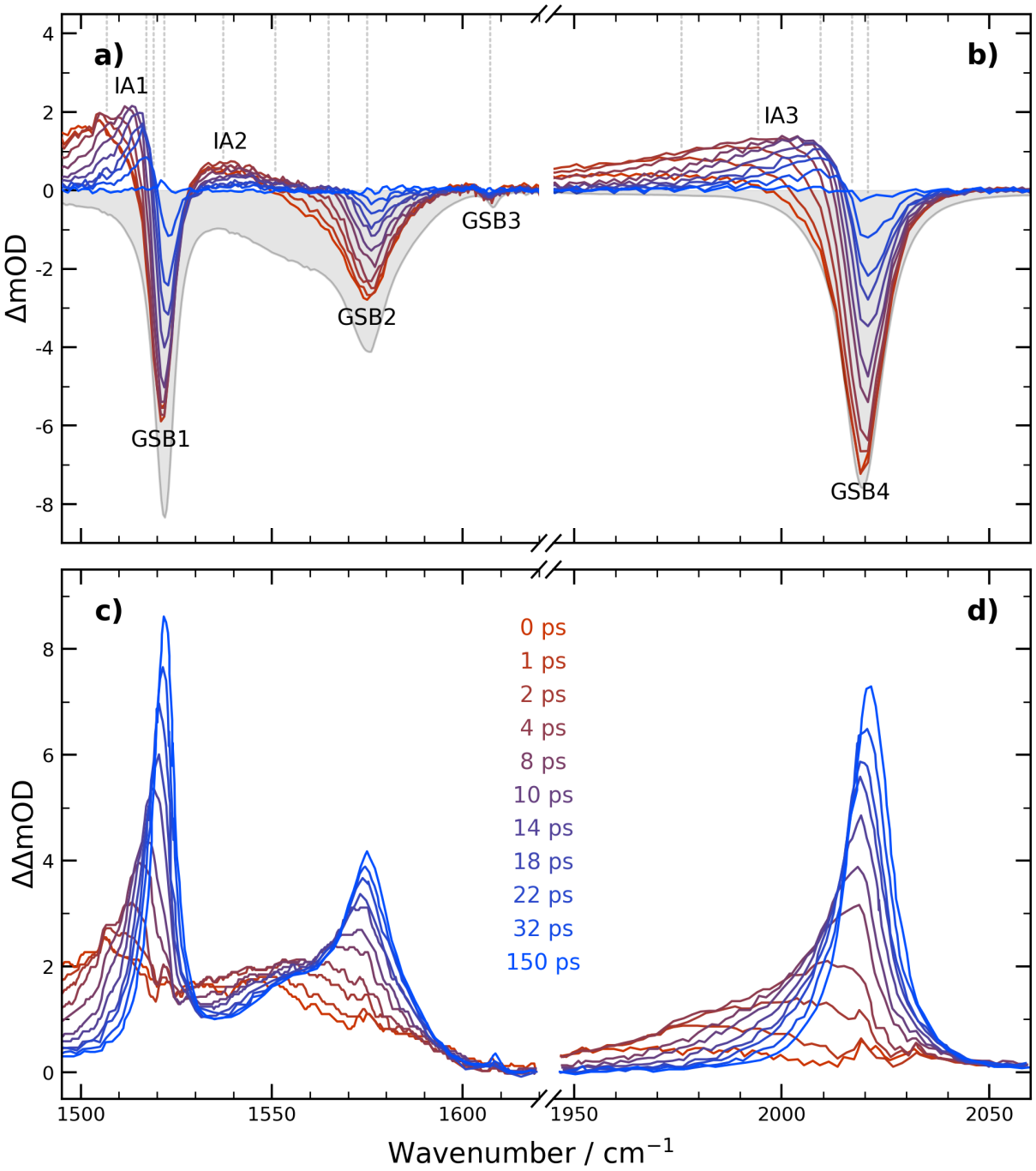

Figure 5.16.: *Time-resolved UV-pump mid-infrared-probe spectra of trans-[**1**] recorded in the carbonyl (a) and the azide (b) stretching spectral regions for selected delays between the pump and the probe pulse. Purely absorptive product spectra calculated by adding the properly scaled inverted FTIR spectrum to the time-resolved spectra are depicted in (c) and (d), respectively. Frequencies, at which kinetic traces were extracted, are indicated by dotted vertical lines in a) and b).*

excitation. Owing to the altered electronic structure, which usually entails the population of antibonding molecular orbitals (MOs), hence the excitation of the respective molecular normal modes requires less energy due to softening of the bonds, thereby giving rise to several redshifted IA bands in the spectrum (c.f. IA1, IA2, IA3 in Fig. 5.16, respectively).

Especially, the band of the induced absorption in the azide stretching region (IA3) exhibits a very peculiar spectro-temporal behavior. Thus, at early delays it features

an immense spectral bandwidth of roughly 50 cm^{-1}, but is observed to rapidly shift to higher frequencies within only a few picoseconds. Instead, the temporal evolution of IA1 and IA2, in turn, can be qualitatively described as follows: at early delays, the induced absorption is very broad and undefined in terms of its spectral profile. Only as the delay between the pump and the probe pulse is increased the signals first reshape, i.e., narrow down, to ultimately vanish completely. Still, in general, as the induced absorption peaks vanish, similarly the GSB signals recover, i.e., their spectral amplitude decreases, indicating a repopulation of the ground state at the expense of the intermediate excited state. However, it is worth mentioning that the evolution of the signals attributed to the acac CO stretching mode (IA2 and GSB2) is particularly complex, since the induced absorption is apparently partially obscured by the ground-state bleaching signal GSB1 due to the broad nature of the latter.

To obtain further insights into the spectro-temporal evolution of the signal, kinetic traces were extracted at distinct probe frequencies (indicated by vertical dotted gray lines in Fig. 5.16 panel a) and b)) and are compiled in Fig. 5.17. Note, that for the sake of clarity, data were scaled to a comparable level and shifted vertically. Experimental data are represented by circles alongside fits to the respective traces. Phenomenologically, kinetic traces were fitted by multiexponential functions according to

$$S(t) = A_0 + \sum_{i=1}^{2} A_i \cdot \exp\left(-\frac{t}{\tau_i}\right) = A_0 + A_1 \cdot \exp\left(-\frac{t}{\tau_1}\right) + A_2 \cdot \exp\left(-\frac{t}{\tau_2}\right) \tag{5.14}$$

or in an alternative representation as

$$S(t) = A_0 + A_1 \cdot \exp\left(-\frac{t}{\tau_1}\right) - (A_1 + \delta A) \cdot \exp\left(-\frac{t}{\tau_1 + \delta t}\right) \tag{5.15}$$

with $\delta A = -(A_1 + A_2)$ and $\delta\tau = \tau_2 - \tau_1$. Here, τ_i and A_i refer to the time constant and the amplitude of the *i*-th exponential component.

Still, in some cases, a systematic deviation from this kinetic behavior was observed and hence, instead a mixed Gaussian/exponential function of the form

$$S(t) = A_0 + A_1 \cdot \exp\left(-\frac{t^2}{\tau_1^2}\right) + A_2 \cdot \exp\left(-\frac{t}{\tau_2}\right) \tag{5.16}$$

was better suited for a phenomenological description of the data and was therefore employed for fitting.

The results of the fits to the experimental data are summarized in Tab. 5.6. A close inspection reveals, that the kinetics are apparently governed by three different time constants clustering around (15 ± 5) ps, (5 ± 2) ps and (1.5 ± 0.2) ps, respectively. Interestingly, all GSB signals, that are essentially governed by bleaching of the sample, entail the longest time constant in the 15 ps range. Conversely, only when probing the low frequency tails of the IA bands, the shortest time constant in the 1.5 ps range mani-

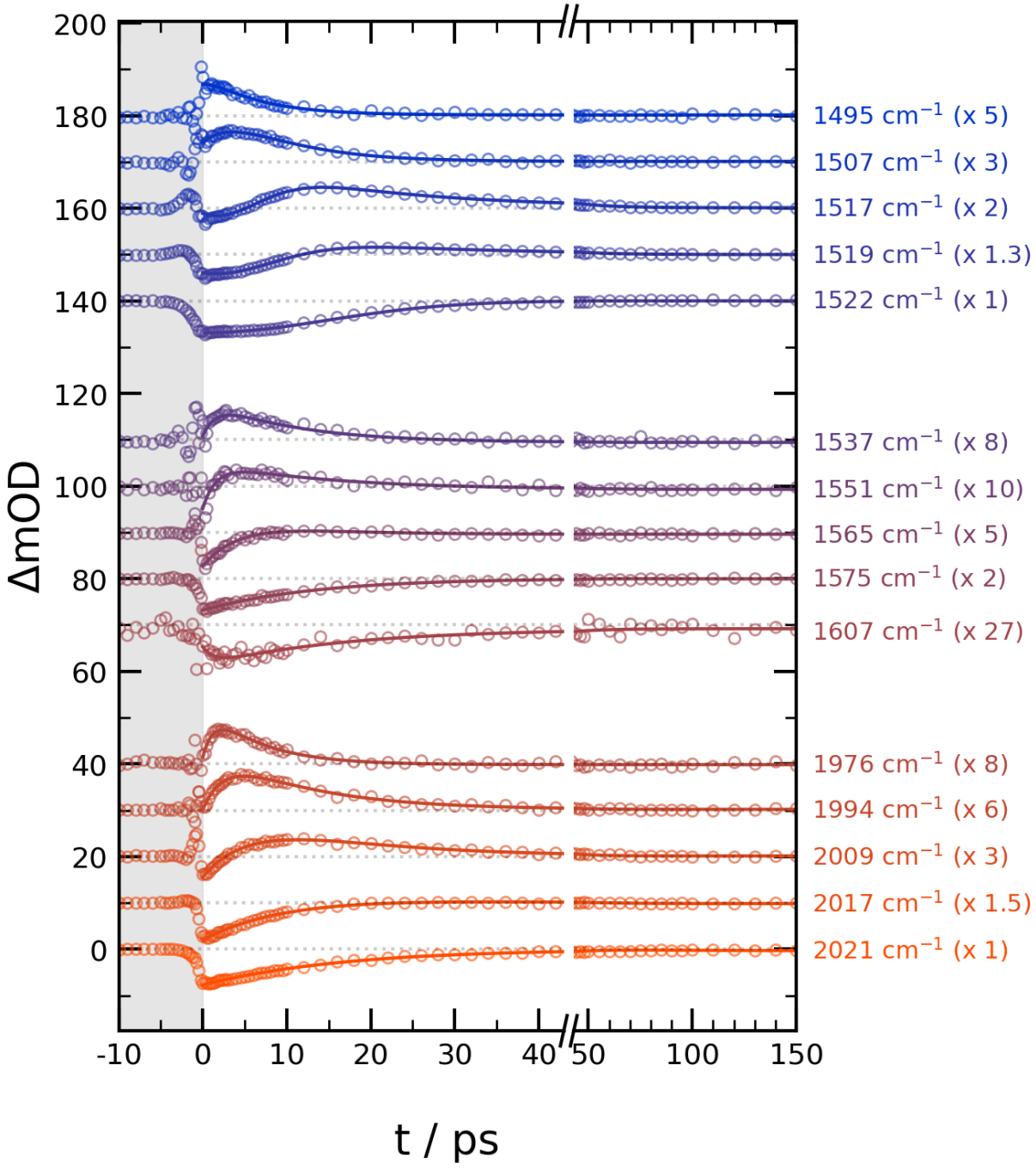

Figure 5.17.: *Kinetic traces at selected probe frequencies as extracted from UV-pump mid-infrared-probe spectra of trans−[Co(acac)2(N3)(py)]. For clarity, traces were shifted and scaled for visualization purposes. Experimental data are represented as circles alongside the multi-exponential fits to the data (solid curves).*

fests itself in the temporal evolution of the signal. Yet, in cases entailing an intermediate change in the sign of the signal, i.e., a GSB evolving into an IA signal or vice versa, the kinetic traces at the spectral position of the respective signals contain the intermediate time constant in the 5 ps range. Still, owing to pronounced spectral shifts and the overlapping nature of many of the signals, a more detailed discussion going beyond this qualitative description is in general prohibitive.

To explore the evolution of the signals unaffected by the GSB signals, so-called purely absorptive product spectra can be deduced by adding the properly scaled and – if nec-

Table 5.6.: *Parameters derived by multi-exponential/Gaussian-exponential fitting of selected kinetic traces from the UV-pump mid-infrared-probe spectra of trans−[Co(acac)2(N3)(py)]. Time constants were found to cluster around three distinct values (1.5 ps, 5 ps and 15 ps).*

$\tilde{\nu}_{probe}$ / cm^{-1}	A_0	A_1 / 10^n (n)	τ_1 / ps	A_2	τ_2 / ps	δA	$\delta\tau$ / 10^{-n} ps (n)
2021	–0.35	–2.684 (4)	23.5	—	—	7.371	2.92 (3)
2019	–0.11	–1.758 (4)	13.3	—	—	5.243	2.48 (3)
2009	0.04	–8.027 (0)	6.27	6.495	11.8	—	—
1994	0.03	–2.494 (0)	2.60	2.478	10.8	—	—
1976	–0.02	–1.546 (0)	1.31	1.740	6.24	—	—
1607	–0.03	–0.295 (0)	16.7	0.150	1.35	—	—
1575	–0.02	–5.569 (3)	17.4	—	—	3.380	3.12 (3)
1565	–0.08	–4.546 (3)	5.93	—	—	1.371	1.55 (3)
1551	–0.07	–1.009 (0)	1.64	0.597	14.2	—	—
1537	–0.07	–1.009 (0)	1.58	1.181	10.3	—	—
1522*)	0.00	–6.9 (0)	21	—	—	—	—
1519*)	0.00	–7.0 (0)	11	4.0	20	—	—
1517*)	0.05	–6.3 (0)	8.4	5.7	18	—	—
1507	0.04	–6.748 (0)	3.90	8.058	6.95	—	—
1495	0.03	–0.5460 (0)	1.58	1.856	6.16	—	—

*) Kinetic traces fitted by (multi)exponential/Gaussian function.

essary convoluted – stationary FTIR spectrum (indicated in gray in Fig. 5.16) to the time-resolved spectra that essentially represent the spectrum of the transient absorbing species[20,23,113] and the resultant spectra of such an analysis are visualized in Fig. 5.16 (panel c) and d)). Clearly, the set of initially three IA bands ultimately evolves into a spectrum that is essentially identical to the stationary FTIR spectrum brought about by continuous frequency blueshifting, band narrowing and an overall steady increase of the band integrals. This gives a clear suggestion that the complex ultimately returns to its initial state unaltered by the initial UV excitation and without the formation of significant amounts of photo products, at least upon excitation at this specific pump wavelength and within the signal-to-noise ratio achievable in this experiment.

As discussed in section 3.2 the spectral behavior observed here, is typical for a systems that disposes of the energy brought into the molecule by the UV pump pulse by energy redistribution onto its vibrational modes or through direct coupling to the solvent.[141] Thus, as it seems, after excitation *trans*-**[1]** returns on an ultrafast timescale back to the ground state energy surface dressed with a large amount of excess energy stored in its vibrational modes and is therefore referred to as vibrationally 'hot'. This way, a large number of several highly excited, vibrational states are accessible which can be seen from the very broad nature of the induced absorptions. Often following subsequent vibrational energy relaxation (VER) transfers the system back to its ground state.[141]

A thorough quantitative analysis of the VER dynamics, however, requires precise knowledge about the intramolecular anharmonic coupling constants of the individual

vibrational modes under consideration, but can in principle still be carried out on a numerical level.[142] Such an analysis was successfully applied in the past to an azido (II) cobalt complex in our workgroup based on theoretically derived ab initio anharmonic coupling constants.[106] Albeit, this analysis is usually strongly limited in its applicability to systems with only one vibrational mode of interest, since the computational costs rapidly exceed an affordable level and therefore become unfeasible for more complex systems. Instead, in such cases a frequently applied approach to extract quantitative information about the underlying VER processes from the spectro-temporal evolution of the spectra entails monitoring the spectral position of the IA peak maxima $\tilde{\nu}_{max}$ over time.[143] For this purpose, the IA signals of interest observable here in the purely absorptive product spectra were approximated by fourth order polynomials within a certain range around the peak maximum (approximately 20 cm^{-1}). By determination of the roots of its first derivative a reliable quantity can be extracted that is much less sensitive to the experimental noise and allows for extraction of time constants describing the underlying kinetics of the spectral shifting and thus the vibrational cooling process.

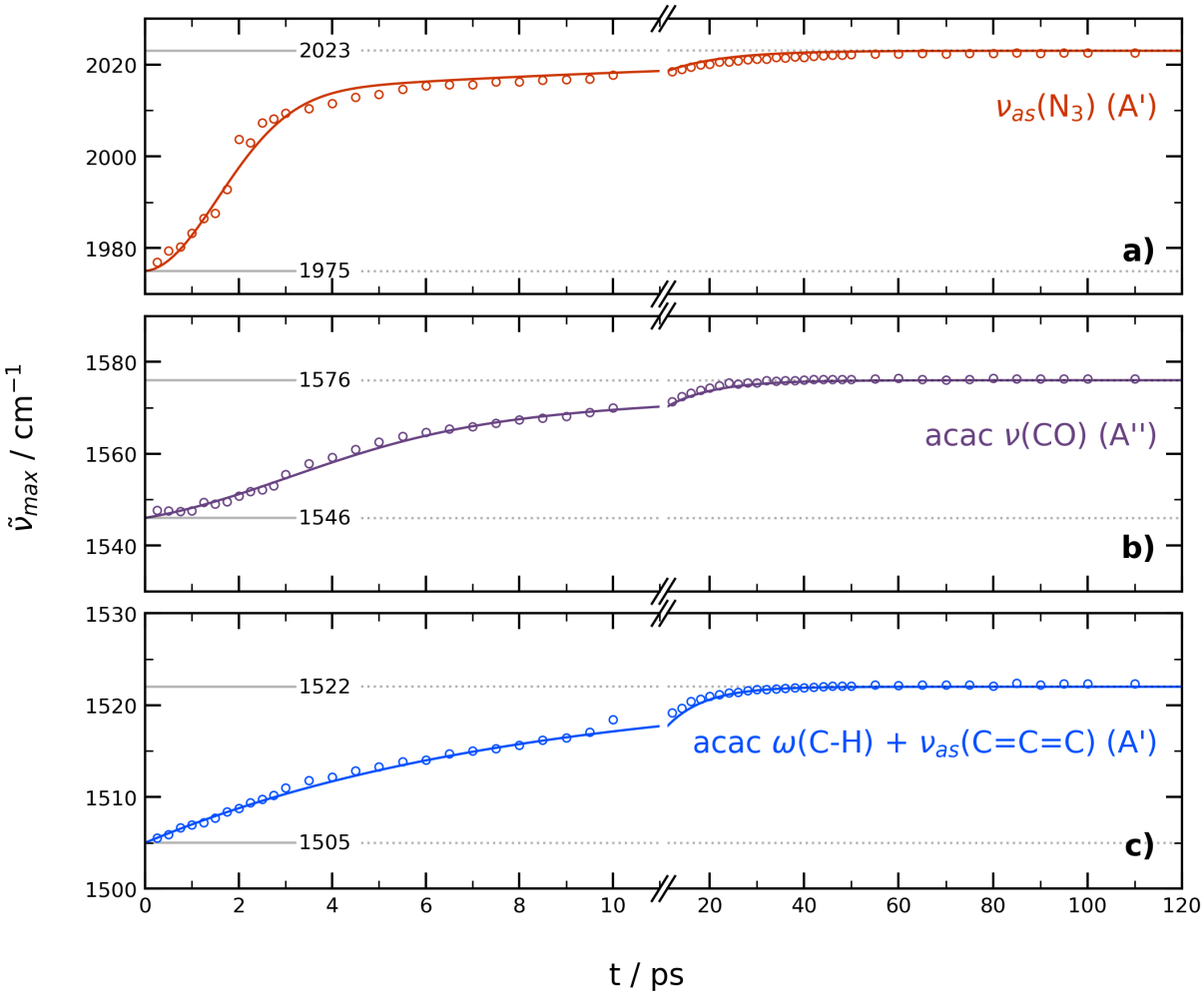

Figure 5.18.: *Peak frequencies of the induced absorption bands in the UV-pump mIR-probe spectra of trans−[Co(acac)2(N3)(py)] as observed in the carbonyl and azide stretching regions as a function of pump-probe delay. Data were extracted from the series of purely absorptive product spectra and were fitted to single exponential or Gaussian exponential kinetics, respectively.*

Table 5.7.: *Kinetic parameters derived from fitting the temporal dependency of the position of the peak maximum of the induced absorption bands in the UV-pump mIR-probe spectra of trans−[Co(acac)2(N3)(py)] by single exponential or Gaussian exponential functions.*

signal	f	τ_1 / ps	τ_2 / ps	$\langle\tau\rangle$
IA1	0.00	—	8	8.0
IA2	0.43	4.8	10	7.5
IA3	0.77	2.2	12	4.3

Hence, plots of $\tilde{\nu}_{max}$ as a function of time for all three of the observed IA bands are depicted in Fig. 5.18. It is apparent, that the majority of the observable spectral shifting occurs and is finished within the first 20 ps indicating that all the energy dumped into the system by the UV pump pulse is almost quantitatively transferred to the solvent after this short period of time.

For a more quantitative evaluation, the temporal dependence was fitted by a phenomenological function of the form

$$\frac{\tilde{\nu}(t)-\tilde{\nu}(\infty)}{\tilde{\nu}(0)-\tilde{\nu}(\infty)} = f\cdot\exp\left(-\frac{t^2}{\tau_1^2}\right)+(1-f)\cdot\exp\left(-\frac{t}{\tau_2}\right) \tag{5.17}$$

containing a Gaussian and a single-exponential component, each contributing a fraction of f and $(1-f)$ to the overall dynamic, respectively. Here, $\tilde{\nu}$(t), $\tilde{\nu}(\infty)$ and $\tilde{\nu}(0)$ represent the peak frequencies at a given time t, at a quasi-infinite delay, and at t = 0 ps, respectively, and τ_1 and τ_2 the underlying time constants.

Whereas the peak shift of IA1 was sufficiently well described by a pure exponential, an induction period at early delays required IA2 and IA3 to be fitted containing a Gaussian component with an overall weight of 23 % and 77 %, respectively. The parameters extracted from fits to the experimental data according to Eq. 5.17 are compiled in Tab. 5.7. In addition, a mean vibrational relaxation time constant defined by

$$\langle\tau\rangle = \int_0^\infty \frac{\tilde{\nu}(t)-\tilde{\nu}(\infty)}{\tilde{\nu}(0)-\tilde{\nu}(\infty)}\,dt \tag{5.18}$$

can be determined and is likewise listed in Tab. 5.7.

Strikingly, it was found that with a mean vibrational time constant of τ = 4.3 ps (extracted from IA3), the azide vibration appears to dissipate its energy roughly twice as fast as compared with the vibrational modes located on the acac ligands, ν(C=O) (7.5 ps, IA2) and ω(C−H) + ν_{as}(C=C=C) (8.0 ps, IA1), respectively. At first glance, it thus may appear as if the relaxation and the dissipation of energy occurs in a fashion that is dependent on the exact nature of the underlying involved vibrational motion, i.e., in a mode specific manner. A final conclusion solely based on these studies, however, is not possible. Therefore, to corroborate or refute this hypothesis, further time-resolved studies probing the response of the sample in the near-UV-to-visible (nUV-to-Vis) range following UV excitation were conducted and are presented in the following section.

5.4.2. UV-Pump nUV-to-Vis-Probe Spectroscopy

Despite the insight on the ultrafast photophysical processes obtained before from the femtosecond UV-pump mIR-probe experiments, the question about the ultimate fate and the timescale of the decay of the initially prepared electronically excited state still remains uncertain. To gain a deeper understanding that will help to answer this open question, in addition, the complex was investigated by femtosecond UV-pump near-UV-to-visible-probe spectroscopy, in short UV/nUV-to-Vis. Measurements were conducted on a commercial transient absorption spectrometer (TAS, Newport/Spectra-Physics) at analogous experimental conditions compared with the previously presented UV/mIR studies. Owing to the superior temporal resolution (80 fs as compared to 250 fs on the UV/mIR experiment), this technique is especially suited to monitor the fate of the presumably extremely short-lived initial electronically excited state.

Time-resolved UV/nUV-to-Vis spectra for selected delays in the range from 150 fs to 28 ps between the pump and the probe pulses, are visualized in Fig. 5.19. It is remarkable that at very early delays, i.e., after 150 fs (depicted in light red in Fig. 5.19), the available spectral range is almost fully spanned by an induced absorption signal which is maximal at 506 nm with its tail extending even above 1000 nm and thus beyond the detection limit of the detector. However, at lower wavelengths of below roughly 400 nm, the sign of the signal is inverted and a prominent ground state bleaching signal can be identified manifesting the depopulation of the ground state. Though, comparing with

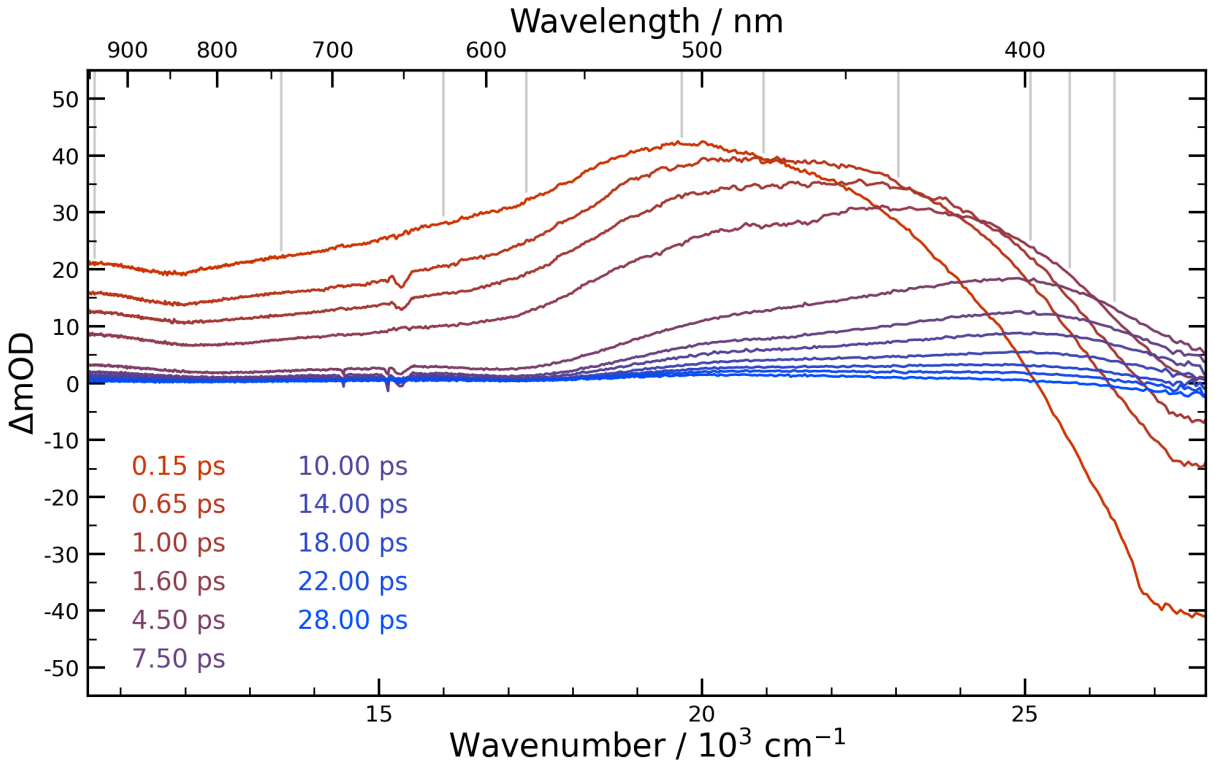

Figure 5.19.: *Time-resolved UV-pump nUV-to-Vis-probe spectra of trans−[Co(acac)2(N3)(py)] for selected delays between the optical pump and the probe pulses. Indicated by gray vertical lines are the spectral positions at which kinetic traces were extracted.*

the spectrum after 650 fs, it is noteworthy, that this bleaching signal recovers remarkably fast, i.e., it has lost the major part of its band integral within roughly 500 fs. Actually, within the first 1.6 ps the bleaching signal continues to decay until its is merely visible, then vanishes completely, and ultimately even a newly emerging induced absorption signal occurs instead with increasing delay time at this spectral position.

The spectral evolution within this short time period up to 1.6 ps is accompanied by pronounced spectral shifting. Thus, the band maximum initially located at 506 nm shifts dramatically to roughly 430 nm within only 1.6 ps translating into a frequency blueshift of roughly 3500 cm^{-1}. As is clearly visible, in addition, the band is subjected to significant spectral reshaping during this time interval. Whereas in the very first spectrum a band maximum is clearly discernible, shortly thereafter at 0.65 ps or 1.00 ps, respectively, the spectra appear almost flat at their maxima. Hence, it appears reasonable to assume, that the observed spectrum is actually the sum of two very broad and strongly overlapping bands. While the lower frequency component governs the shape of the IA band at early times extending it well into the near-infrared (NIR) range, it soon decays at the expense of the second one located at higher frequencies, but still remains visible as a frequency downshifted shoulder in later spectra beyond 4.50 ps. Based on this qualitative assessment, one may conclude, that the interconversion of two involved species is observed in the time-resolved spectrum. However, a clear isosbestic point that is usually considered as an unmistakable proof for such an assessment, remains absent throughout the entire delay range of the measurement. Still, in principle, two effects are conceivable that may preclude the observation of a well-behaved isosbestic point, that is (i) an additional frequency shift, in this case to the blue, that occurs for both bands in question or (ii) that the signals are still subjected to non-radiative electronic relaxation leading to diminished signal amplitude of the induced absorption band.

To reveal the underlying time constants that govern the spectral dynamics that may give a definite clue about the involved processes, fitting of the experimental data based on multiexponential models (c.f. Eq. 3.5) was applied. To this end, kinetic traces were extracted from the time-resolved spectra at the wavelengths indicated by dotted gray lines in Fig. 5.19. Experimental kinetic traces (open circles) and the corresponding fits (solid lines) are depicted in Fig. 5.20. In most cases, the data were reasonably well described by triple-exponential functions, i.e., featuring a total of three distinct time constants. The fit parameters deduced for a mathematical description of the data are compiled in Tab. 5.8. It is noteworthy, that kinetic traces in the near-infrared, e.g., at 943 nm decay monotonically and just as the probe wavelength decreases, i.e., with higher energy, an initial rise becomes visible whose amplitude grows as the probe frequency increases. Upon a close inspection of the data in Tab. 5.8, the time constants deduced from the fits are again observed to cluster around three distinct average values of (0.20 ± 0.05) ps, (1.5 ± 0.5) ps and (7.5 ± 2.5) ps, respectively.

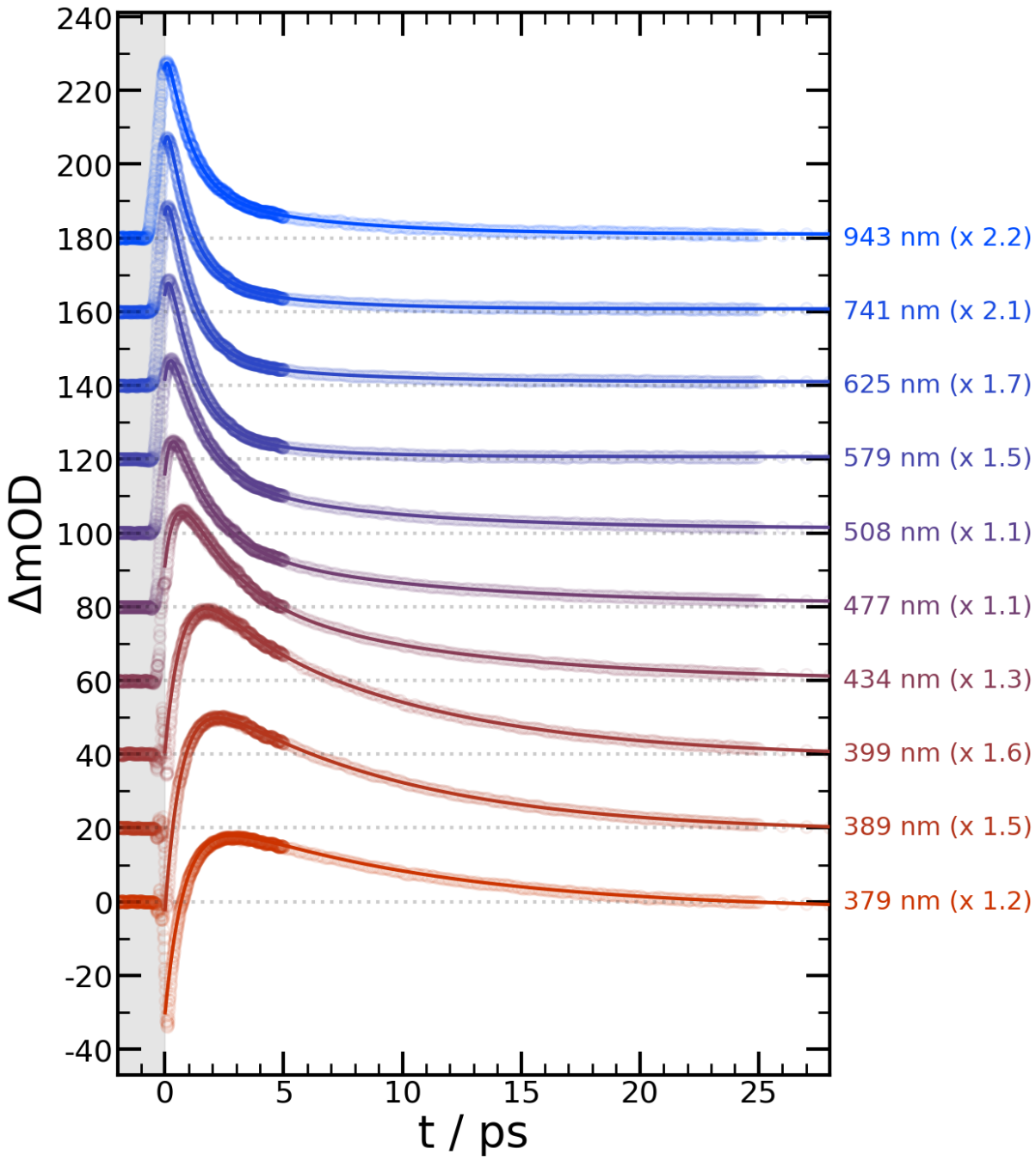

Figure 5.20.: *Kinetic traces at selected probe wavelengths as extracted from time-resolved UV-pump nUV-to-Vis probe spectra of trans−[Co(acac)2(N3)(py)]. For clarity, traces were shifted and scaled to a comparable level for visualization purposes. Experimental data are represented as blurred circles alongside the multiexponential fits to the data (solid curves).*

Strikingly, the latter is significantly close to the mean vibrational relaxation time for the vibrational modes attributed to the acac ligand deduced earlier (vide infra). Likewise, the UV/mIR data already revealed a time constant in the range of the intermediate time constant, in particular whenever the traces were governed by absorptive features. However, the fastest time constant in the sub-picosecond range was not detectable in the previously presented measurements owing to the limited time resolution. To further rationalize the observed dynamics, in an analogous fashion as presented before, the spectral shifting of the IA maximum was tracked and peak wavenumbers were again

Table 5.8.: *Time constants and amplitudes derived by multiexponential fitting of selected kinetic traces from the UV-pump nUV-to-Vis-probe spectra of trans–[Co(acac)2(N3)(py)].*

λ_{probe} / nm	A_0	A_1 / 10^1	τ_1 / ps	A_2 / 10^1	τ_2 / ps	A_3 / 10^1	τ_3 / ps
943	0.973	–1.079	0.138	4.440	1.00	1.164	5.63
741	0.338	–0.645	0.144	2.394	0.96	0.396	4.51
625	0.563	–0.955	0.171	3.237	1.02	0.396	5.81
579	0.436	–1.271	0.188	3.688	1.08	0.518	3.88
508	1.060	–1.791	0.229	4.145	1.38	1.327	7.36
477	0.758	–2.141	0.252	3.738	1.56	1.602	8.54
434	–0.228	–2.715	0.452	3.065	2.10	2.059	9.69
399	–0.762	–7.443	0.887	4.559	1.25	3.000	8.74
389	–0.893	–4.380	0.701	—	—	2.934	8.54
379	–2.150	–4.827	0.824	—	—	2.476	9.98
365	–2.400	–2.725	0.247	—	—	1.603	10.19

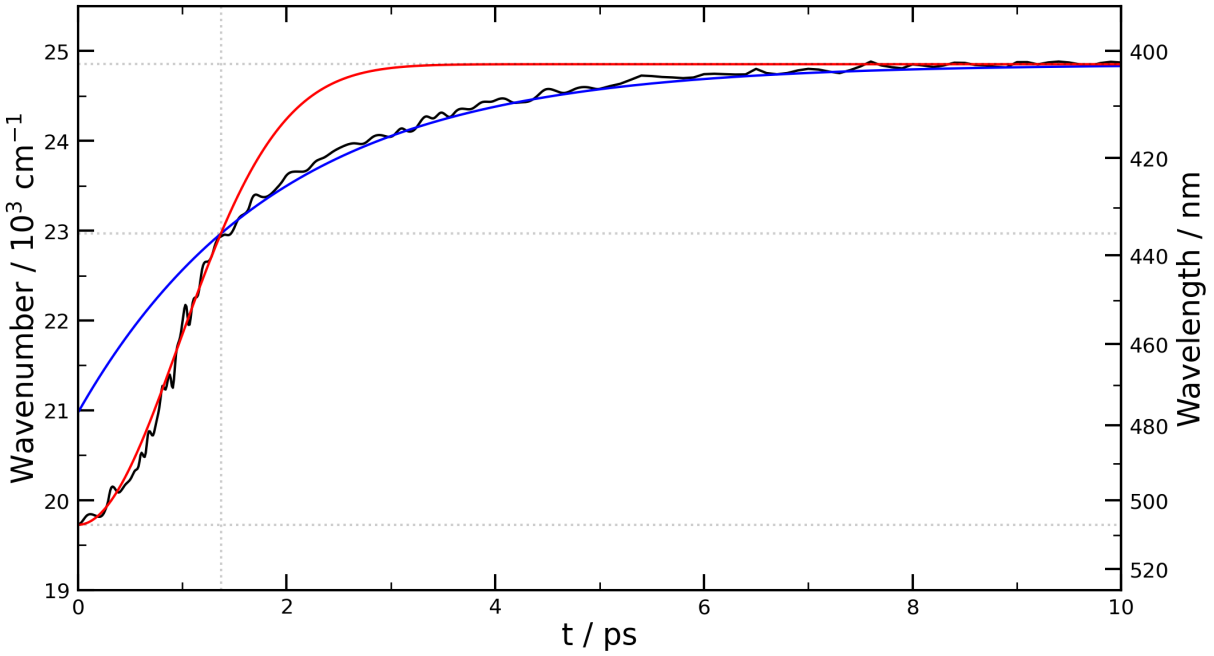

Figure 5.21.: *Peak position of the induced absorption band as observed in the experimental UV-pump nUV-to-Vis-probe spectrum of trans–[Co(acac)2(N3)(py)]. At early delays, the curve can satisfactory be fitted by a Gaussian rise with a 1/e time constant of 1.37 ps (red curve). At larger pump-probe delays, however, the data can be described by a single exponential function and a time constant of 1.9 ps (blue curve).*

plotted accordingly as a function of time (see Fig. 5.21). It is obvious, that the spectral shifting is governed by two components and can be described mathematical by a Gaussian exponential behavior (c.f. Eq. 5.17). At early delays, the Gaussian component featuring a time constant of 1.37 ps is dominant and causes the band to shift over a spectral range of roughly 3300 cm^{-1}, followed by a slower shifting behavior that is purely exponential in nature and entails a time constant of 1.9 ps which makes the signal shift by another 1900 cm^{-1} to higher energies.

This peculiar behavior that the shift of the maximum is brought about by two distinct components further corroborates that indeed the interconversion of two states is ob-

served, although it was not clearly deducible as such from the analogous UV/mIR measurement. However, it is noteworthy, that the spectral shifting of IA3 in the UV/mIR spectra discussed previously and the peak maximum in this measurement share some remarkable similarity, i.e., in both cases the majority of the spectral shifting occurs within the first two picoseconds. This agreement is indicative of the fact, that the spectral shifting observed on IA3 is not exclusively due to vibrational cooling of the N3 moiety in the electronic ground state, but most probably is superimposed by a process attributed to the interconversion of two distinct electronic states.

5.4.3. Discussion

Thus, the question about the nature of the two electronic states in question arises. According to TDDFT calculations as already discussed in section 5.2.4, following excitation at 266 nm an acac-to-cobalt charge transfer state, $^1\mathrm{LMCT}_{\mathrm{acac}}$, is prepared. However, the peculiar shape of the very first spectrum after 150 ps and the fact that it extends very far into the NIR suggests that this state is populated not exclusively. Especially, taking into account the ultrafast time constant of 200 fs deduced earlier, even after a delay as short as 150 fs, the population of the initially prepared state has decreased by roughly 50 % at the expense of another state.

In fact, a very interesting spectral behavior at very short pump-probe delays could already be seen in the UV/mIR spectrum (c.f. Fig. 5.16). Especially the induced absorption of the very first transient spectrum in the N3 stretching region exhibits a peculiar spectral shape. Not only is it extremely broad, but also very weak with respect to its spectral amplitude. Thus, to obtain a more quantitative metric going beyond this qualitative description, the band integrals of IA3 and the GSB3 in this spectral region as a function of the time delay were analyzed. Likewise, the absolute ratio of the two can be deduced accordingly, and the three quantities of interest are plotted against the pump-probe delay in Fig. 5.22. Both, the band integral of IA3 and GSB3 appear to follow a biexponential behavior and can satisfactorily well be fitted assuming this mathematical relationship. Whereas in case of the GSB, a time constant of 12.0 ps, that accounts for 93 % of the overall recovery, and a larger time constant to describe the behavior at later delays are found, in case of the IA the temporal evolution is governed by two distinct time constants that amount to 1.8 ps and 13.2 ps, respectively, among which especially the former is significantly striking. As was shown previously in related studies, at early pump-probe delays, the calculated integral ratio serves as a reliable metric to determine the number of closed-shell $\mathrm{N3}^-$ ligands attached to a transition metal center.[59,143] Thus, monitoring this quantity allows to precisely determine the number of intact azide vibrators attached to the metal fragment at a given instance of time after the electronic excitation. Therefore, the fact that at very early delays such as up to roughly 1 ps the integral ratio is significantly lower than 1, indicates that shortly after the electronic excitation the integrity of the $\mathrm{N3}^-$ group is disturbed. Still, the formation of free azide

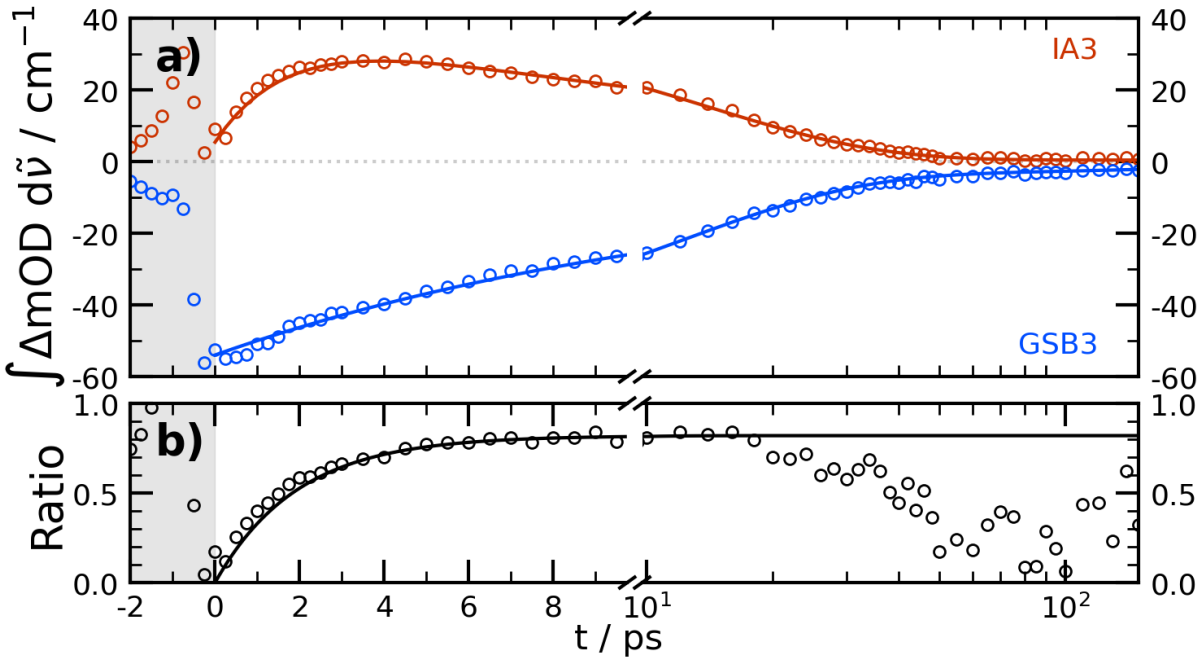

Figure 5.22.: *Time evolution of the integrated induced absorption and ground state bleaching signals (in red and in blue, respectively) in the azide stretching region of the UV-pump mid-infrared-probe spectra of trans−[Co(acac)2(N3)(py)] (upper panel). The absolute ratio of the two quantities increases from a value close to 0 to nearly 1 within the first ten picoseconds indicating that the integrity of the azide moiety is restored within this time interval.*

ions can be ruled out because of the absence of the very characteristic IR absorption band that is usually located slightly above 2000 cm^{-1}.[17,59] Thus, it has to be concluded, that the system has lost its azide absorber in an oxidative fashion. Within this scenario, two configurations are conceivable: (i) the system is best considered as a radical pair of the two isolated open-shell species $[Co^{II}(acac)_2(py)]^{\bullet}$ and an azidyl radical, $N_3^{\bullet}$, or alternatively (ii) that the system prevails in an azide-to-metal charge transfer state, $LMCT_{azide}$ in which the system is best regarded as $[Co^{II\bullet}(acac)_2(N_3^{\bullet})py]$. In either of the two cases the fast rise of the integral ratio to a value close to one is then an indication of the N3 moiety regaining its anionic character either via geminate recombination of the radical pair or via the relaxation of $LMCT_{azide}$ to a energetically lower lying state such as for instance the vibrationally hot electronic ground state.

Taking all the experimental findings and the insights gained from electronic structure calculations into consideration, the final interpretation can be summarized as sketched in Fig. 5.23. Following the illumination of *trans*-**[1]** by UV light of 266 nm, the system is excited into its $^1LMCT_{acac}$ state (root 23 of the TDDFT calculation), which entails an electron transfer from the acac ligand onto the metal center. Thus, this excitation can formally be regarded as a photoreduction of the Co(III) center or, conversely, as a photooxidation of the acac ligand. However, as the data obtained by UV-pump nUV-to-Vis-probe spectroscopy clearly indicate, this state is extremely short-lived, and thus very rapidly decays to the energetically close $^1LMCT_{azide}$ state (root 14), or even into the corresponding radical pair $\{N_3^{\bullet} \cdot [Co^{II}(acac)_2py]^{\bullet}\}$ on a timescale of 200 fs. This pri-

mary interconversion leading to the population of this state and affecting the integrity of the azide ligand, then gives rise to the peculiar shape of the very early UV-pump nUV-to-Vis-probe spectra, which feature induced signals that are extremely broad and extend far into the near-infrared. The fact, that already at very early delays the induced absorption constitutes the sum of the absorption profiles of these two states, hence gives rise to the atypical plateau in the vicinity of the maximum (see for instance the spectrum at 0.65 ps in Fig. 5.19). Likewise, this intermediate population of $^1\mathrm{LMCT}_{\mathrm{azide}}$ leads to the strongly diminished spectral amplitude of the IA in the azide stretching region at around 2000 cm^{-1} in the UV/mIR spectra. This interconversion of states formally involves an electron transfer from the azide moiety onto the acac ligand, thereby fully restoring the integrity of the acac ligand. However, following this pathway, instead the anionic and closed-shell character of the N3 moiety is lost as seen from the IA to GSB ratio in the azide stretching spectral region that is close to zero in the very first few picoseconds after the UV excitation (c.f. Fig. 5.22). The thus prepared state can subsequently either directly recover the ground state by geminate recombination of the $\{\mathrm{N3}^{\bullet} \cdot [\mathrm{Co}^{\mathrm{II}}(\mathrm{acac})2\mathrm{py}]^{\bullet}\}$ radical pair or decay to the singlet ^{1}MC state (root 4) by cobalt-to-azidyl charge transfer with a time constant of 1.8 ps. Likewise, this process clearly manifests itself in the Gaussian component of the shifting dynamics of the maximum of the IA in the azide stretching band because the number of intact N3 oscillators continuously increases. Hence, an assignment of the shifting of this band solely due to vibrational cooling dynamics must be rejected as premature, but instead can also be reasoned by the decay of the $^1\mathrm{LMCT}_{\mathrm{azide}}$ state. The overall sequence is then completed by the decay of the population in the ^{1}MC state, that replenishes the electronic ground state of the system although still in a vibrationally hot fashion. Finally, the hot ground dissipates this excess energy with a time constant of $1/(12.6 \pm 0.6)$ ps.

It is noteworthy, that *trans*-[**1**] exhibits a remarkable photochemical inertness. Thus, the time-resolved spectra indicate that within the achievable signal-to-noise ratio of our experiment, the system fully recovers the ground state within less then 100 ps. Hence, opposed to other related Co(III) system[59,66–68,106,125,143] *trans*-[**1**] does not undergo photochemically induced transformations to a significant extent. This peculiarity can be rationalized by the particular relaxation pathway we observed for this system. Although the initial $^1\mathrm{LMCT}_{\mathrm{acac}}$ state features energetically unfavored occupation of the anti-bonding cobalt $d_{x^2-y^2}$-orbital, the ultrafast collapse of this state prevents any events that would affect the chemical integrity of the system. Albeit, even the $^1\mathrm{LMCT}_{\mathrm{azide}}$ state entails population of the anti-bonding metal d_{z^2}-orbital, which in principle leads to softening of the dative bonds of the axial ligands, i.e., N3 and py, to the metal and should therefore ease the dissociation of either of the two. Here, the $\mathrm{Co}-\mathrm{N}_{\mathrm{py}}$ bond cleavage should be slightly energetically favored. Yet, also in this case, the short lived nature of the species (about 2 ps) rules out any photochemical pathways to be followed to an appreciable extent. Finally, although partial acac detachment on the ^{1}MC surface ap-

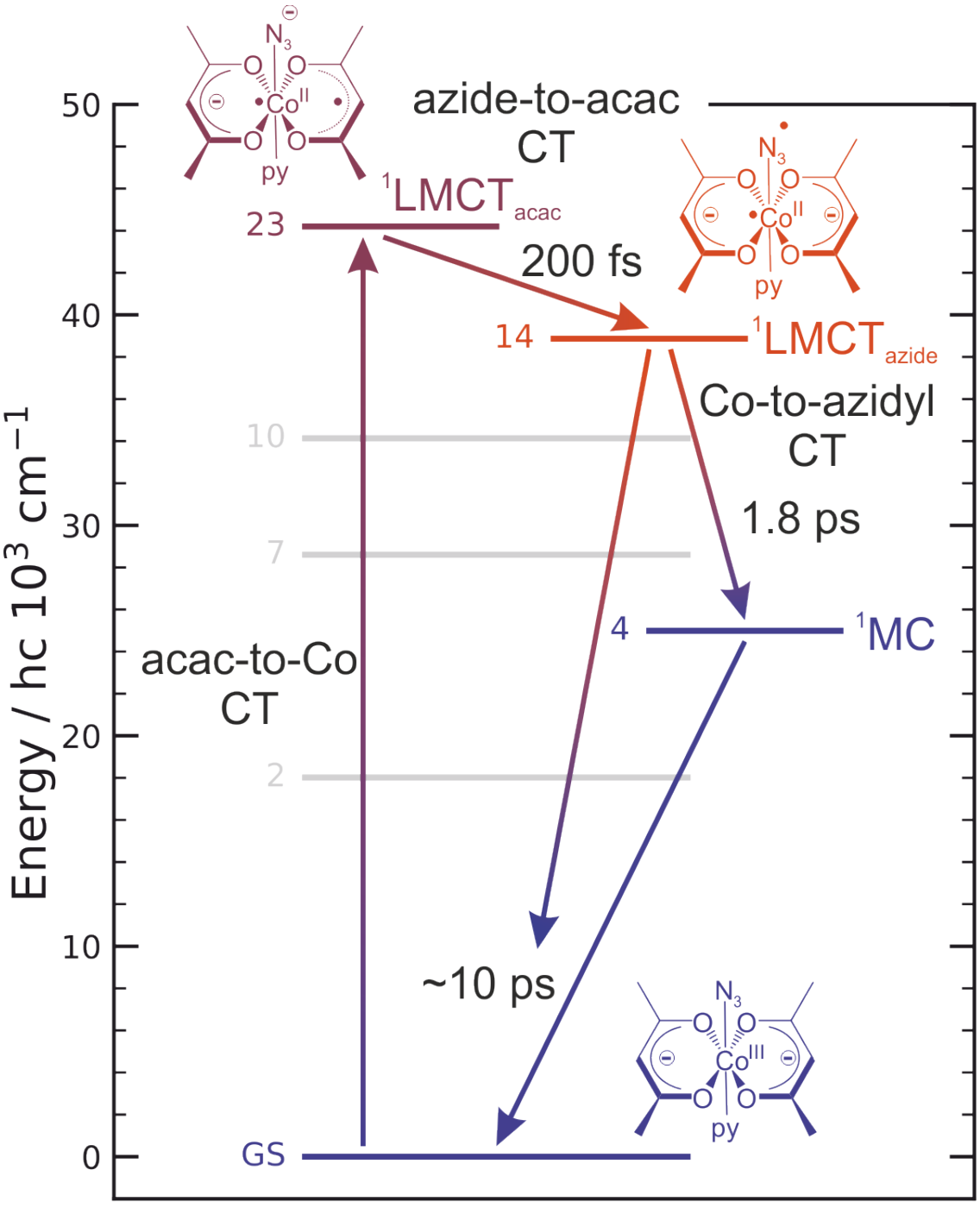

Figure 5.23.: *Primary processes occurring on the ultrafast timescale following UV excitation of trans−[Co(acac)2(N3)(py)] at 266 nm. The system is prepared in the extremely short-lived $^1LMCT_{acac}$ state (root 23) brought about by an acac-to-cobalt charge transfer transition. Subsequent azide-to-acac charge transfer on a timescale of 200 fs enables efficient population of the $^1LMCT_{azide}$ state (root 14) that can be regarded as a Co(II) complex to which an azidyl radical is ligated. The integrity of the azido ligand is then restored by a cobalt-to azidyl transition to ^1MC (root 4). This species ultimately then returns back to its ground state within roughly 10 ps.*

pears conceivable at first glance, it can be ruled out due to its high activation barrier. Thus, this process is highly complex from a mechanistic point of view, since it entails a dramatic conformational change of the acac ligand involving first a rotation across the bond axis of a carbonyl and the methylene carbon and subsequently across the Co-O axis. It is very likely that the energetic barriers involved in such a deformational process are too high and therefore effectively suppress this pathway. Hence, instead the system is driven to decay back to its ground state from the ^{1}MC surface within roughly 10 ps and dissipate its residual energy then by VER processes from the vibrationally hot molecule in its electronic ground state to its molecular surrounding.

6. Photophysics and Photochemistry of Diazido[1,2-bis(diphenylphosphino)-ethane]nickel(II)

As was pointed out in previous sections, the photochemistry of azido complexes is to a large extent governed by the electron configuration of the central atom. To further scrutinize this effect, in this section, the investigations on this class of compounds was therefore extended to the next heavier transition metal, nickel, listed to the right of cobalt in the periodic table. Although the ordinal number is higher only by +1, the coordination chemistry in comparison to cobalt usually is vastly different owing to the fact that in its most abundant oxidation state +II it frequently adopts a square-planar coordination geometry resulting from the particular *d*-orbital splitting in d^8 systems.

Following the general trends discussed before, the electron richness of the transition metal center should have a prominent effect on the photochemical and photophysical behavior of corresponding azido systems. Hence, to investigate this in more detail the diazido nickel(II) model system, diazido[1,2-bis(diphenylphosphino)ethane]nickel(II), was first prepared and fully characterized by stationary spectroscopic, X-ray diffraction and computational methods, and subsequently subject to time-resolved spectroscopic investigations. The work on this system in particular was inspired by research by Hennig and coworkers, who reported this system to be prone to nitrene formation, as already mentioned before.[27] Hence, the fundamental question which processes enable this photochemical behavior was addressed by UV-pump mIR-probe spectroscopy and will be discussed on the following pages.

6.1. Synthesis

The complex of interest was prepared via a two-step synthesis. In a first step, the corresponding precursor complex dichlorido[1,2-bis(diphenylphosphino)ethane]nickel(II) (Ni(dppe)Cl_2, $NiC_{26}H_{24}Cl_2P_2$) was prepared which subsequently was subjected to a ligand exchange reaction to furnish the target compound diazido[1,2-bis(diphenylphosphino)ethane]nickel(II) (Ni(dppe)$(N_3)_2$, $NiC_{26}H_{24}N_6P_2$, **[2]**).[144]

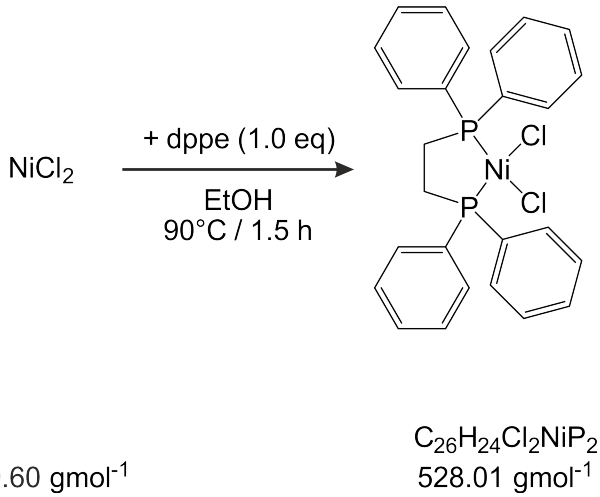

Figure 6.1.: *Synthesis of precursor complex Ni(dppe)(Cl)$_2$. In presence of one equivalent of the phosphine ligand, the product is readily obtained by a simple ligation reaction to the Lewis acidic Ni(II) center.*

6.1.1. Dichlorido[1,2-bis(diphenylphosphino)ethane]nickel(II)

The complex was prepared according to a synthetic route devised by Thananatthanachon and Lecklider.[145] 1.1427 g of anhydrous nickel(II)chloride (8.82 mmol, 1.04 eq., yellow-orange powder, $NiCl_2$) were suspended in 20 mL of absolute ethanol and provided in a 100 mL round-bottom flask. Then, 3.3941 g of 1,2-bis(diphenylphosphino)-ethane (8.52 mmol, 1.00 eq., white powder, $C_{26}H_4P_2$) were suspended in 20 mL of hot ethanol and slowly added to the reaction flask. After that, the thus obtained dark-brown suspension was then heated to reflux on an oil bath for 1.5 h while stirring vigorously. During the course of the reaction, the color of the suspension changed to dark-red and ultimately orange accompanied by precipitation of an orange solid. Once the reaction was complete, the heating source was removed. The reaction mixture was allowed to cool to room temperature and was subsequently chilled for additional 10 min at 4 °C in a refrigerator. Finally, the orange precipitate was filtered off, washed with small portions of ethanol (3×3 mL) and diethylether (3×3 mL) and dried at 50 °C under vacuum for 8 h. The product was obtained as an orange powdery solid with an isolated yield of 82 % (3.7086 g) with respect to the phosphine ligand.

6.1.2. Diazido[1,2-bis(diphenylphosphino)ethane]nickel(II)

The previously prepared precursor compound, $Ni(dppe)Cl_2$, was converted to the target complex **[2]** following a protocol devised by Bowman *et al.*[144] with minor modifications. To this end, 3.4442 g of dichlorido[1,2-bis(diphenylphosphino)ethane]nickel(II) (6.52 mmol, 1.00 eq., orange powder, $NiC_{26}H_{24}Cl_2P_2$) were suspended in 40 mL of dimethylformamide and provided in a 100 mL round-bottom flask that was covered with aluminum foil to prevent excessive exposure of the product to light during the course of the reaction. A solution of 0.9118 g of sodium azide (14.02 mmol, 2.15 eq., colorless crystalline solid, NaN_3) in 50 mL of methanol was subsequently added drop-

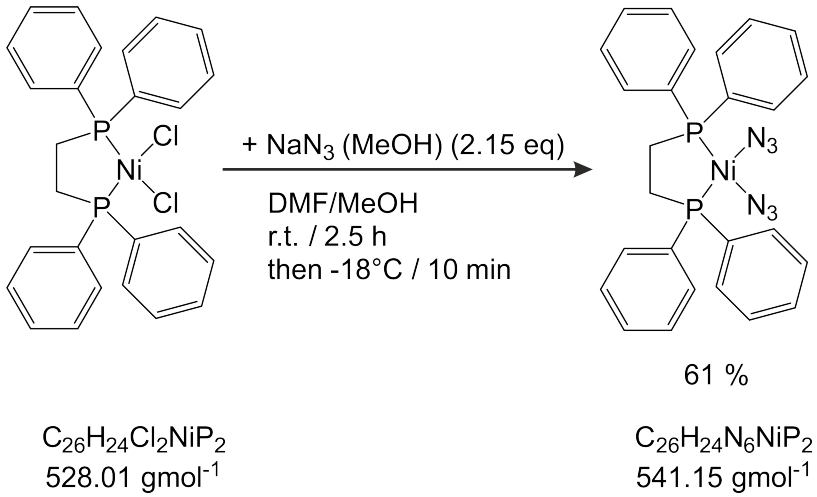

Figure 6.2.: *Synthesis of $Ni(dppe)(N_3)_2$. The target compound is readily obtained via ligand exchange reaction by treating the previously prepared precursor complex, $Ni(dppe)Cl_2$, with sodium azide.*

wise to the suspension via a dropping funnel while stirring vigorously over the course of 15 min. Upon addition of the azide source, the orange solution turned reddish. Once the addition was complete, the reaction mixture was stirred for another 2.5 h at room temperature upon which an intensively red colored precipitate formed. After that, the reaction mixture was chilled at −18 °C for 10 min for further precipitation. Afterwards, the precipitate was filtered off and washed with cold methanol (2×3 mL), cold toluene (1×3 mL) and finally with diethylether (2×3 mL). The product was then dried to constant weight under vacuum for roughly 6 h. 2.1519 g of the reddish-orange target compound were obtained with an isolated yield of 61 % with respect to the starting precursor complex.

Analytical Characterization

Elemental Analysis: *Anal. Calcd.* for $C_{26}H_{24}N_6NiP_2$: C, 57.71; H, 4.47; N, 15.53. Found: C, 55.45; H, 4.487; N, 15.71.

IR: (22 °C, CH_2Cl_2): $\tilde{\nu}$ (cm^{-1}) (ϵ, $L\,mol^{-1}\,cm^{-1}$) = 1438 (544) ($\nu_s(N_3)$), 1606 (w) (i.p. CH_{ar}-bend), 2043 (1604) ($\nu_{oop,as}(N_3)$), 2060 (2790) ($\nu_{ip,as}(N_3)$)

UV-Vis: (22 °C, CH_2Cl_2): λ_{max} (nm) (ϵ, $L\,mol^{-1}\,cm^{-1}$) = 266 (17680) ($\pi_{dppe} \rightarrow d^*_{xy}$), 300 (21010) ($\pi_{azide} \rightarrow d_{x^2-y^2}$), 490 (1405) ($d_{xy} \rightarrow d_{x^2-y^2}$)

6.2. Molecular and Spectroscopic Properties

6.2.1. Single Crystal X-Ray Diffraction Studies

The molecular structure of **[2]** was inferred via X-ray diffractometry. To this end, single crystals suitable for diffraction studies were grown from a saturated dichloromethane solution of the compound at 4 °C over the course of two weeks and were obtained as clear orange red blocks. Measurements were conducted on a STOE IPDS-2T diffractometer employing Mo-K_α radiation.

The complex was found to crystallize in the monoclinic space group Cc and features four molecules per asymmetric unit. Detailed crystallographic information are compiled in Tab. 6.1. The thus determined molecular structure of **[2]** in the solid state is depicted in Fig. 6.3 and an overview of selected structural parameters is provided in Tab. 6.2.

In the derived molecular X-ray structure, the complex adopts approximately C_2 symmetry. Here, the C_2 axis is defined by the nickel(II) ion and the center of the C−C bond of the ethylenic backbone of the dppe ligand. As is frequently observed for transition metal complexes of d^8-electron configuration, **[2]** obviously adopts square planar coordination geometry across the nickel(II) center with P−Ni−N angles that are close to the ideally expected value of 180° (174.66° and 175.94°, respectively). Thus, the metal ion, the phosphorus and the N_α atoms of the ligands almost lie in one plane.

This geometric feature gives clear indications to the electronic structure of the system, especially, since it is commonly observed that in the presence of weak ligands instead a tetrahedral arrangement is adopted for Ni(II) d^8-complexes. In these cases owing to Jahn-Teller distortion the system usually features an open-shell ground state manifesting itself in the paramagnetic character of such compounds.[30,146–150] However, following general trends, the phosphine ligand apparently enforces a sufficiently strong ligand field splitting, which renders the square planar diamagnetic configuration energetically favorable due to its good σ-donor properties.[30]

Table 6.1.: *Crystallographic parameters of Ni(dppe)$(N_3)_2$. Dimensions and angles of the unit cell defined by parameters a, b, c and α and β, respectively, following usual conventions. Number of molecules per asymmetric unit specified by parameter Z.*

crystallographic parameter	**[2]**
crystal system	monoclinic
space group	Cc
a / Å	10.3167(3)
b / Å	15.7207(3)
c / Å	15.5371(4)
α / °	90
β / °	101.611(2)
Z	4

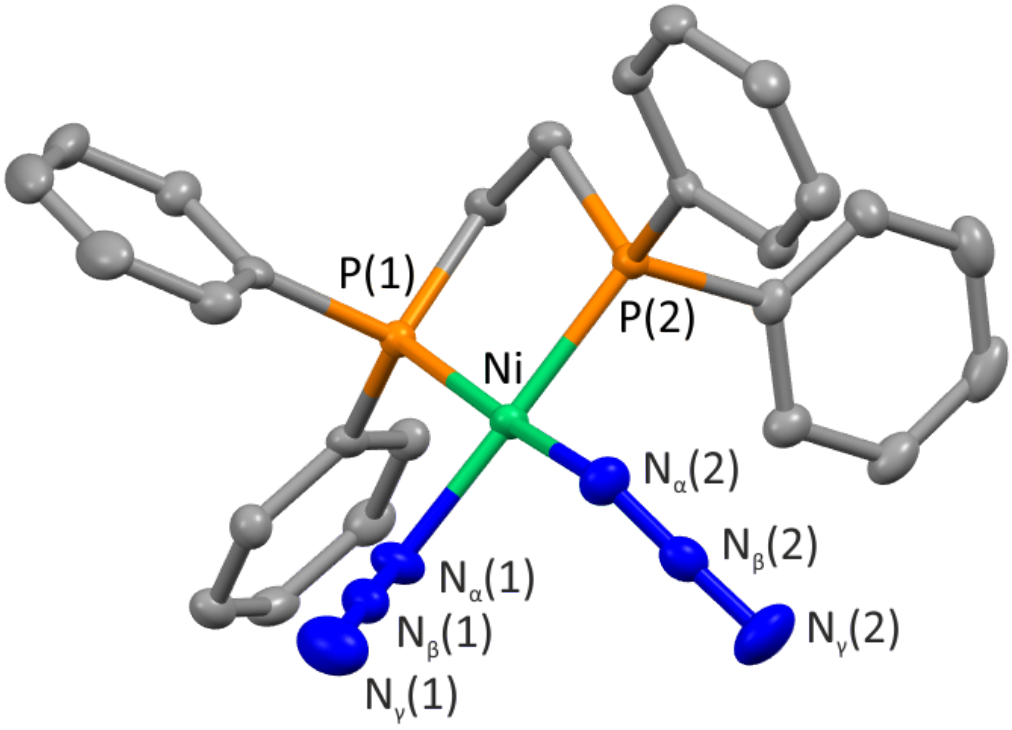

Figure 6.3.: *Molecular structure of $Ni(dppe)(N3)_2$ as determined from single crystal X-ray diffraction. Hydrogen atoms are omitted for clarity. Carbon in gray, nitrogen in blue, phosphorus in orange and nickel in green.*

Moreover, indeed, a close inspection of the molecular structure reveals, that the slight deviations from ideal square planar geometry, that are observed, can be attributed towards steric effects. In order to reduce the unfavorable steric interaction between either of the azido ligands and the phenyl ring that is oriented into a similar direction, the N3 groups tend to slightly move out of the plane spanned by the two phosphorus atoms and the central metal ion. In addition, the angle spanned by *cis*-adjacent ligand atoms across the nickel center (86.86°, 90.54°, 89.51° and 93.20°) only slightly deviate from 90° as would be expected and especially, the deviation of the P−Ni−P angle from this value can in part be understood in terms of the comparably small bite angle of the dppe ligand that was reported to amount to 78.1°.[151]

Interestingly, the two azido ligands adopt such a configuration that the angle between the two corresponding $N_\alpha - N_\beta$ bond vectors amounts to roughly 92.3°. Most likely, this arrangement is enforced by the space filling requirements of the dppe phenyl rings. Hence, by adopting this orientation, the azide ligands fit well into the areas in space that are left free by the organic rests and thus reduce steric stress.

In the complex, the Ni−P bonds (2.143 Å and 2.160 Å) appear slightly elongated in comparison with the Ni−N_α bonds (1.913 Å and 1.910 Å); a relative elongation of roughly 12 %. Yet, the bond lengths are in the typical range of dative Ni−P and Ni−N

Table 6.2.: *Structural parameters of Ni(dppe)(N_3)$_2$ as determined from single crystal X-ray diffraction. Bond lengths are in Å, bond angles and dihedral angles are in °.*

structural parameter	**[2]**
Ni−P(1)	2.1431(15)
Ni−P(2)	2.1597(14)
Ni−N_α(1)	1.913(5)
Ni−N_α(2)	1.910(5)
N(1)−N_β(1)	1.180(7)
N_β(1)−N_γ(1)	1.172(7)
N_α(2)−N_β(2)	1.169(7)
N_β(2)−N_γ(2)	1.169(8)
P(1)−Ni−P(2)	86.86(5)
N_α(1)−Ni−P(1)	90.54(16)
N_α(1)−Ni−P(2)	174.66(16)
N_α(2)−Ni−P(1)	175.94(15)
N_α(2)−Ni−P(2)	89.51(15)
N_α(2)−Ni−N_α(1)	93.2(2)
N_β(1)−N_α(1)−Ni	122.8(4)
N_γ(1)−N_β(1)−N_α(1)	175.2(6)
N_β(2)−N_α(2)−Ni	117.5(4)
N_γ(2)−N_β(2)−N_α(2)	175.8(6)

bonds, respectively,[152,153] and thus follow the general trend of increasing covalent radii as the ordinal number increases. Interestingly, the C−P−C angles of the dppe ligand tend to be very close to the ideal tetrahedral angle of 109.5° indicating that to a considerable amount the *3s*-orbital is admixed to the molecular orbital accommodating the lone pair that emerges in dative boding to the metal center.

Particular attention should be paid to the nitrogen-nitrogen bond lengths of the azido ligands. Opposed to the frequently observed shortening of the $N_\alpha-N_\beta$ bonds upon ligation, often interpreted as preconfiguration towards decomposition via extrusion of dinitrogen[41] as discussed before (c.f. section 2.2.3), in the present case, the $N_\alpha-N_\beta$ and the $N_\beta-N_\gamma$ bonds (1.180 Å and 1.169 Å or 1.172 Å and 1.169 Å, respectively, for either of the azido ligands) are nearly equally long. Thus, following this interpretation, the $N_\alpha-N_\beta$ bonds of the azido ligands should be thermally comparably robust which is corroborated by the observation, that the compound can be handled under thermal conditions without any particular precautions and without any tendency toward spontaneous detonation.

6.2.2. FTIR Spectroscopy

Moreover, the complex of interest was investigated by FTIR spectroscopy. The vibrational spectrum of **[2]** was measured in dichloromethane solution ($c = 11.5\,\mathrm{mmol\,L^{-1}}$) as described previously in section 4.1 and the prominent spectral ranges are shown in Fig. 6.4b). Apparently, the entire spectrum is essentially dominated by the strong

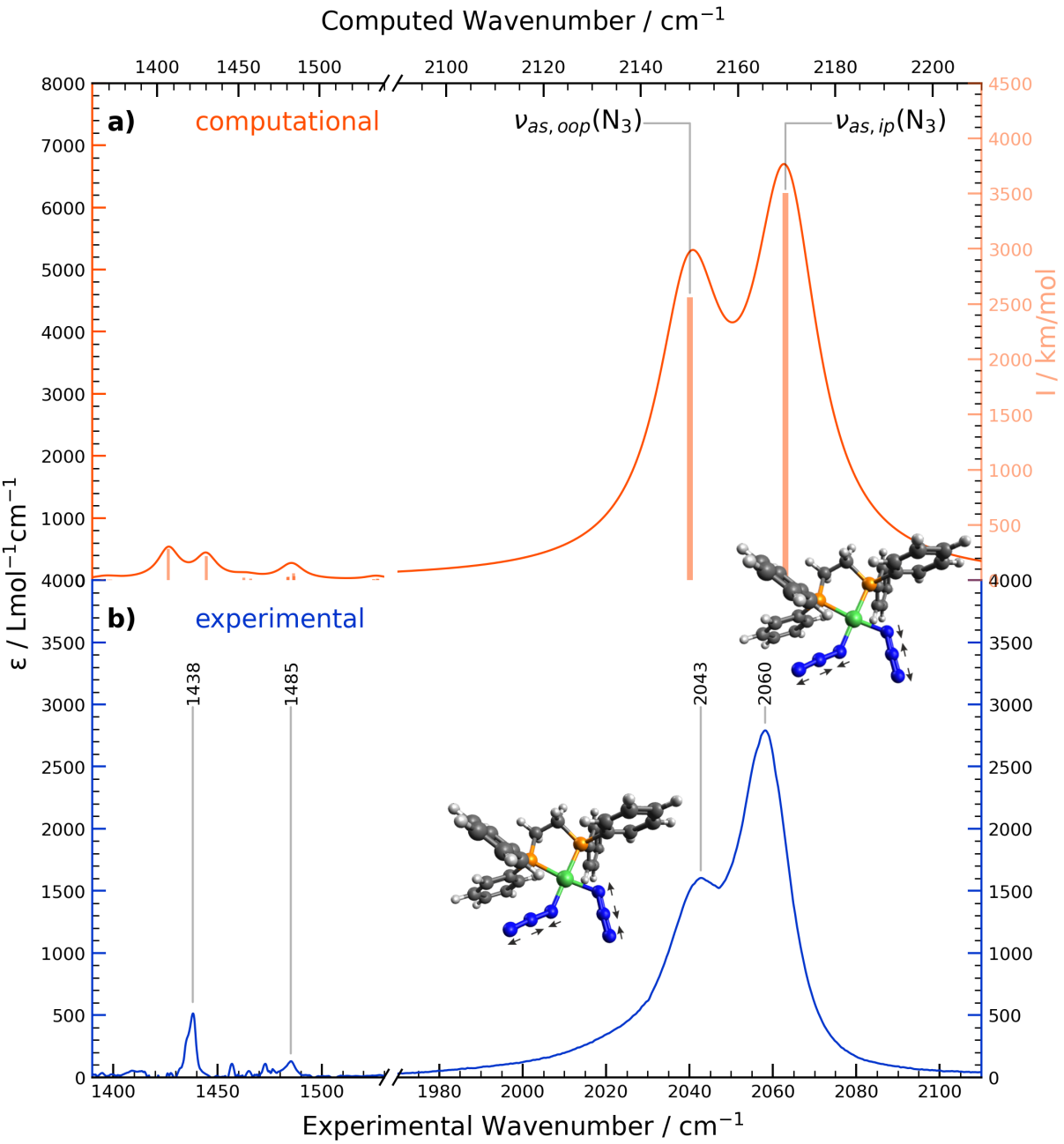

Figure 6.4.: *FTIR spectrum of a freshly prepared solution of $Ni(dppe)(N_3)_2$ in liquid dichloromethane ($c = 11.5\,mmol\,L^{-1}$) at room temperature (20 °C) (b) and comparison with computed IR spectrum (a). Note the axis break in the abcissa.*

peaks due to the vibrations of the azido ligands in the frequency range from 2000 cm^{-1} to 2100 cm^{-1} . In fact, the remaining peaks due to vibrations of the dppe ligand proved to be either rather weak and broad in nature, or to be covered by solvent absorptions. Therefore, in the spectrum depicted in Fig. 6.4 a special focus is set to the azide stretching spectral range. An overview over discernible vibrational absorption peaks as observed in the spectrum including an assignment based on theoretical calculations can be found in Tab. 6.3

In the spectrum two distinct absorption features are observable in the azide stretching range above 2000 cm^{-1}. As already mentioned in previous sections, this spectral range is very characteristic of ligated azide since the vibrational transitions attributed

Table 6.3.: *Frequencies and intensities of azide vibrational normal modes of* **[2]** *as determined experimentally and calculated by theoretical methods.*

	$\tilde{\nu}$ / cm^{-1}		intensity	
mode	exp.	comp.	ϵ / $L\,mol^{-1}\,cm^{-1}$	I / $km\,mol^{-1}$ (comp.)
$\nu_{s,ip}(N3)$	1438	1406	544	195
$\nu_{as,ip}(N3)$	2060	2187	2790	2907
$\nu_{as,ip}(N3)$	2043	2168	1604	2475

to the asymmetric azide stretching vibrations usually fall in this energy regime.[120] Interestingly, in this case alongside a rather strong absorption band peaking at 2060 cm^{-1} ($\epsilon = 2790\,L\,mol^{-1}\,cm^{-1}$) a redshifted shoulder is clearly discernible at 2043 cm^{-1} whose extinction coefficient is significantly decreased ($\epsilon = 1604\,L\,mol^{-1}\,cm^{-1}$).

The observed occurrence of two bands with significantly differing absorption coefficients can readily be understood in terms of the normal modes of the system. Firstly, the asymmetric vibration of the two azide ligands can occur in an in-phase fashion, i.e., both the $N_\alpha - N_\beta$ and the $N_\beta - N_\gamma$ bonds, respectively, of the two ligands stretch and compress simultaneously. This in-phase mode, in the following referred to as $\nu_{as,ip}$, features an increased transition dipole moment owing to a constructive interaction of the dipole vectors involved as sketched in the inset in Fig. 6.4. Alternatively, the asymmetric stretching modes can combine in an out-of-phase fashion, with a phase-shift between the two vibrations of 180°, denoted as $\nu_{as,oop}$. In the latter case, either of the bond stretches while that corresponding bond of the second azide ligand compresses and vice versa leading to a partial cancellation of the dipole vectors.

This qualitative consideration was corroborated by calculation of harmonic frequencies within the ωB97X-D/def2-TZVPP DFT framework (c.f. Appendix C.2.1). However, interestingly a frequency calculation performed on a local minimum of the potential energy surface maintaining the C_2 symmetry that was structurally related to the molecular arrangement deduced from X-ray crystallography, failed to predict an IR spectrum that would be in line with the experimentally observed one. Instead, the energetic ordering of the normal modes was found to be inverted in this case, i.e., the peak due to the $\nu_{as,ip}$ mode is observed at lower energies and the $\nu_{as,oop}$ band appears as a blueshifted shoulder instead. Only if the symmetry of the complex is allowed to break during geometry optimization a local minimum is found in which the two N3 moieties are arranged nearly at a right angle. Thus, only in this case the computed IR spectrum is qualitatively in line with the experiment, indicating that in solution the complex is subject to a molecular distortion that decreases the point group symmetry of the system, or alternatively that the ideal C_2 molecular symmetry in the solid state is enforced by packing effects in the crystal.

Albeit the rest of the spectrum is not very conclusive, still the symmetric stretching modes of the azides can be identified as a faint absorption peak at roughly 1438 cm^{-1}

and thus in the typical spectral range.[120] As rationalized before, due to the symmetric nature of the atomic motions to a large extend the dipole vectors cancel out, thereby rendering the transition very weak. Anyhow, in light of these observations, it should be stressed out, that the $\nu_{as,ip}$ and the $\nu_{as,oop}$ constitute ideal vibrational marker bands, since any change in the molecular structure directly will manifest itself by changes in the respective spectral range. Therefore, for investigation by UV-pump mIR-probe spectroscopy presented in the following special attention was paid to this spectral window.

6.2.3. UV/Vis Spectroscopy

In order to obtain a deeper understanding of the electronic properties of **[2]**, the system was investigated by means of UV/Vis spectroscopy. Hence, the electronic absorption spectrum of the compound in liquid dichloromethane solution ($c = 0.96\,\mathrm{mmol\,L^{-1}}$) (c.f. Fig. 6.5) under ambient conditions was measured as described previously (vide supra). Moreover, to assist the interpretation of the spectrum and the assignment of absorption bands, the electronic structure of the system was studied by means of TDDFT calculations on the ωB97X-D/def2-TZVPP level of theory in ORCA 5.0.2 (for details see Appendix C.2.1). For a realistic picture the obtained TDDFT spectrum was subjected to Gaussian broadening. A constant full width at half maximum of $4000\,\mathrm{cm^{-1}}$ for all absorption bands involved was assumed and proved to be feasible to reproduce the experimental spectrum sufficiently well.

As a comparison, both the computationally (a) and the experimentally determined (b) electronic absorption spectra of **[2]** are depicted in Fig. 6.6. Strikingly, the spectrum can be divided into three spectral regions. As is frequently observed for transition metal complexes, at lower photon energies from 400 nm to 660 nm ($15\,000\,\mathrm{cm^{-1}}$

Figure 6.5.: *Solution of $Ni(dppe)(N_3)_2$ in dichloromethane. The intense orange-red color of the complex arises from d-d excitations of the nickel center, most prominently the $d_{xy} \rightarrow d_{x^2-y^2}$ transition.*

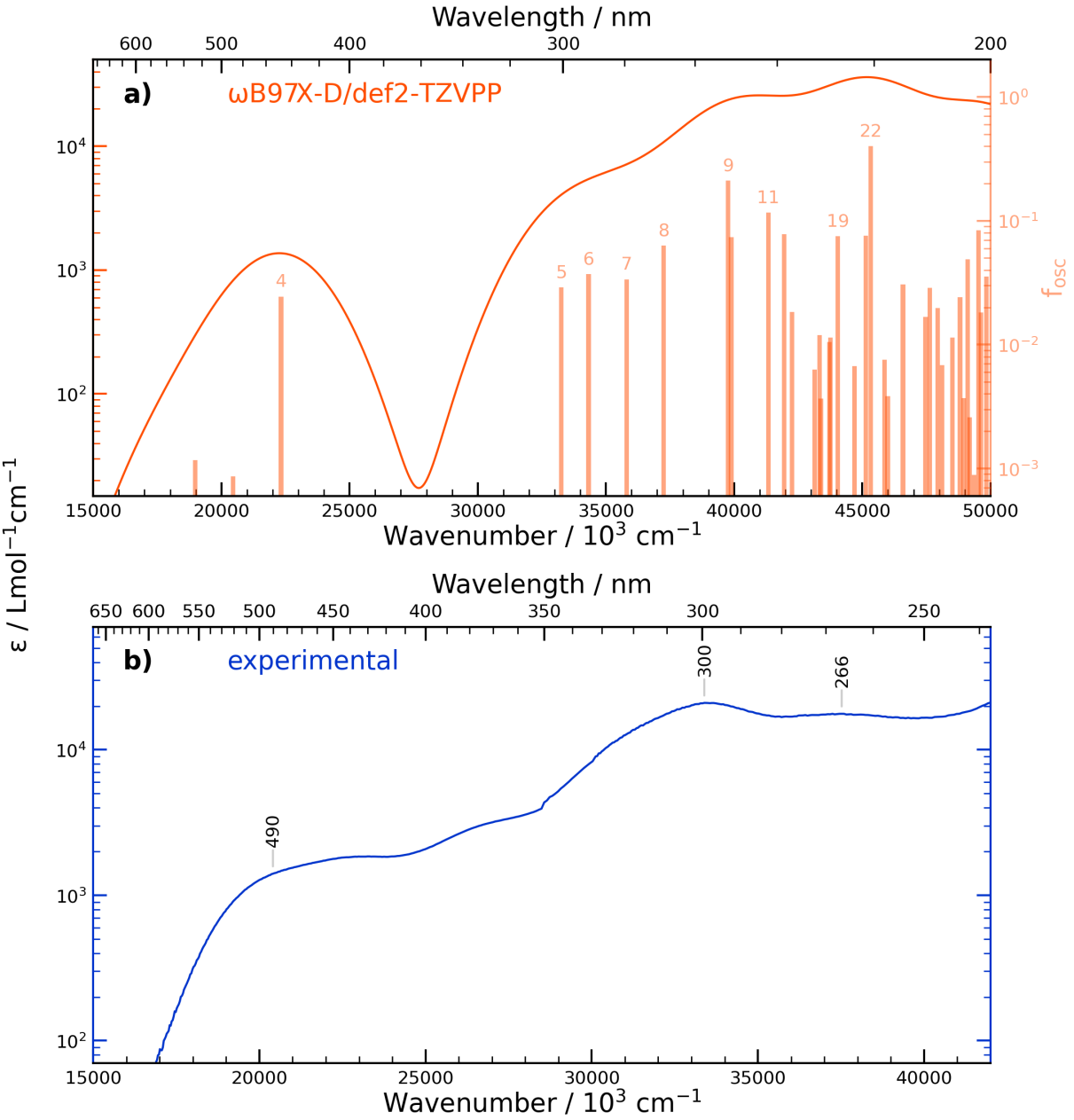

Figure 6.6.: *UV/Vis spectrum of Ni(dppe)(N3)2 recorded in liquid dichloromethane at 20 °C (b) and computational TDDFT spectrum calculated on the ωB97X-D/def2-TZVPP level of theory (a).*

to 25 000 cm^{-1}), the visible range of the electromagnetic spectrum is governed by relatively weak *d-d* transitions due to the reasoning discussed in previous sections (c.f. section 5.2.4). In case of d^8-systems, in total three different *d-d* excitations are expected; $d_{z^2} \rightarrow d_{x^2-y^2}$, $d_{xy} \rightarrow d_{x^2-y^2}$ and $d_{yz} \rightarrow d_{x^2-y^2}$. According to detailed studies on Ni(II) d^8-systems, the $d_{xy} \rightarrow d_{x^2-y^2}$ transition is expected to be the most prominent one.[60] However, the remaining transition bands are obscured by this stronger one and introduce some asymmetry to the observed absorption profile, which in fact can be observed also experimentally. This transition is found to correspond to root 4 of the TDDFT calculation which is observed to be the most prominent. As can be seen from the electronic difference densities attributed to this excitation and plotted in Fig. 6.7, the calculation unequivocally reveals the *d-d*-transition nature of the corresponding absorption band.

Interestingly, the *d-d* excitations are essentially the only optical transitions that are induced by visible light, and hence must be held responsible for the characteristic orange-red color of the compound (see Fig. 6.5).

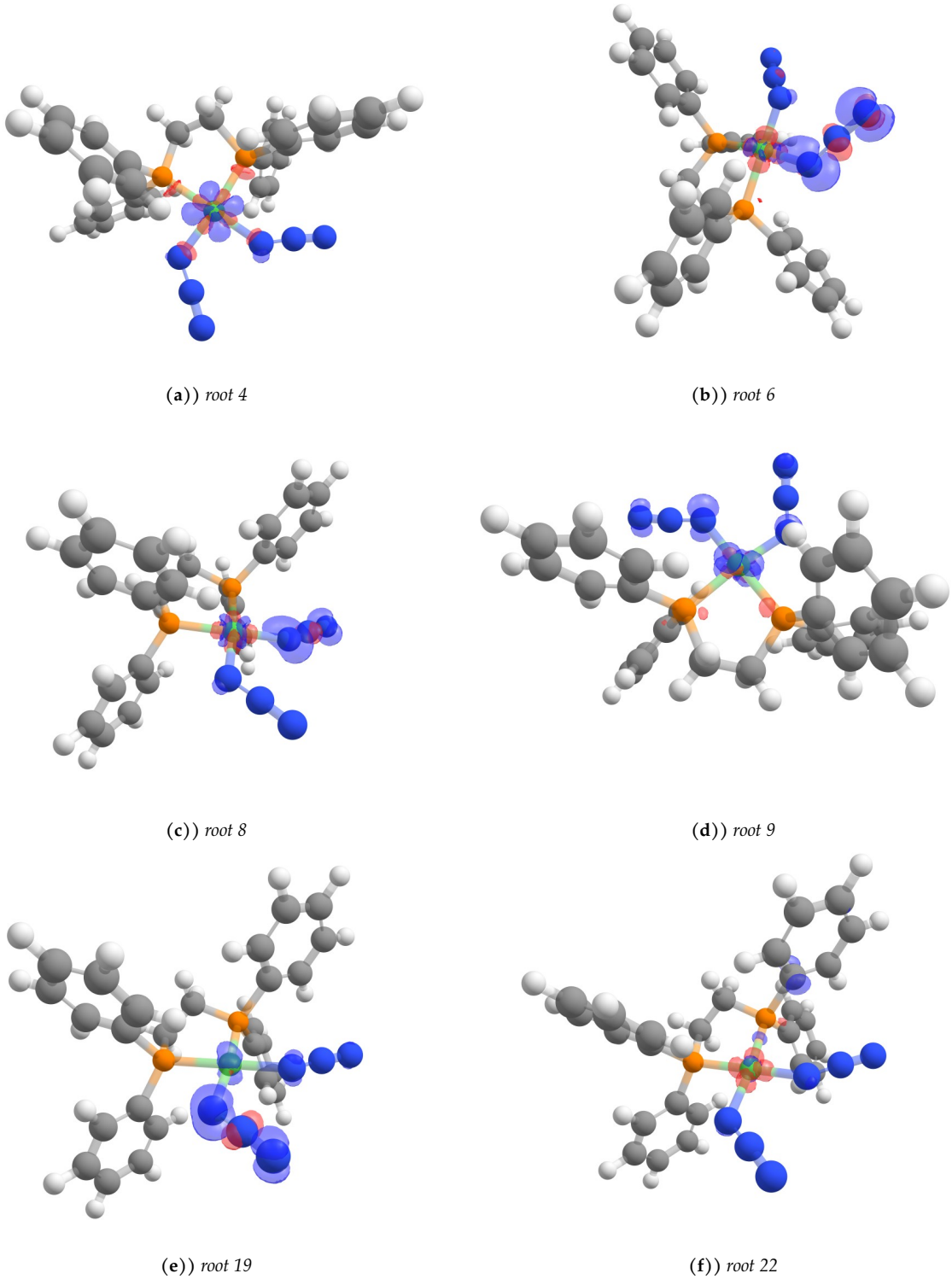

(**a**)) *root 4*

(**b**)) *root 6*

(**c**)) *root 8*

(**d**)) *root 9*

(**e**)) *root 19*

(**f**)) *root 22*

Figure 6.7.: *Difference densities attributed to selected roots as computed on the ωB97X-D/def2-TZVPP level at an iso level of 0.012 electrons/Å^3. Red shaded areas indicate points in space that contain excessive electron density in comparison to the ground state of the molecule and blue areas those from which electron density is removed.*

In turn, the near UV range of the spectrum from 400 nm down to 300 nm (25 000 cm^{-1} to 33 300 cm^{-1}, respectively) is dominated by azide-to-metal charge transfer transitions that correspond to roots 5 to 8 in the TDDFT calculation. According to the results of the computation, these transitions mainly involve the transfer of electron density from π-orbitals of the azide ligands to vacant nickel *d*-orbitals of appropriate symmetry, and thus can be regarded to entail a transient photooxidation of the azide ligand. Hence, the states populated by theses transitions, can be regarded as containing a photoreduced Ni(I) center, to which an azidyl ligand is ligated.

Finally, at even lower wavelengths of less then 300 nm, in addition electronic transitions involving the organic dppe ligand can be observed. Most prominently, root 22 of the TDDFT calculation can be understood as a promotion of electron density from the dppe ligand to the metal center and gives rise to the strong absorption at 266 nm.

6.3. UV-Pump mIR-Probe Spectroscopy

As previous investigations by Hennig and coworkers suggest,[27] **[2]** is subjected to photolytic decomposition upon irradiation with light of appropriate energy and by performing trapping reactions strong indications for the intermediacy of a nickel nitrene complex were found. In order to corroborate this hypothesis and deduce the exact photophysical and photochemical mechanism that enables this reactivity, UV-pump mIR-probe spectroscopy is the method of choice to monitor the proclaimed transformations in real time due to its structural sensitivity, and allows for determination of the relevant time constants of the underlying processes.

6.3.1. Experimental

To this end, the ultrafast light-induced dynamics of the system were investigated on our experimental setup as described previously. Measurements were conducted on solutions of **[2]** in dichloromethane ($c = 11.0\,mmol\,L^{-1}$). The solution employed for these measurements was kept in a closed system between the sample reservoir and the measurement cell of an optical thickness of 200 µm, which was comprised as described before. Constantly refreshing the sample volume in the measurement cell by a gear pump proved to be critical to exclude any detrimental effects on the measurement by photoproducts that were observed to be formed from the reaction sequence and tend to form a solid precipitate and stick to the CaF_2 windows over the course of the experiment. Moreover, it was also necessary to ensure, that the cell was in constant movement to avoid concentration of the laser energy to a single spot over an extended period of time. Additionally, the solution was used no longer than for an average set of measurements of 45 min. As soon as degradation of the solution set in to an appreciable amount, which was readily identified by clear changes in the observed spectra, the solution was

discarded and was replaced by a fresh one. Also, if necessary the cell was exchanged prior to any further measurements to rule out distortions of the actual signals of interest due to deposits on the windows to the best possible way.

As it soon turned out, the relevant photochemical processes of **[2]** occur on timescales that cover several orders of magnitude from the picosecond up to the microsecond regime. Unfortunately, as discussed in section 4.2, due to technical and optical limitations, the direct collection of all the relevant data in a single run is out of scope. Therefore, the data were collected in several runs. First, spectra up to pump-probe delays of roughly 2 ns were recorded via simply delaying the probe pulse using a motorized delay stage. For larger delays, the approaches presented in section 4.2 were followed, i.e., via shortening of the optical path length of the pump beam or by introduction of an electronic delay between the two laser systems.

Therefore, in fact, the measurements presented in the following, in actuality represent four distinct sets of measurements that vary by how the pump-probe delay was actually realized. Certainly, absolute signal amplitudes and frequency axes of the measurements differ slightly since it was virtually impossible to ensure a perfectly identical beam path and alignment between sets of measurements. Applying interpolative techniques and scaling, all the available spectra were afterwards artificially stitched together to obtain a single, larger full data set.[1]

Following this approach the time-resolved pump-probe spectra of **[2]** were collected over a vast range of different pump-probe delays. The compound was excited with UV pulses whose center wavelength was set to 266 nm realized by third harmonic generation of the 800 nm fundamental and the response of the system was monitored in the mid-infrared. The pump energy was chosen carefully and was set to roughly 6 µJ since with this setting it was possible to observe the signals of interest with a satisfactory signal-to-noise ratio. Even higher pump energies proved to be detrimental to the spectral quality owing to excessively fast decomposition of the sample that led to deposits on the CaF_2 windows and large offsets on the measured signals because of the formation of solvated electrons from the dichloromethane solvent. Moreover, this way multiphoton processes were ruled out as much as possible, which otherwise would overcomplicate the measured signals.

6.3.2. Discussion of Time-Resolved Spectra

The spectral response of the sample to the UV excitation was traced in the mid-infrared with the probe pulses tuned to cover a spectral range from 1880 cm^{-1} to 2150 cm^{-1} that is essentially governed by the two asymmetric azide stretching modes of the complex (cf. section 6.2.2). An overview of selected pump-probe spectra is depicted in Fig. 6.8 (panel a)). Additionally, a representation of the full dataset (ranging from 1880 cm^{-1}

[1] To perform the required data post-processing steps, a software package was developed in Python 3.9. A copy of the code can be obtained via `https://github.com/IPTC-MPC/tresspec_toolkit`.

to 2150 cm^{-1} in the frequency domain and from 0 ps to 350 µs) in a contour map representation is provided in Fig. 6.8c) where regions colored in red and blue constitute signals of positive (IA) and negative sign (GSB), respectively. Special attention should be paid to the logarithmic nature of the vertical axis due to the fact that pump-probe delays over several orders of magnitudes were scanned. As frequently observed, at very early delays, for instance after 0.25 ps, the time-resolved spectrum is essentially governed by the presence of a pronounced redshifted absorption whose spectral profile resembles that of a log-normal distribution. This signal is accompanied by the corresponding bleaching signal centered at 2060 cm^{-1} indicating the depletion of the ground state. The fact, that at early delays an induced absorption is visible gives indications that the thus prepared excited state is bound with respect to the motion along the normal mode coordinates of the azide stretching vibrations. Thus, instantaneous formation of a nitrene complex seems highly unlikely from this perspective. Instead, over the course of the first few picoseconds the initially broad IA band undergoes a blueshift and spectral reshaping. Thus, similar as in the previous chapter (c.f. section 5.4.1), it appears reasonable to interpret this behavior as the process of vibrational cooling, i.e., the dissipation of excess vibrational energy to energetically lower lying modes or onto the solvent.

Interestingly, however, here the shifting of the signal appears to result in the formation of a newly formed IA band that is centered at roughly 2047 cm^{-1} and is marked in Fig. 6.8c) (*) indicative of the formation of a relatively long-lived state. Hence, it appears as if an interconversion between the vibrationally hot system and a state of yet to be determined nature is observed. As is obvious from the time-resolved spectra, the species associated with this signal apparently is present in the solution for a long period of time from roughly 20 ps to roughly 10 ns. On the picosecond timescale this system even appears to be stationary as can be seen from the near flat nature of the corresponding kinetic trace at 2047 cm^{-1} extracted from the spectra (c.f. Fig. 6.11) and vanishes only very slowly with an appreciable decrease of the signal intensity only setting in on the nanosecond timescale. Albeit the signals become exceedingly week, interestingly, on this timescale this intermediate state appears to interconvert into another state as can be judged by an isosbestic point at 2036 cm^{-1} in the time-resolved spectra in Fig. 6.8a). While the aforementioned IA vanishes a very faint and broad induced absorption appears in the range of roughly 2030 cm^{-1} (**). However, it should not go unmentioned, that also the recovering of the GSB signal seems to continue as the new, faint band grows. This observation suggests that the state at 2047 cm^{-1} can either decay at the expense of yet another new species or alternatively recover the ground state.

To address the obvious question about the nature of the species that gives rise to the signals described before, again the evolution of the ratio between the integrated transient bleach and the induced absorption proved to be insightful and its temporal dependency is plotted in Fig. 6.9. As can be seen at very early delays of a few picosec-

onds, the integrated spectral amplitude of the GSB is larger than that of the IA and thus their ratio deviates from the ideal value of 1 that is expected for a species that entails all azide moieties intact. However, it should be regarded with great care and premature conclusions should be avoided, since at early delays, the spectral window of the experiment is insufficient to cover the entire spectral range of the very broad redshifted IA band. After roughly 10 ps the signal has undergone spectral blueshifting and reshaping

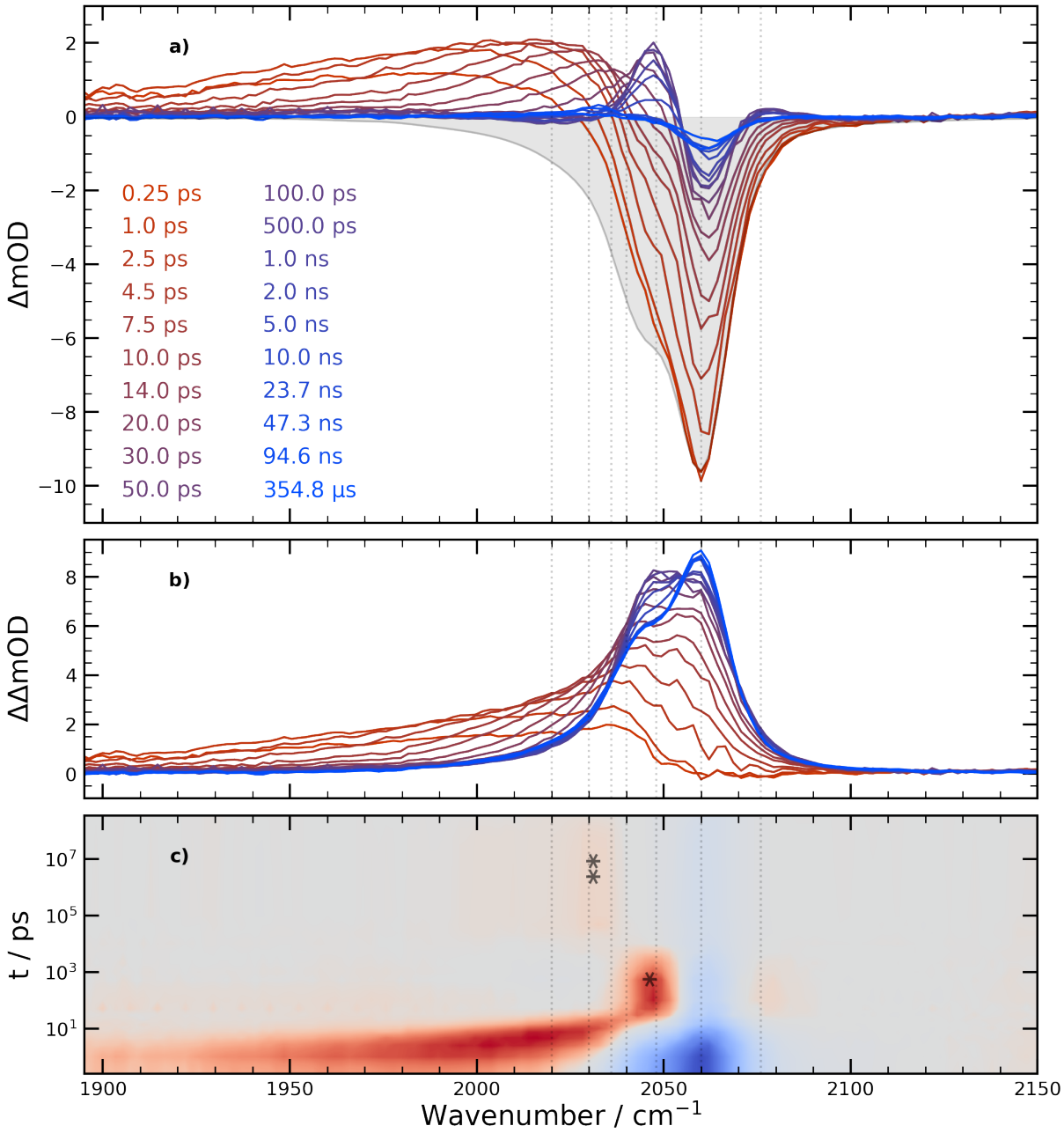

Figure 6.8.: *Time-resolved UV-pump mid-infrared-probe spectra of $Ni(dppe)(N_3)_2$ recorded in the azide stretching spectral region for selected delays between the pump and the probe pulse (a). Purely absorptive product spectra calculated by adding the properly scaled inverted FTIR spectrum to the time-resolved spectra are depicted in (b). A full overview of the data set in a contour plot representation is depicted in (c). Transient signal at 2047 cm^{-1} due to the intermediate population of the triplet state of the parent compound, $Ni(dppe)(N_3)_2$ ($S = 1$), marked by *. From this state the system can decay to the triplet nitrene, seen as a faint signal at 2033 cm^{-1} (**). Frequencies, at which kinetic traces were extracted, are indicated by dotted vertical lines in either of the plots.*

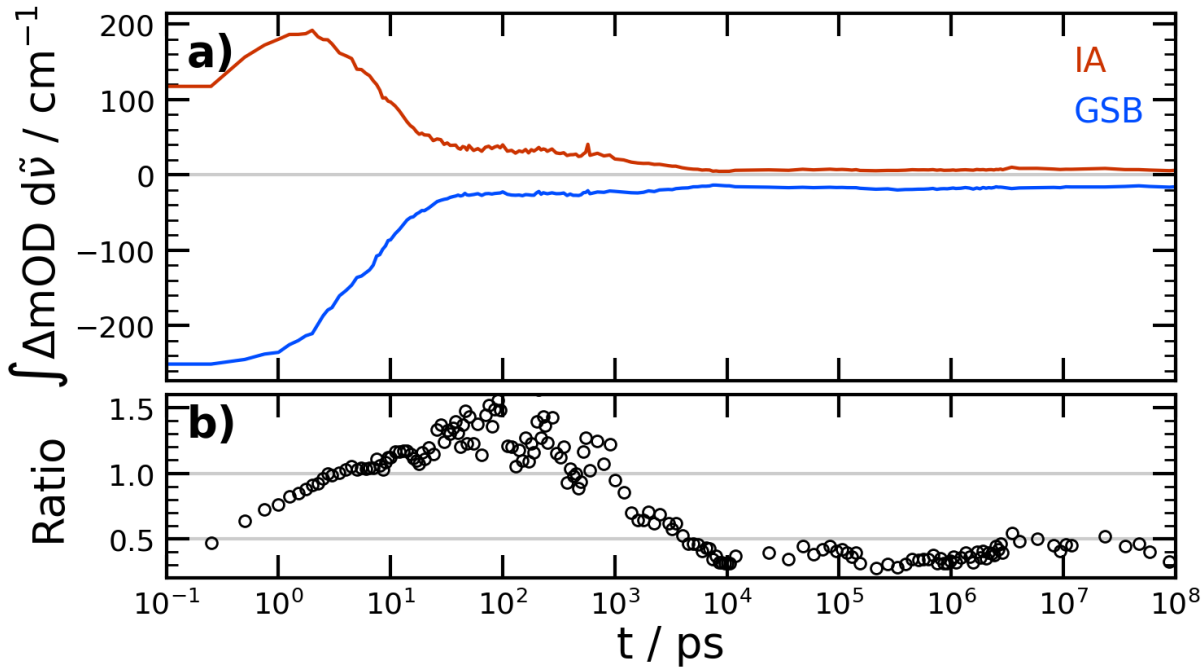

Figure 6.9.: *Temporal evolution of the integrated induced absorption (red) and the ground state bleach (blue) as a function of increasing pump-probe delay (a). The ratio of the two quantities shown in (b) drops to a value close to 0.5 in the time window from 1000 ps to 10 000 ps indicating the loss of one azide vibrator and is interpreted in terms of triplet nitrene formation.*

that for intermediate and later delays the analysis can be considered reliable. Albeit the calculated integral ratio is heavily affected by noise, it is still evident that in the range from roughly 10 ps to 1000 ps this value is close to 1. Thus, it can be inferred that during this time range the integrity of both azide moieties is maintained and no decomposition has occurred. A dramatic change is observable however in the range from 1000 ps to 10 000 ps after the UV pump excitation as the integral ratio significantly decreases to a value close to 0.5. This behavior is also clearly visible from the time-resolved spectra recorded at respective delays. The GSB approximately remains unchanged, but the IA significantly continues to vanish, indicative of an effective loss of azide vibrators. After roughly 10 ns a stationary picture is obtained. Within the noise limit no further changes are observable neither concerning the time-resolved spectra nor the integral ratio. Taking these observations into consideration, it must be concluded that on this timescale a decomposition of at least one azide moiety occurs which in analogy to the findings by Hennig and coworkers[27] must be understood by the formation of a nitrene. However, this photodecomposition seemingly features an induction period, i.e., does not occur instantaneously upon UV excitation. Thus, prior to the formation of a nitrene complex, another species must be present in the solution at intermediate times that ultimately paves the way to the formation of the photoproduct.

To identify the nature of this species, quantum chemical calculations were carried out on a number of putative reaction products and intermediates (c.f. Appendix C.2). First of all, it should be noted, that in principle apart from the closed-shell configuration of the system, also the triplet state of the system can be formulated. Albeit this state

is thermally out of reach at ambient conditions, photoexcitation may lead to the population of this state as a consequence of an intersystem crossing event. Interestingly, when trying to perform geometry optimizations of a putative nitrene complex formed by cleavage of one $N_\alpha - N_\beta$ bond, on the singlet surface no stable geometry could be obtained that contains a terminal singly bound nitrogen atom. Instead, over the course of the optimization the electron deficient nitrogen center stabilizes itself via insertion into the Ni−P bond which is analogous to a reactivity pattern that is well-known and was reported on selected nitrido or nitrene complexes.[154–156] Thus, if even for a short instance in time a singlet nitrene species should be present, it should be possible to identify it indirectly via the characteristic iminophosphorane vibration at roughly 1100 cm^{-1}. Experiments to detect a signal that would corroborate this hypothesis, however, remained unsuccessful suggesting that this reaction scheme is unfeasible for this particular system. On the other hand, on the triplet surface the DFT calculations readily converge to a geometry that can be identified as a triplet nitrene based on the analysis of the spin density. Additionally, also the triplet state of the parent system represents a minimum structure and can be prepared in silico. Interestingly, however, in this electronic state no longer a square-planar coordination geometry across the nickel center is adopted, but instead the phosphorus and the nitrogen N_α ligand atoms span a coordination tetrahedron. In fact, it is well known that d^8-systems that feature a triplet ground state, tend to adopt a tetrahedral arrangement across the metal center. This effect can be rationalized by the *d*-orbital ordering in either of the two coordination geometries in question.[123] Thus, based on these findings the observed spectro-temporal behavior gives strong indications that indeed a triplet nitrene is formed as the ultimate reaction product. Due to spin conservation arguments, the required release of dinitrogen therefore most likely occurs within the triplet manifold which requires an intersystem crossing event before this reaction can take place. Therefore, taking all these indications into account, the IA that is observed at 2047 cm^{-1} and appears stationary for intermediate times must be assigned to the triplet state of the molecule. Considering the fact, that the population of this state involves a complicated molecular deformation, a direct formation of this state appears highly unlikely. Thus, the overall interpretation is well in line with the usual observation that nitrenes in most cases preferably adopt a triplet ground state.[72]

The proposed mechanism can be summarized as is laid out in Fig. 6.10. Upon excitation with UV light of 266 nm wavelength, the system is prepared in the $LMCT_{dppe}$ state. This state rapidly disposes of the excessive vibrational energy and ultimately undergoes intersystem crossing to the triplet surface rendering the parent complex in its triplet configuration. This species, however, ultimately extrudes dinitrogen on later timescales and thus furnishes the sought-after triplet nitrene that must be held responsible for the observed photochemical reactivity.

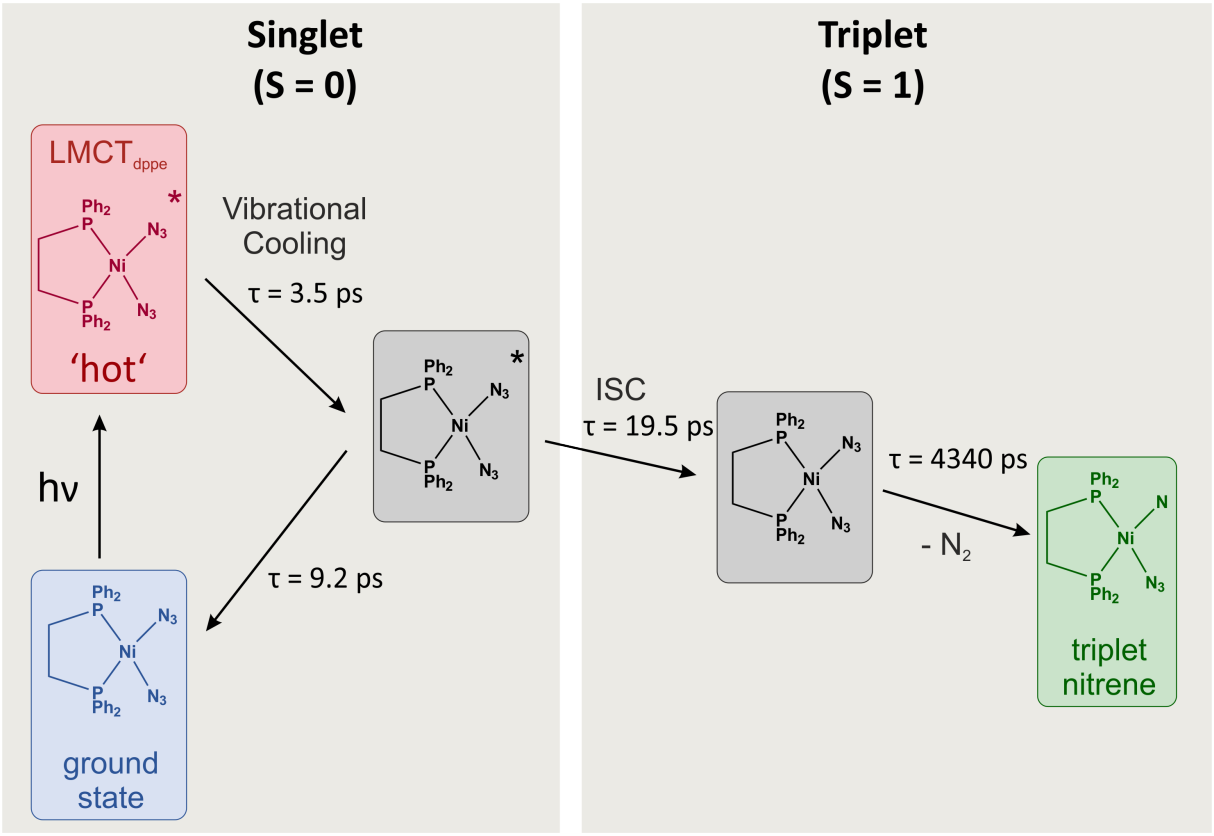

Figure 6.10.: *Photochemical mechanism of light-induced triplet nitrene formation upon UV excitation of* $Ni(dppe)(N3)2$ *at 266 nm. The pump pulse transfers the system to the* $LMCT_{dppe}$ *state which disposes of its excess vibrational energy within the first few picoseconds. The vibrationally cold excited state subsequently either repopulates the ground state or undergoes intersystem crossing (ISC) with a time constant of 19.5 ps. Once the system is on the triplet surface, it extrudes dinitrogen to render the respective triplet nitrene species at a rate of 1/4340 ps.*

6.3.3. Kinetic Analysis

It readily can be seen that all steps in the proposed mechanism are purely monomolecular. In fact, on short timescales considered here up to several nanoseconds, no bimolecular reactions are observable since even the most efficient diffusion controlled reactions are impossible owing to the comparably slow diffusive processes that are required. If at all, reactions involving the solvent are conceivable since in any case solvent molecules are in close vicinity to a potentially reactive intermediate. However, due to the huge excess of solvent molecules, the rate equation of such a reaction would collapse to a rate law of pseudo first order. Thus, the rate equations constitute a set of coupled linear differential equations. Systems like these can readily be solved for analytically involving the matrix exponential of the transition matrix and rate equations derived thereof can be phenomenologically expressed as a sum of several exponential components as described by Eq. 3.5. It should be noted, that an analysis going beyond the empirical fitting requires precise knowledge about the behavior of the spectral shifting and the underlying band shapes, which usually is available only for the simplest of cases. Still, to deduce a more quantitative picture and to assess the lifetimes of the species involved

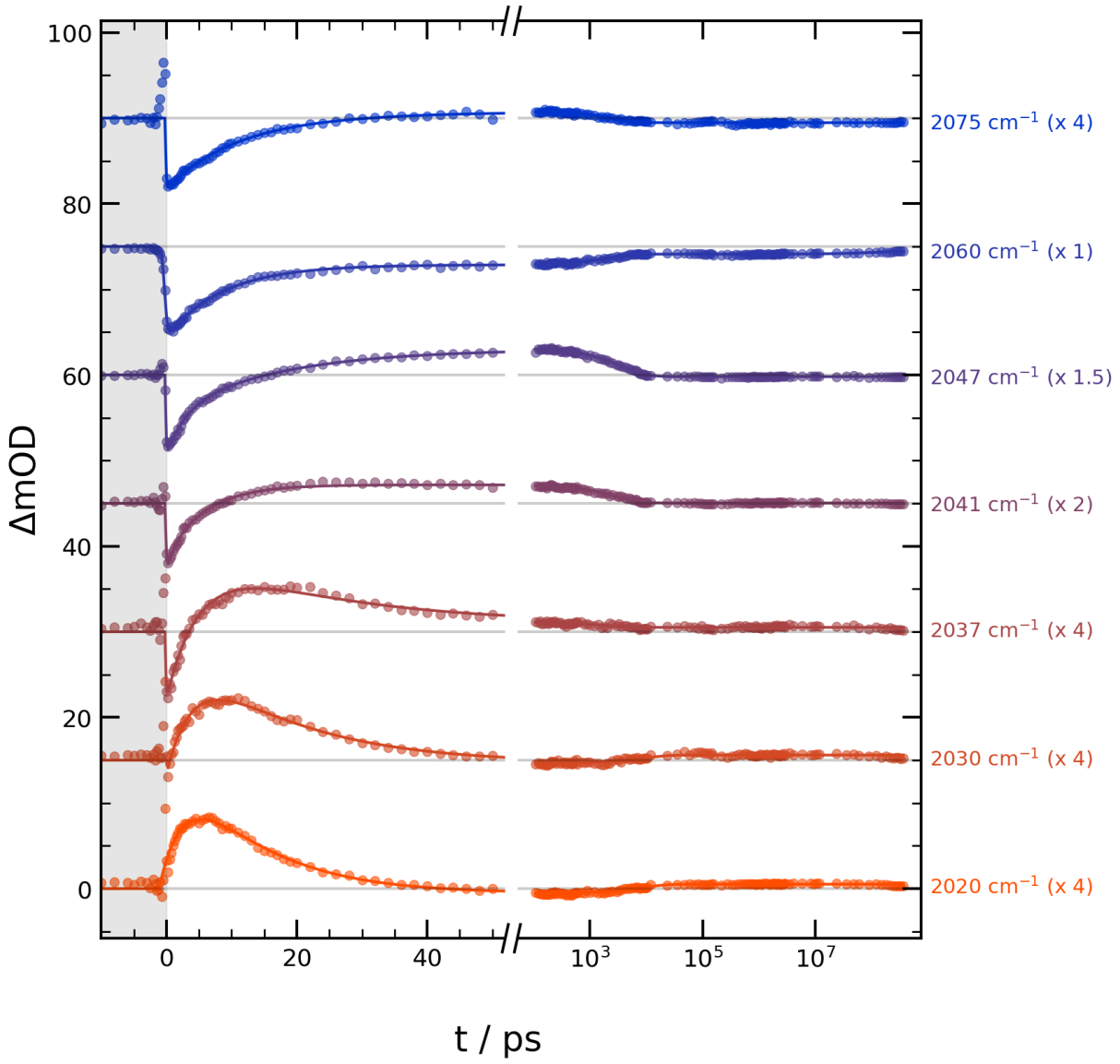

Figure 6.11.: *Kinetic traces extracted at selected probe frequencies from the UV-pump mid-infrared-probe spectra of Ni(dppe)(N3)2. For clarity, traces were shifted and scaled for visualization purposes. Experimental data are represented as circles alongside the multi-exponential fits to the data (solid curves).*

in the proposed mechanism, kinetic traces at selected frequencies were extracted and analyzed based on Eq. 3.5.

Taking a closer look at the time constants derived from phenomenological multi-exponential fits to selected kinetic traces (c.f. Fig. 6.11), it is striking that they tend to cluster around four principle values. A faster time constant in the picosecond range is essentially prominent when considering the spectral range from 2020 cm^{-1} to 2047 cm^{-1} that averages to 3.5 ps. Owing to the fact that the questionable frequency range is heavily affected by spectral shifting at early times, it appears reasonable to interpret this time constant in terms of the lifetime of the vibrationally hot excited state. Within this timescale, the excited state relaxes to its vibrational ground state. However, when considering kinetic traces at frequencies close to or at the spectral position of the ground state bleach at 2060 cm^{-1}, another apparent time constant can be found that amounts to

Table 6.4.: *Time constants and amplitudes obtained from multi-exponential fitting of the experimental data. The observed time constants seem to cluster around four values. Here, the first and smallest time constant of roughly 3.5 ps, is observed whenever the evolution of the signal is governed by spectral shifting and can therefore be understood in terms of vibrational cooling of the excited state. A time constant in the range of 9.2 ps describes the repopulation of the ground state in the singlet manifold. Molecules that reside in the excited state sufficiently long, however, can undergo intersystem crossing to the triplet diazido compound with a time constant of roughly 19.5 ps. On the triplet surface, the system ultimately releases dinitrogen to give rise to the nitrene on a timescale of about 4340 ps.*

$\tilde{\nu}$ / cm^{-1}	A_0	A_1	τ_1 / ps	A_2	τ_2 / ps	A_3	τ_3 / ps	A_4	τ_4 / ps
2020	0.13	–5.68	3.9	5.60	11.9	—	—	–0.27	8161
2030	0.15	–4.30	4.1	—	—	3.98	16.5	–0.24	8855
2037	0.13	–4.82	5.2	—	—	2.60	20.6	0.14	2188
2041	0.02	–0.84	1.2	–4.13	6.0	—	—	1.08	2814
2047	–0.14	–3.23	3.0	—	—	–4.97	17.2	2.20	3626
2060	–0.89	—	—	–8.64	8.7	—	—	–1.27	2127
2075	–0.13	—	—	–1.85	10.3	–0.42	23.8	0.34	2621

9.2 ps and must be attributed to the ground state recovery within the singlet manifold from the vibrationally cold excited state.

In spectral ranges close to the position of the IA band at 2047 cm^{-1} that has previously been assigned to the triplet state, however, the respective kinetic traces frequently exhibit a time constants of about 15 ps to 25 ps. Thus, it is reasonable to assume that this time constant is attributed to the process involved in the population of the triplet state. Hence, following this rationale the intersystem crossing occurs with a time constant of roughly 19.5 ps. This value, in general, falls in the same time range, that can be estimated qualitatively from the spectra, in which the peak due to the semi-stationary triplet state emerges in the spectrum at 2047 cm^{-1} (c.f. Fig. 6.8). The formation of the triplet nitrene, in turn, manifests itself in the kinetic traces as a time constant in the range of a few thousands of picoseconds, $\langle\tau\rangle = 4340$ ps. Thus, it is interesting to note, that the triplet nitrene appears to be metastable on intermediate timescales from roughly 20 ps up to a few nanoseconds. As it seems, the formation of the triplet nitrene is therefore only feasible due to inefficient intersystem recrossing that ensures that the system resides sufficiently long on the triplet surface.

Summing up, it was established, that the photochemical reactivity observed by others, results from a series of interconversion between different states. It should be especially pointed out, that the intersystem crossing process is a rather complex transformation from a structural point of view since it involves a change from square planar to pseudotetrahedral geometry and therefore can not occur instantaneously . Once the intersystem process event has taken place, however, the system can be regarded as being trapped on the triplet surface. Only this ultimately enables the formation of the reactive nitrene.

7. Conclusion and Outlook

In the present thesis, the photochemistry and the photophysics of two representatives of the transition metal azido class of compounds have been the subject of detailed investigations. Since the photochemistry of these systems may be rather complex, but still highly relevant both from a practical as well as from a fundamental perspective, here we conducted studies intended to support and enhance the knowledge about the factors that govern the photochemical behavior of such systems. Here, the key to a better understanding lies in knowledge about the ultrafast processes occurring in these systems upon light-matter interaction. Hence, time-resolved pump-probe spectroscopy was applied in this work to obtain insights into the ultrafast dynamics of these systems.

In the first part, a closed-shell octahedral Co(III) low-spin system, *trans*-bis(acetylacetonato)azidopyridinecobalt(III) was investigated. Apart from the involved photophysics, the system was shown to likewise exhibit a pronounced thermal reactivity involving stereochemical scrambling in liquid solution under ambient conditions. The gradual formation of its *cis* isomer was tracked and studied in detail by means of FTIR spectroscopy. Owing to the structure sensitivity of this method, clear changes could be observed in the azide and the carbonyl stretching regions of the spectrum over time, which proved to be highly instructive for monitoring this interconversion. The kinetics of the underlying isomerization could be extracted at temperatures ranging from 20 °C to 58 °C indicating a dramatic acceleration by roughly three orders of magnitudes. Knowledge about the temperature dependence of the reaction rates allowed to determine the activation barrier of the forward reaction to be 122 kJ mol^{-1}.

Mechanistic in-silico DFT studies applied to explore potential reaction mechanisms, indicated that in principle only a sequential pathway is feasible to enable the observed reactivity. The isomerization process commences by an initial pyridine dissociation step. The thus formed five-coordinate intermediate then undergoes a process that can be regarded as an inverse Berry pseudorotation and transfers the vacant coordination site *cis* to the azido ligand. A pursuing pyridine religation then completes the reaction sequence and furnishes the *cis* isomer. Although a certain discrepancy between the theoretically calculated reaction barrier, and the experimental value is found, still the values are sufficiently close to conclude that only this reaction sequence is followed in solution.

Despite the observed tendency for isomerization, it is still interesting to note, that the synthetic route furnishes exclusively the *trans* product. Hence, from a conceptual

perspective, the question about the underlying reaction mechanism for the formation of the starting material arises that, apparently, is sufficiently specific to suppress the formation of detectable amounts of the *cis* isomer and should therefore be investigated in more detail. In addition, this may give some indications how the system may be tuned to suppress the stereochemical isomerization at all. Moreover, possibly a better understanding of the fundamental factors that control this reactivity may be obtained. Especially the fact, that the synthesis had been carried out in an aqueous environment, while all the following studies were conducted in apolar solvents, suggests that this reactivity is at least to some extent solvent controlled, which may be scrutinized further by varying the solvent used in the synthesis, or alternatively for the studies on the isomerization. Thus, following this hypothesis operating in a more polar solvent such as dimethyl sulfoxide or acetonitrile should have an influence on the overall behavior that should be verified experimentally.

Moreover, it appears reasonable to assume, that the isomerization process is sensitive towards exchange or modifications of the departing ligand. Thus, for instance methylation of the pyridine in *ortho* positions most likely should increase steric interaction with the acac ligand and should therefore lead to faster and even more efficient isomerization, not only accelerating the reaction but shifting the chemical equilibrium in general. In fact, as studies by Hsieh and Milosavljević on the *trans*$-\mathrm{Co(acac)(N3)(PPh3)}$ system indicate, the steric demand of the departing ligand indeed leads to a more readily formation of the required fivecoordinate species, as the aforementioned authors even found indications of the presence of small amounts of $\mathrm{Co(acac)2(N3)}$ by NMR when dissolving the starting material in deuterochloroform.[157] As the formation of this intermediate is a clear result of the *trans* influence of the azide ligand exerted on the Co-pyridine σ-bond, it might likewise be of interest to study how the reaction is affected purely by exchanging the pyridine ligand by for instance phosphines or other amines. Alternatively, a more tightly bound ligand (CO) may be utilized to stabilized the system, thereby giving rise to potentially new applications and it should be studied in more detail how this affects the isomerization reaction rates.

However, as was shown, the ligand sphere is not only responsible for the dynamic changes on the timescale of minutes to hours, but in addition, is also essential for the photophysical processes occurring in the system on ultrashort timescales. The ultrafast dynamics were uncovered by femtosecond UV-pump mid-infrared-probe and UV-pump nUV-to-Vis-probe spectroscopy, respectively, and were observed to occur remarkably fast, even on the ultrashort timescale, on the order of only a few tens of picoseconds and were vastly governed by the particular optical properties of the acac and the azide ligands. Thus, excitation at 266 nm was found to prepare the system in the $^1\mathrm{LMCT}_{\mathrm{acac}}$ state which entails formal one-electron oxidation of one of the acac ligands, and, conversely photoreduction and formation of Co(II). This state however was observed to be extremely short-lived and tends to decay into the $^1\mathrm{LMCT}_{\mathrm{azide}}$ state on a

timescale of roughly 200 fs. It could therefore only be identified reliably by probing in the visible range owing to the insufficient temporal resolution of the UV/mIR experiment for this purpose. This process can be regarded as a one-electron transfer from the azide ligand to the coordinated acac radical. It is because of the remarkably fast nature of this process, that no secondary reactivity is encountered involving the acac ligand but instead its integrity is restored fast enough to suppress any such processes. The $^1LMCT_{azide}$ state in turn is considerably longer lived and unequivocally manifests itself in the UV/mIR spectrum by the largely suppressed spectral amplitude of the respective induced absorption band attributed to the asymmetric azide stretching band in the UV/mIR experiment. Over the course of roughly 1.8 ps this state was observed to decay further thereby restoring the integrity of the azide ligand, to either repopulate the ground state directly or via intermediate population of the ^1MC state. Overall, the ground state recovery was found to exhibit a time-scale in the range of 10 ps and essentially occurs quantitatively within the signal-to-noise-ratio of the experimental setup employed here.

As is evident, the photophysical pathway enables efficient repopulation of the ground state, i.e., any putative photochemical process is too slow to compete to a significant extent with the relaxation processes. Thus, this example gives an instructive demonstration how the photochemical stability of a transition metal azido system can be improved; by enabling an efficient relaxation pathway, that channels the population of a potentially reactive state, such as in this case the $^1LMCT_{azide}$ state into a metastable state, such as ^1MC in this case. Alternatively, if photochemical reactivity is instead desired, modifications to the ligand sphere may facilitate photochemical transformations. First of all, in further studies, it would be interesting to explore the efficiency of the decay of the $^1LMCT_{acac}$ state. Hence, control experiments by exchanging the azide ligand by other halogen or pseudohalogen ligands (CN^-, OCN^-, SCN^-, $SeCN^-$) may prove instructive to provide further insight about the question whether the photophysical behavior, that is observed here, can be generalized to related systems. Another option not considered in detail in this work entails variation of the experimental conditions. Thus, in further studies it should be explored whether the outcome of the experiment changes in different solvents, that for instance stabilize a putative azidyl radical or are capable of trapping such species as for instance solvents containing double bonds. This may particularly be of interest in order to explore whether the tendency of the $^1LMCT_{azide}$ state to decay into two isolated radical species may be significantly increased. This process was not observed here but could be a consequence of the molecular surrounding and should not be ruled out in general under different experimental conditions. In addition, tuning the relative energetic ordering of the molecular orbitals may provide another way to explore how the photophysical pathway may be altered by changing the ligand sphere of the system. This unequivocally will affect the efficiency of the coupling between the $^1LMCT_{azide}$ and the ^1MC state, which may therefore be utilized to

adjust the relaxation characteristics of the $^1\mathrm{LMCT}_{\mathrm{azide}}$ state. In particular, utilizing a redox-noninnocent ligand may prove instructive, since in that case the population of charge transfer states involving this ligand can virtually be excluded and thus the photophysics of the azide group of the system can be investigated without any coupling to other electronic states. Summing up, the knowledge inferred from the studies conducted on *trans*-$\mathrm{Co(acac)_2(N_3)(py)}$ proved to be very insightful and may be employed to design systems that enable photophysical and photochemical behavior as desired by experimental chemists.

Having explored the ultrafast photophysics of this system, in addition, the square planar d^8 diazido[1,2-bis(diphenylphosphino)ethane]nickel(II) as a representative of electron-rich complexes of the late transition metals was investigated. Although the atomic number is increased only by one, the electronic configuration and structure were found to be vastly different. Inspired by research by Hennig and coworkers who claimed the involvement of a nitrene species based on indirect measures such as trapping reactions, the hypothesis of these authors was put to a test by studying the ultrafast processes occurring after UV excitation into the $^1\mathrm{LMCT}_{\mathrm{dppe}}$ band at 266 nm by UV-pump mid-infrared spectroscopy. As reports in the literature about the direct spectroscopic observation of nitrene intermediates in the photochemical decomposition of transition metal azides are scarce in general, likewise in this case, so far, bona fide, studies of this type have not been conducted and thus were aimed at developing an understanding about the factors which enable this reactivity.

To this end, a new experimental setup was developed and realized that enabled probing of the response to the UV excitation for pump probe delays spanning several orders of magnitudes ranging from the femto- to the microsecond range based on an approach that combined both optically and electronically delaying the probe pulse with respect to the excitation pulse.

These ultrafast spectroscopic studies indicated the initial population of the $^1\mathrm{LMCT}_{\mathrm{dppe}}$ state which was found to rapidly undergo vibrational cooling with a time constant of 3.5 ps followed by an intersystem crossing event to the triplet manifold that occurs with a time constant of roughly 20 ps. The respective triplet state state preserves the integrity of the two azide vibrators, as was unequivocally demonstrated from the integral ratios of the induced absorption and the ground state bleach, and – based on quantum chemical calculations – was found to adopt a pseudotetrahedral arrangement as is frequently observed for open-shell d^8-systems. On the ultrafast timescale the triplet parent state was found to be metastable, i.e., the systems resides in this state up to several nanoseconds. Hence, the intersystem recrossing process apparently is relatively inefficient and instead with a time constant of 4340 ps dinitrogen is extruded from the system to furnish the triplet nitrene species, which ultimately gives rise to the observed photochemical reactivity. Thus, for the first time the primary processes leading to the formation of the invoked transition metal nitrene species were observed. Following the general trends,

also in this case the triplet nitrene was found to be formed preferably. Still, the formation of the nitrene was found to be remarkably slow in comparison indicative of a high reaction barrier.

The studies indicate, that the process of the nitrene formation is a complex sequence resulting from the interconversion between several states. Since the photochemical reactivity relies on the intermediate population of the triplet state that requires sufficiently high energy, it can therefore selectively be triggered photochemically. Thus, by adjusting the excitation wavelength in further studies, it should be investigated in more detail whether the same photochemical reactivity can also be realized if other electronic states are prepared in the first place. Alternatively, tailoring the ligand sphere may be applied to alter the energetic ordering and coupling between the states which most probably will also directly affect the relaxation pathway and potentially the reaction outcome. Moreover, it would be interesting to prepare nickel d^8-systems that exhibit a triplet ground state already. Following the reasoning discussed before, in these cases the nitrene formation process should then occur even more readily and potentially even thermally. Adjustment to the photochemical reactivity could moreover also be envisioned by adjustment of the ligand sphere in such a way that a potential singlet nitrene is stabilized by introducing a way to lift the degeneracy of the two singly occupied *p*-orbitals of the triplet nitrene.

It should be noted, that owing to the relatively low atomic number in the system studied here the spin-orbit coupling effects are considerably lower than in the heavier congeners of nickel, palladium and platinum. Since the photochemical reactivity apparently is spin controlled, thus extending this work to related systems may give additional insight since the intersystem crossing event should be assumed to be even more efficient in these cases.

Summing up, in the present work, the versatility of time-resolved pump-probe spectroscopy for the investigation of the photochemical and photophysical processes of transition metal azido complexes was demonstrated. A few general trends observed in azide photochemistry were confirmed and understood on a molecular dynamic level and will hence assist experimentalists in the future to develop systems that will meet the exact requirements to fulfill the desired properties. With the present work, the author hopes to raise awareness about this experimental technique. As was illustrated in this thesis, it constitutes a powerful tool to derive a profound understanding about the subtleties that govern the photoreactivity of transition metal complexes and its application in a much broader sense in this field in the future is therefore highly desirable.

8. Bibliography

(1) Cardona, T. *Heliyon* **2018**, *4*, e00548.

(2) Vol'pin, M.; Kolomnikov, I. In *Coordination Chemistry–XIV*; Butterworth-Heinemann: 1973, pp 567–581.

(3) Darensbourg, D. J.; Kudaroski, R. A. In *Advances in Organometallic Chemistry*; Elsevier: 1983; Vol. 22, pp 129–168.

(4) Yin, X.; Moss, J. R. *Coord. Chem. Rev.* **1999**, *181*, 27–59.

(5) Ciamician, G. *Science* **1912**, *36*, 385–394.

(6) Friedlingstein, P. et al. *Earth Syst. Sci. Data* **2020**, *12*, 3269–3340.

(7) Fujita, E. *Coord. Chem. Rev.* **1999**, *185-186*, 373–384.

(8) Raymond, J.; Blankenship, R. E. *Coord. Chem. Rev.* **2008**, *252*, The Role of Manganese in Photosystem II, 377–383.

(9) Lehn, J.-M.; Ziessel, R. *Proceedings of the National Academy of Sciences* **1982**, *79*, 701–704.

(10) Artero, V.; Chavarot-Kerlidou, M.; Fontecave, M. *Angew. Chem. Int. Ed.* **2011**, *50*, 7238–7266.

(11) Sutra, P.; Igau, A. *Current Opinion in Green and Sustainable Chemistry* **2018**, *10*, Green Catalysis, 60–67.

(12) Nocera, D. G. *Acc. Chem. Res.* **2012**, *45*, 767–776.

(13) Porter, G.-N. *Proceedings of the Royal Society of London. Series A. Mathematical and Physical Sciences* **1950**, *200*, 284–300.

(14) Porter, G.; Wright, F. J. *Discuss. Faraday Soc.* **1953**, *14*, 23–34.

(15) Ertl, G. *Angew. Chem. Int. Ed. Engl.* **1990**, *29*, 1219–1227.

(16) Ertl, G. *Chem. Rec.* **2001**, *1*, 33–45.

(17) Torres-Alacan, J.; Krahe, O.; Filippou, A. C.; Neese, F.; Schwarzer, D.; Vöhringer, P. *Chem. Eur. J.* **2012**, *18*, 3043–3055.

(18) Torres-Alacan, J.; Das, U.; Filippou, A. C.; Vöhringer, P. *Angew. Chem., Int. Ed.* **2013**, *52*, 12833–12837.

(19) Torres-Alacan, J.; Vöhringer, P. *Int. Rev. Phys. Chem.* **2014**, *33*, 521–553.

(20) Torres-Alacan, J.; Lindner, J.; Vöhringer, P. *ChemPhysChem* **2015**, *16*, 2289–2293.

(21) Torres-Alacan, J.; Vöhringer, P. *Chem. Eur. J.* **2017**, *23*, 6746–6751.

(22) Vennekate, H.; Schwarzer, D.; Torres-Alacan, J.; Krahe, O.; Filippou, A. C.; Neese, F.; Vöhringer, P. *Phys. Chem. Chem. Phys.* **2012**, *14*, 6165–6172.

(23) Vennekate, H.; Schwarzer, D.; Torres-Alacan, J.; Vöhringer, P. *J. Am. Chem. Soc.* **2014**, *136*, 10095–10103.

(24) Meunier, B.; de Visser, S. P.; Shaik, S. *Chem. Rev.* **2004**, *104*, 3947–3980.

(25) Han, A.-R.; Jin Jeong, Y.; Kang, Y.; Yoon Lee, J.; Sook Seo, M.; Nam, W. *Chem. Commun.* **2008**, 1076–1078.

(26) Makris, T. M.; von Koenig, K.; Schlichting, I.; Sligar, S. G. *J. Inorg. Biochem.* **2006**, *100*, High-valent iron intermediates in biology, 507–518.

(27) Hennig, H.; Hofbauer, K.; Handke, K.; Stich, R. *Angew. Chem. Int. Ed. Engl.* **1997**, *36*, 408–410.

(28) Hennig, H.; Ritter, K.; Chibisov, A. K.; Görner, H.; Grevels, F.-W.; Kerpen, K.; Schaffner, K. *Inorg. Chim. Acta* **1998**, *271*, 160–166.

(29) Kurz, D.; Hennig, H.; Reinhold, J. *Z. Anorg. Allg. Chem.* **2000**, *626*, 354–361.

(30) Holleman, A. F.; Wiberg, E.; Wiberg, N., *Anorganische Chemie: Nebengruppenelemente, Lanthanoide, Actinoide, Transactinoide, Anhänge*, 103rd Edition; De Gruyter: 2017; Vol. 2.

(31) Pauling, L. *J. Am. Chem. Soc.* **1931**, *53*, 1367–1400.

(32) Pauling, L. *J. Am. Chem. Soc.* **1931**, *53*, 3225–3237.

(33) Pauling, L., *The Nature of the Chemical Bond and the Structure of Molecules and Crystals: An Introduction to Modern Structural Chemistry*, 3rd ed.; George Fisher Baker Non-Resident Lec; Cornell University Press: 1960.

(34) Gillespie, R. J.; Robinson, E. A. *Chem. Soc. Rev.* **2005**, *34*, 396–407.

(35) Ahlrichs, R. *Chem. unserer Zeit* **1980**, *14*, 18–24.

(36) Müller, U. In *Inorganic Chemistry*; Springer: 1973, pp 141–172.

(37) Dori, Z.; Ziolo, R. F. *Chem. Rev.* **1973**, *73*, 247–254.

(38) Finch, A.; Gardner, P.; Head, A.; Xiaoping, W. *J. Chem. Thermodyn.* **1990**, *22*, 301–305.

(39) Portius, P.; Davis, M. *Coord. Chem. Rev.* **2013**, *257*, Recent Developments in Main Group Chemistry, 1011–1025.

(40) Evers, J.; Göbel, M.; Krumm, B.; Martin, F.; Medvedyev, S.; Oehlinger, G.; Steemann, F. X.; Troyan, I.; Klapötke, T. M.; Eremets, M. I. *J. Am. Chem. Soc.* **2011**, *133*, 12100–12105.

(41) Tornieporth-Oetting, I. C.; Klapötke, T. M. *Angew. Chem. Int. Ed. Engl.* **1995**, *34*, 511–520.

(42) Ziolo, R. F.; Dori, Z. *J. Am. Chem. Soc.* **1968**, *90*, 6560–6561.

(43) *Proc. Chem. Soc.* **1961**, 357–396.

(44) Kolb, H. C.; Finn, M. G.; Sharpless, K. B. *Angew. Chem. Int. Ed.* **2001**, *40*, 2004–2021.

(45) Hawker, C. J.; Fokin, V. V.; Finn, M.; Sharpless, K. B. *Aust. J. Chem* **2007**, *60*, 381–383.

(46) Evans, R. A. *Aust. J. Chem.* **2007**, *60*, 384–395.

(47) Himo, F.; Lovell, T.; Hilgraf, R.; Rostovtsev, V. V.; Noodleman, L.; Sharpless, K. B.; Fokin, V. V. *J. Am. Chem. Soc.* **2005**, *127*, 210–216.

(48) Rostovtsev, V. V.; Green, L. G.; Fokin, V. V.; Sharpless, K. B. *Angewandte Chemie* **2002**, *114*, 2708–2711.

(49) Evans, B. L.; Yoffe, A. D.; Bowden, F. P. *Proceedings of the Royal Society of London. Series A. Mathematical and Physical Sciences* **1957**, *238*, 568–574.

(50) Evans, B.; Yoffe, A.; Gray, P. *Chem. Rev.* **1959**, *59*, 515–568.

(51) Evans, B. L.; Yoffe, A. D.; Bowden, F. P. *Proceedings of the Royal Society of London. Series A. Mathematical and Physical Sciences* **1959**, *250*, 346–366.

(52) Krischner, H. *Monatshefte für Chemie / Chemical Monthly* **1985**, *116*, 189–202.

(53) Seok, W.-K.; Klapötke, T. M. *Bull. Korean Chem. Soc.* **2010**, *31*, 781–788.

(54) Janoschek, R. *Angew. Chem. Int. Ed. Engl.* **1993**, *32*, 230–232.

(55) Holleman, A. F.; Wiberg, E.; Wiberg, N., *Anorganische Chemie: Grundlagen und Hauptgruppenelemente*, 103rd Edition; De Gruyter: 2017; Vol. 1.

(56) Fehlhammer, W. P.; Beck, W. *Z. Anorg. Allg. Chem.* **2013**, *639*, 1053–1082.

(57) Schulz, A.; Tornieporth-Oetting, I. C.; Klapoetke, T. M. *Inorg. Chem.* **1995**, *34*, 4343–4346.

(58) Šima, J. *Coord. Chem. Rev.* **2006**, *250*, 20th International Conference on Coordination and Bioinorganic Chemistry, 2325–2334.

(59) Flesch, S.; Domenianni, L. I.; Vöhringer, P. *Phys. Chem. Chem. Phys.* **2020**, *22*, 25618–25630.

(60) Becalska, A.; Batchelor, R.; Einstein, F.; Hill, R. H.; Palmer, B. *Inorg. Chem.* **1992**, *31*, 3118–3123.

(61) Gafney, H. D.; Reed, J. L.; Basolo, F. *J. Am. Chem. Soc.* **1973**, *95*, 7998–8005.

(62) Vogler, A.; Wright, R. E.; Kunkely, H. *Angew. Chem. Int. Ed. Engl.* **1980**, *19*, 717–718.

(63) Lauderdale, W. J.; Stanton, J. F.; Bartlett, R. J. *J. Phys. Chem.* **1992**, *96*, 1173–1178.

(64) Kalyanasundaram, K; Grätzel, M., *Photosensitization and Photocatalysis using inorganic and organometallic compounds*; Springer Science & Business Media: 1993; Vol. 14.

(65) Rehorek, D; Thomas, P.; Hennig, H *Inorg. Chim. Acta* **1979**, *32*, L1–L2.

(66) Ferraudi, G.; Endicott, J. F. *J. Am. Chem. Soc.* **1973**, *95*, 2371–2372.

(67) Ferraudi, G.; Endicott, J. F. *Inorg. Chem.* **1973**, *12*, 2389–2396.

(68) Endicott, J. F.; Hoffman, M. Z.; Beres, L. S. *J. Phys. Chem.* **1970**, *74*, 1021–1029.

(69) Reed, J. L. *Inorg. Chem.* **1978**, *17*, 1725–1729.

(70) Reed, J. L. *Inorg. Chem.* **1982**, *21*, 2829–2832.

(71) Kurti, L.; Czakó, B., *Strategic Applications of Named Reactions in Organic Synthesis*, First Edition; Elsevier Academic Press: Amsterdam, 2005.

(72) Falvey, D. E.; Gudmundsdottir, A. D., *Nitrenes and Nitrenium Ions*; Wiley Hoboken, NJ: 2013; Vol. 6.

(73) Richardson, W. C.; Setser, D. W. *Can. J. Chem.* **1969**, *47*, 2725–2727.

(74) Alexander, M. H.; Werner, H.; Dagdigian, P. J. *J. Chem. Phys.* **1988**, *89*, 1388–1400.

(75) Reed, J. L.; Wang, F.; Basolo, F. *J. Am. Chem. Soc.* **1972**, *94*, 7173–7174.

(76) Kane-Maguire, L. A.; Sheridan, P. S.; Basolo, F.; Pearson, R. G. *J. Am. Chem. Soc.* **1970**, *92*, 5865–5872.

(77) Lane, B. C.; McDonald, J. W.; Basolo, F.; Pearson, R. G. *J. Am. Chem. Soc.* **1972**, *94*, 3786–3793.

(78) Vreeken, V.; Siegler, M. A.; de Bruin, B.; Reek, J. N. H.; Lutz, M.; van der Vlugt, J. I. *Angew. Chem. Int. Ed.* **2015**, *54*, 7055–7059.

(79) Klein, H. F.; Haller, S.; Koenig, H.; Dartiguenave, M.; Dartiguenave, Y.; Menu, M. J. *J. Am. Chem. Soc.* **1991**, *113*, 4673–4675.

(80) Ngai, R.; Wang, Y. H. L.; Reed, J. L. *Inorg. Chem.* **1985**, *24*, 3802–3807.

(81) Chatt, J.; Falk, C. D.; Leigh, G. J.; Paske, R. J. *J. Chem. Soc. A* **1969**, 2288–2293.

(82) Berry, J. F. *Comments Inorg. Chem.* **2009**, *30*, 28–66.

(83) Arshankow, S. I.; Poznjak, A. L. *Z. Anorg. Allg. Chem.* **1981**, *481*, 201–206.

(84) Poznyak, A. L.; Pavlovski, V. I. *Angew. Chem. Int. Ed. Engl.* **1988**, *27*, 789–796.

(85) Corcos, A. R.; Long, A. K. M.; Guzei, I. A.; Berry, J. F. *Eur. J. Inorg. Chem.* **2013**, *2013*, 3808–3811.

(86) Tsubaki, M.; Hori, H.; Hotta, T.; Hiwatashi, A.; Ichikawa, Y.; Yu, N. T. *Biochemistry* **1987**, *26*, 4980–4986.

(87) Tran, B. L.; Washington, M. P.; Henckel, D. A.; Gao, X.; Park, H.; Pink, M.; Mindiola, D. J. *Chem. Commun.* **2012**, *48*, 1529–1531.

(88) Hesse, M.; Meier, H.; Zeeh, B., *Spektroskopische Methoden in der Organischen Chemie*, Eighth Edition; Thieme: 2012.

(89) Banwell, C. N.; McCash, E. M., *Fundamentals of Molecular Spectroscopy*; McGraw-Hill New York: 1994; Vol. 851.

(90) Hollas, J. M., *Modern Spectroscopy*; John Wiley & Sons: 2004.

(91) Atkins, P.; de Paula, J., *Physical Chemistry*, Ninth Edition; Oxford University Press: 2009.

(92) Eigen, M. *Discuss. Faraday Soc.* **1954**, *17*, 194–205.

(93) Eigen, M.; Johnson, J. S. *Annu. Rev. Phys. Chem.* **1960**, *11*, 307–334.

(94) Cavalieri, A. L.; Müller, N.; Uphues, T.; Yakovlev, V. S.; Baltuška, A.; Horvath, B.; Schmidt, B; Blümel, L; Holzwarth, R; Hendel, S., et al. *Nature* **2007**, *449*, 1029–1032.

(95) Jordan, I.; Huppert, M.; Rattenbacher, D.; Peper, M.; Jelovina, D.; Perry, C.; von Conta, A.; Schild, A.; Wörner, H. J. *Science* **2020**, *369*, 974–979.

(96) Ramasesha, K.; Leone, S. R.; Neumark, D. M. *Annu. Rev. Phys. Chem.* **2016**, *67*, 41–63.

(97) Khundkar, L. R.; Zewail, A. H. *Annu. Rev. Phys. Chem.* **1990**, *41*, 15–60.

(98) Mukamel, S. *Annu. Rev. Phys. Chem.* **1990**, *41*, 647–681.

(99) Born, M.; Oppenheimer, R. *Ann. Phys.* **1927**, *389*, 457–484.

(100) Schoonover, J. R.; Strouse, G. F. *Chem. Rev.* **1998**, *98*, 1335–1356.

(101) Franck, J.; Dymond, E. G. *Trans. Faraday Soc.* **1926**, *21*, 536–542.

(102) Condon, E. *Phys. Rev.* **1926**, *28*, 1182–1201.

(103) Condon, E. U. *Phys. Rev.* **1928**, *32*, 858–872.

(104) Einstein, A. *Phys. Z.* **1917**, *18*, 121–128.

(105) Straub, S.; Brünker, P.; Lindner, J.; Vöhringer, P. *Phys. Chem. Chem. Phys.* **2018**, *20*, 21390–21403.

(106) Straub, S.; Stubbe, J.; Lindner, J.; Sarkar, B.; Vöhringer, P. *Inorg. Chem.* **2020**, *59*, 14629–14642.

(107) Omary, M. A.; Patterson, H. H. In *Encyclopedia of Spectroscopy and Spectrometry (Third Edition)*, Lindon, J. C., Tranter, G. E., Koppenaal, D. W., Eds., Third Edition; Academic Press: Oxford, 2017, pp 636–653.

(108) Jörn Manz, L. W., *Femtosecond Chemistry: A Handbook in Two Volumes*, 1st ed.; Wiley-VCH: 1995.

(109) Ruckebusch, C.; Sliwa, M.; Pernot, P.; de Juan, A.; Tauler, R. *J. Photochem. Photobiol., C* **2012**, *13*, 1–27.

(110) Rullière, C., *Femtosecond Laser Pulses*, 2nd Edition; Advanced Texts in Physics; Springer: 2005.

(111) Siegman, A. E., *Lasers*; University Science Books: 1986.

(112) Weiner, A., *Ultrafast Optics*; John Wiley & Sons: 2011; Vol. 72.

(113) Wezisla, B.; Lindner, J.; Das, U.; Filippou, A. C.; Vöhringer, P. *Angew. Chem., Int. Ed.* **2017**, *56*, 6901–6905.

(114) Straub, S.; Lindner, J.; Vöhringer, P. *J. Phys. Chem. A* **2017**, *121*, 4914–4922.

(115) Straub, S.; Brünker, P.; Lindner, J.; Vöhringer, P. *Angew. Chem.* **2018**, *130*, 5094–5099.

(116) Juban, E. A.; McCusker, J. K. *J. Am. Chem. Soc.* **2005**, *127*, 6857–6865.

(117) Unruh, T.; Vöhringer, P. *Z. Phys. Chem.* **2020**, *234*, 1549–1566.

(118) Unruh, T.; Domenianni, L. I.; Vöhringer, P. *Mol. Phys.* **2021**, *119*, e1964043.

(119) Boucher, L. J.; Herrington, D. R. *Inorg. Chem.* **1972**, *11*, 1772–1777.

(120) Nakamoto, K., *Infrared and Raman Spectra of Inorganic and Coordination Compounds, Part B, Applications in Coordination, Organometallic, and Bioinorganic Chemistry*, Sixth Edition; Wiley-Blackwell: Chichester, 2009.

(121) Martin, R. L. *J. Chem. Phys.* **2003**, *118*, 4775–4777.

(122) Gade, L. H., *Koordinationschemie*, First Edition; Wiley-VCH: Weinheim, 1998.

(123) Miessler, G. L.; Fischer, P. J.; Tarr, D. A., *Inorganic Chemistry*, Fifth Edition; Pearson: Boston, 2013.

(124) Laporte, O.; Meggers, W. F. *J. Opt. Soc. Am.* **1925**, *11*, 459–463.

(125) Domenianni, L. I.; Fligg, R.; Schäfermeier, A.; Straub, S.; Beerhues, J.; Sarkar, B.; Vöhringer, P. *Phys. Chem. Chem. Phys.* **2019**, *21*, 20393–20402.

(126) Herrington, D. R.; Boucher, L. J. *Inorg. Chem.* **1973**, *12*, 2378–2381.

(127) McNaught, A. D.; Wilkinson, A., et al., *Compendium of Chemical Terminology*; Blackwell Science Oxford: 1997; Vol. 1669.

(128) Wedler, G.; Freund, H.-J., *Lehrbuch der Physikalischen Chemie*; John Wiley & Sons: 2012; Vol. 1.

(129) Levine, I., *Physical Chemistry*, 6th edition; McGraw-Hill: 2008.

(130) Muetterties, E. L. *J. Am. Chem. Soc.* **1968**, *90*, 5097–5102.

(131) Brady, J. E. *Inorg. Chem.* **1969**, *8*, 1208–1209.

(132) Rodger, A.; Johnson, B. F. *Inorg Chem* **1988**, *27*, 3061–3062.

(133) Darensbourg, D. J. In *Advances in Organometallic Chemistry*, Stone, F., West, R., Eds.; Advances in Organometallic Chemistry, Vol. 21; Academic Press: 1982, pp 113 –150.

(134) Darensbourg, D. J.; Kudaroski, R.; Schenk, W. *Inorg. Chem.* **1982**, *21*, 2488–2491.

(135) Crabtree, R. H., *The Organometallic Chemistry of the Transition Metals*, Sixth Edition; Wiley: Hoboken, 2014.

(136) Hartwig, J., *Organotransition Metal Chemistry: From Bonding to Catalysis*, First Edition; University Science Books: Mill Valley, 2009.

(137) Berry, R. S. *J. Chem. Phys.* **1960**, *32*, 933–938.

(138) Cass, M. E.; Hiib, K.; Rzepa, H. S. *J. Chem. Educ.* **2006**, *83*, 336.

(139) Iron, M. A.; Janes, T. *J. Phys. Chem. A* **2019**, *123*, 3761–3781.

(140) Hu, L.; Chen, H. *J. Chem. Theory Comput.* **2015**, *11*, 4601–4614.

(141) Sando, G. M.; Zhong, Q.; Owrutsky, J. C. *J. Chem. Phys.* **2004**, *121*, 2158–2168.

(142) Hamm, P.; Ohline, S. M.; Zinth, W. *J. Chem. Phys.* **1997**, *106*, 519–529.

(143) Straub, S.; Domenianni, L. I.; Lindner, J.; Vöhringer, P. *J. Phys. Chem. B* **2019**, *123*, 7893–7904.

(144) Bowman, K.; Dori, Z. *Inorg. Chem.* **1970**, *9*, 395–397.

(145) Thananatthanachon, T.; Lecklider, M. R. *J. Chem. Educ.* **2017**, *94*, 786–789.

(146) Uhlig, E. *Coord. Chem. Rev.* **1973**, *10*, 227–264.

(147) Venanzi, L. *J. Chem. Soc.* **1958**, 719–724.

(148) Coussmaker, C.; Hutchinson, M. H.; Mellor, J.; Sutton, L.; Venanzi, L. *J. Chem. Soc.* **1961**, 2705–2713.

(149) Browning, M.; Davies, R.; Morgan, D.; Sutton, L.; Venanzi, L. *J. Chem. Soc.* **1961**, 4816–4823.

(150) Browning, M.; Mellor, J.; Morgan, D.; Pratt, S.; Sutton, L.; Venanzi, L. *J. Chem. Soc.* **1962**, 693–703.

(151) Van Leeuwen, P. W. N. M.; Kamer, P. C. J.; Reek, J. N. H. *Pure Appl. Chem.* **1999**, *71*, 1443–1452.

(152) Muthu Tamizh, M.; Mereiter, K.; Kirchner, K.; Ramachandra Bhat, B.; Karvembu, R. *Polyhedron* **2009**, *28*, 2157–2164.

(153) Gao, W.; Li, K.; Wang, X.-L. *Asian J. Chem.* **2013**, *25*, 7876.

(154) Smith, J. M.; Subedi, D. *Dalton Trans.* **2012**, *41*, 1423–1429.

(155) Scepaniak, J. J.; Fulton, M. D.; Bontchev, R. P.; Duesler, E. N.; Kirk, M. L.; Smith, J. M. *J. Am. Chem. Soc.* **2008**, *130*, 10515–10517.

(156) Scepaniak, J. J.; Vogel, C. S.; Khusniyarov, M. M.; Heinemann, F. W.; Meyer, K.; Smith, J. M. *Science* **2011**, *331*, 1049–1052.

(157) Hsieh, B.-T.; Nelson, J. H.; Milosavljević, E. B.; Beck, W.; Kemmerich, T. *Inorg. Chim. Acta* **1987**, *133*, 267 –274.

A. Glossary

Table A.1.: *List of acronyms used throughout this thesis.*

acronym	meaning
[1]	bis(acetylacetonato)azidopyridinecobalt(III)
[2]	diazido[1,2-bis(diphenylphosphino)ethane]nickel(II)
acac	acetylacetonato
BBO	β-barium borate
CASSCF	complete active space self-consistent field
DFT	density functional theory
dppe	1,2-bis(diphenyl)phosphinoethane
EDC	1,2-dichloroethane
EPR	electron paramagnetic resonance
FTIR spectroscopy	Fourier transform infrared spectroscopy
FWHM	full width at half maximum
GSB	ground state bleach
IA	induced absorption
IR	infrared
ISC	intersystem crossing
IVR	intramolecular vibrational energy redistribution
LC state	ligand centered state
LF state	ligand field state
LMCT	ligand-to-metal charge transfer
MC state	metal centered state
MCT	mercury cadmium telluride
mIR	mid-infrared
MLCT	metal-to-ligand charge transfer
NEVPT	n-electron valence state perturbation theory
NIR	near-infrared
NMR	nuclear magnetic resonance
OD	optical density
OPA	optical parametrical amplifier
PES	potential energy surface
py	pyridine

Table A.2.: *List of acronyms used throughout this thesis (continued).*

acronym	meaning
RGA	regenerative amplifier
THG	third harmonic generation
TDDFT	time-dependent density functional theory
UV	ultraviolet
UV/mIR	ultraviolet-pump mid-infrared-probe
UV/nUV-to-Vis	ultraviolet-pump near-ultraviolet-to-visible-probe
VER	vibrational energy relaxation
Vis	visible
VSEPR	valence shell electron pair repulsion

B. List of Chemicals

Table B.1.: *List of chemicals used for syntheses and studies of target materials in this thesis.*

compound	sum formula	supplier	purity
bis(acetylacetonato)azidopyridinecobalt(III)	$CoC_{10}H_{14}O_4$	Alfa Aesar	$\geq 97\,\%$
sodium azide	NaN_3	Roth	$\geq 99\,\%$
hydrogen peroxide (aqueous solution)	H_2O_2	Merck	35 %
acetic acid	$C_2H_4O_2$	VWR	99.8 %
nickel(II)dichloride	$NiCl_2$	Alfa Aesar	98 %
1,2-bis(diphenyl)phosphinoethane	$C_{26}H_{24}P_2$	abcr	97 %
dichloromethane	CH_2Cl_2	VWR	99.9 %
1,2-dichloroethane	$C_2H_4Cl_2$	VWR	99.9 %

C. Theoretical Calculations

C.1. $Co(acac)_2(N_3)(py)$

C.1.1. trans−$Co(acac)_2(N_3)(py)$

Geometry Optimization

```
! def2-TZVP def2/J RIJCOSX D3BJ TightSCF TightOpt Freq defgrid3
! MORead
%moinp "old_orbitals.gbw"

%pal
nprocs 8
end

%maxcore 3000

%method
method dft
functional HYB_MGGA_XC_MPW1B95
end

%method
D3S6 1.000
D3A1 0.1955
D3S8 1.0508
D3A2 6.4177
end

%scf
MaxIter 100
end

%cpcm
epsilon 10.36
```

```
end

* xyzfile 0 1 start.xyz
```

Optimized Geometry

```
43
Coordinates from ORCA-job tr_opt_freq_C1
  C   -1.79070700480069      1.72871264090918      3.26629507900670
  C   -1.04724428421314      0.69541831892745      2.48846050609874
  H   -2.78392858924662      1.84387836633550      2.83488326838996
  H   -1.28182896575369      2.68603372296619      3.17149231411349
  H   -1.87807175145633      1.46430646047009      4.31394864697280
  C   -0.59021702633804     -0.45254966825162      3.12253250100381
  C   0.18307186605280     -1.42744470761828      2.49871083844359
  C   0.72055475451824     -2.56584765684696      3.30029694347936
  H   0.43990944171319     -2.49521378677206      4.34502241181061
  H   1.80539817381037     -2.58331920798457      3.21437668938453
  H   0.34662985003829     -3.49984460592397      2.88466350621298
  C   -1.79070726332450      1.72871272136247     -3.26629457717261
  C   -1.04724445926536      0.69541842981864     -2.48845998376784
  H   -1.87807206966238      1.46430648615795     -4.31394814095147
  H   -2.78392882814842      1.84387843560780     -2.83488274652817
  H   -1.28182923969381      2.68603380977734     -3.17149192029398
  C   -0.59021712827224     -0.45254948570976     -3.12253206755114
  C   0.18307174445178     -1.42744456609604     -2.49871045534207
  C   0.72055463284926     -2.56584743867810     -3.30029673700977
  H   0.34662983348079     -3.49984443279645     -2.88466334490024
  H   1.80539806877894     -2.58331892803671     -3.21437669024545
  H   0.43990918090607     -2.49521349137437     -4.34502217146515
  O   -0.88233227701699      0.96857265739722      1.26368291133361
  O   0.49843830998594     -1.43808610760160      1.27629893575651
  O   0.49843815676921     -1.43808603798789     -1.27629853341144
  O   -0.88233238156698      0.96857270099565     -1.26368236121933
  H   -0.79444133241907     -0.56497456429160      4.17329884738238
  Co  -0.19519319731056     -0.23906183176344      0.00000033046026
  H   -0.79444140721995     -0.56497430533495     -4.17329843610852
  N   -1.86385312984144     -1.23124548112175      0.00000017241374
  N   -2.85630059826933     -0.57405411113884      0.00000078182048
  N   -3.83114134983693      0.01691208473472     -0.00000506402407
  N   1.50794738188076      0.71675285826044      0.00000017753757
  C   2.64987474500454      0.03839652101462      0.00000022210646
  C   1.52309126922591      2.04479408336971     -0.00000014062652
  C   3.87020027026361      0.67763841310141     -0.00000010317053
  C   2.70410064764228      2.75399610281480     -0.00000040166723
```

C	3.89834925495759	2.05907963006256	-0.00000024722263
H	2.67934230203799	3.83190910619866	-0.00000073779195
H	4.83973846147929	2.58761571622259	-0.00000038490016
H	4.77765275913037	0.09535286341490	-0.00000001914004
H	2.55910792083043	-1.03577406319270	0.00000053896444
H	0.55871622453015	2.52679551589652	-0.00000035818170

TDDFT Calculation

```
! def2-TZVPP def2/J RIJCOSX TightSCF defgrid3
! MORead
%moinp "orbitals.gbw"

%tddft
nroots 50
DoNTO true
triplets True
end

%pal
nprocs 8
end

%maxcore 3000

%method
method dft
functional HYB_GGA_XC_WB97X_D
end

%scf
MaxIter 100
end

%cpcm
epsilon 8.93
end

* xyzfile 0 1 wB97-XD_opt_geometry.xyz
```

C.1.2. cis−$Co(acac)_2(N_3)(py)$

Geometry Optimization

```
! Usesym def2-TZVP def2/J RIJCOSX D3BJ TightSCF TightOpt Freq defgrid3

%maxcore 2000

%pal
nprocs 8
end

%method
method dft
functional HYB_MGGA_XC_MPW1B95
end

%method
D3S6 1.000
D3A1 0.1955
D3S8 1.0508
D3A2 6.4177
end

%scf
MaxIter 100
end

%method
SymThresh 5.0e-2
end

%cpcm
epsilon 10.36
end

* xyzfile 0 1 start.xyz
```

Optimized Geometry

```
43
Coordinates from ORCA-job c_opt_freq
  O   -1.49835703324068     -0.72727491707392     -0.70418777666262
  O    1.77195085699524      0.76676723708112      0.39436696422493
  O    0.83389998989212     -1.75970427072787     -0.31732766323176
  C    2.89271279614846      0.19192203152426      0.30440120544182
  C    4.06737136057223      1.04240889748126      0.65868881039218
  C    3.09432917904863     -1.13101400188957     -0.07591103831390
  C    2.06802079726854     -2.03257668102322     -0.33381697584312
  C    2.39213431871692     -3.45204640537879     -0.66029661373508
  H    4.08975570050361      1.90946389487676      0.00106262956792
  H    3.94893186592364      1.40892186519072      1.67671137146732
  H    4.10677493446112     -1.49380356063173     -0.11974485957200
  H    2.02554870845882     -3.67075490994443     -1.66231813613553
  H    1.86709266829140     -4.10993498121924      0.02920650119727
  H    3.45727616728846     -3.64820004812420     -0.61355943303064
  Co   0.14395957109382     -0.02477024920507     -0.12130978184795
  O   -0.15627194345618     -0.36798555903833      1.71775427817201
  N    0.57708273483112      0.38407776906908     -1.96544490266992
  N    0.36403786576004     -0.48766117526000     -2.74818122453764
  N    0.17799013859042     -1.29309456641762     -3.53198589054559
  H    5.00193728905974      0.49937649146837      0.57563214642209
  C   -2.27329928011078     -1.41440549507104      0.02113499435767
  C   -2.11038001078249     -1.64753048049134      1.38180582179556
  C   -1.08910385499523     -1.10082364970162      2.15242671310544
  C   -1.05439314633871     -1.36448525107242      3.62128045940148
  C   -3.45433782693107     -1.98508216377140     -0.69024355479128
  H   -0.12513715765030     -1.87556565420512      3.86734082108172
  H   -1.89533347345410     -1.96661131798588      3.94614220459162
  H   -1.05509228866924     -0.41663021612995      4.15596154011367
  H   -2.84598899506906     -2.25588520316374      1.87917497692576
  H   -3.10813987033289     -2.58911699489609     -1.52667817440515
  H   -4.04860837355642     -1.17103540547299     -1.10204863470989
  H   -4.07258366311910     -2.58744393164136     -0.03444574168170
  N   -0.68675618029121      1.71778070616893      0.07153415535163
  C   -0.42160519401869      2.46189084413674      1.13964389171665
  C   -1.00483743662337      3.69601546716154      1.32525859924662
  C   -1.88856878693093      4.16552106114197      0.37284224061817
  C   -2.15741153738832      3.38322079381145     -0.73379375910611
```

C	-1.53413562627543	2.16062569292394	-0.85109475982900
H	0.27368789894208	2.04056460066510	1.84678374332498
H	-0.76549742120251	4.27162156215142	2.20495862901646
H	-2.36200050393664	5.12850923086306	0.49158286377075
H	-2.84010882506838	3.70885922505745	-1.50210934113814
H	-1.70010186617932	1.50594841326385	-1.69069557328686

C.1.3. trans−Co(acac)$_2$(N$_3$)

Geometry Optimization

```
! Usesym def2-TZVP def2/J RIJCOSX D3BJ TightSCF TightOpt Freq defgrid3

%pal
nprocs 4
end

%maxcore 3000

%method
method dft
functional HYB_MGGA_XC_MPW1B95
end

%method
D3S6 1.000
D3A1 0.1955
D3S8 1.0508
D3A2 6.4177
end

%scf
MaxIter 100
end

%sym
SymThresh 5.0e-2
end

%cpcm
epsilon 10.36
end

* xyzfile 0 1 start.xyz
```

Optimized Geometry

```
32
Coordinates from ORCA-job tr-Co_--py
  C   -1.08830786702189      2.08490562149711      3.26389444924728
  C   -0.35091122494867      1.04463904529453      2.49542976517687
  H   -2.07997910707603      2.20388325496014      2.82994725568581
  H   -0.57281178799824      3.03812055076200      3.16322059835127
  H   -1.17684828740623      1.82688924986392      4.31289318894950
  C   0.11459717354582     -0.09848291707666      3.12787807592446
  C   0.94490386829706     -1.01878356830405      2.49871514778103
  C   1.55935508075441     -2.12944216664807      3.27810739409697
  H   1.31598732365714     -2.06832227973756      4.33256745948815
  H   2.63932968354499     -2.10656717232050      3.14767807184368
  H   1.20430154954484     -3.07756030430916      2.87688343427999
  C   -1.08830780506264      2.08490567518166     -3.26389439933101
  C   -0.35091127345991      1.04463900884992     -2.49542972557115
  H   -1.17684824555032      1.82688934117342     -4.31289314334577
  H   -2.07997903348560      2.20388343594458     -2.82994721369505
  H   -0.57281159245508      3.03812052914722     -3.16322053360112
  C   0.11459702376831     -0.09848300285603     -3.12787799106298
  C   0.94490374000901     -1.01878364655688     -2.49871505023898
  C   1.55935495120786     -2.12944218139482     -3.27810737637760
  H   1.20430149804552     -3.07756035961602     -2.87688345274499
  H   2.63932957516513     -2.10656714928058     -3.14767818152908
  H   1.31598709340893     -2.06832223438480     -4.33256741793343
  O   -0.18319367716293      1.30586855405533      1.26289634492051
  O   1.25326992616575     -0.98415184730351      1.27000752470732
  O   1.25326986256740     -0.98415191856720     -1.27000741569531
  O   -0.18319364375585      1.30586853860411     -1.26289632905583
  H   -0.09174071564525     -0.22526089238680      4.17645761159990
  Co  0.42635695251891      0.09406657777456      0.00000005676324
  H   -0.09174086197811     -0.22526098350305     -4.17645753415162
  N   -1.14152135468863     -0.90649114885157      0.00000026808997
  N   -2.15171940673358     -0.25252264441101      0.00000001410247
  N   -3.14629950874507      0.28805958127057     -0.00000089667452
```

C.1.4. cis−Co(acac)$_2$(N$_3$)

Geometry Optimization

```
! Usesym def2-TZVP def2/J RIJCOSX D3BJ TightSCF TightOpt Freq defgrid3

%maxcore 2000

%pal
nprocs 8
end

%method
method dft
functional HYB_MGGA_XC_MPW1B95
end

%method
D3S6 1.000
D3A1 0.1955
D3S8 1.0508
D3A2 6.4177
end

%scf
MaxIter 100
end

%method
SymThresh 5.0e-2
end

%cpcm
epsilon 10.36
end

* xyzfile 0 1 start.xyz
```

Optimized Geometry

```
32
Coordinates from ORCA-job c_opt_freq
  O   -1.79632544973394      0.01696723076304     -0.62454898986105
  O    1.43749168540599      1.44361153596821      0.44857814138134
  O    0.56346654903070     -1.08640810282307     -0.24584414543206
  C    2.58265013261759      0.92613695540025      0.36550550568604
  C    3.72459142280661      1.81832235708544      0.70698770328012
  C    2.81810399040474     -0.40076362173176     -0.00121935319973
  C    1.81810610886377     -1.32058920713030     -0.24951214205396
  C    2.15481954484468     -2.74124003107267     -0.54755801141332
  H    3.72657716044950      2.66548352482349      0.02336248783416
  H    3.58241635661593      2.21093323137639      1.71188485948143
  H    3.83732394765963     -0.74322831424742     -0.04101998524826
  H    1.79056377288556     -2.98958315798313     -1.54279992246183
  H    1.64084405323577     -3.38834821072420      0.16002698518022
  H    3.22295916755522     -2.91611761132156     -0.49562553276841
  Co  -0.11714919495196      0.57824540939540     -0.07682892561461
  O   -0.51438980314644      0.38641916483253      1.74682848409753
  N    0.26647537312114      1.11604619523125     -1.85161417846297
  N   -0.19687135905468      0.47268844323193     -2.74655468034969
  N   -0.60851134914602     -0.10650070638970     -3.63108839697697
  H    4.67425350172104      1.29988191229582      0.64732206582770
  C   -2.59447826464784     -0.67741136210299      0.07904756220211
  C   -2.43117501973853     -0.94230078431299      1.43098644934691
  C   -1.44048304560945     -0.34803910564317      2.20451926907694
  C   -1.43648785013208     -0.53168816434576      3.68286599205943
  C   -3.78798564927423     -1.18997764459335     -0.64888161337040
  H   -0.49954339863098     -1.00039057245009      3.97893776292903
  H   -2.26964050392706     -1.13851755803676      4.01827618166283
  H   -1.47744630656279      0.44378383155871      4.16373190471305
  H   -3.16740710068915     -1.55335280075108      1.92386663181906
  H   -3.45729548402673     -1.79660159340988     -1.48993226379176
  H   -4.34441712835713     -0.34767622527876     -1.05635923791087
  H   -4.43502803331007     -1.77473979571582     -0.00536003544364
```

C.2. $Ni(dppe)_2(N_3)_2$

C.2.1. $Ni(dppe)_2(N_3)_2$ (S = 0)

Geometry Optimization

```
! def2-TZVPP def2/J RIJCOSX VeryTightSCF VeryTightOpt Freq defgrid3

%pal
nprocs 8
end

%maxcore 3000

%method
method dft
functional HYB_GGA_XC_WB97X_D
end

%scf
MaxIter 500
end

%cpcm
epsilon 8.93
end

* xyzfile 0 1 nidppe_pbe0.xyz
```

Optimized Geometry

```
59
Coordinates from ORCA-job Ni-dppe-N3_2_wB97XD
  Ni   4.23417482181654     10.69268210333490      8.48230380278527
  P    2.29893698965522     11.64250940216432      8.93596140122792
  P    4.36246980693796     12.09866824490064      6.78415253308013
  N    4.13719514562748      9.43485243531852      9.92004997946042
  N    3.55980682669500      9.42155717395160     10.95938873347058
  N    3.04504053867016      9.34570895116483     11.97753870882018
  N    5.94279604043031      9.99018529253978      7.90521975895065
  N    6.45139911769014      9.04346447036611      8.42194890809223
  N    6.98261037844865      8.14407335790005      8.88013156339195
  C    1.80026944281196     12.66039655308898      7.49176001052368
  H    1.38973910239451     11.97916477526726      6.74467790092347
  H    1.01611380027172     13.36508629534255      7.76449620303120
  C    3.04493697020754     13.36364531256668      6.95951591708475
  H    3.39752051251781     14.11241642123663      7.67000648453680
  H    2.85529870177317     13.86764812059965      6.01332566795761
  C    0.91476397526788     10.50483338192280      9.23186712384377
  C    0.17763149888056     10.49636670791414     10.41181298581386
  H    0.40832810502998     11.19086420938825     11.20742473527633
  C   -0.85885933597550      9.58803749437634     10.57941132682095
  H   -1.42540396224624      9.58916524909294     11.50113956218813
  C   -1.16286588544065      8.68303460339670      9.57508370920773
  H   -1.97073108377884      7.97559173779857      9.70893668288829
  C   -0.42405545307290      8.67939803706526      8.39867115774643
  H   -0.65151852007561      7.96930881129349      7.61472701671280
  C    0.61225692195632      9.58110369814555      8.22898528892747
  H    1.19173223004222      9.55930751849030      7.31341064815422
  C    2.38720198083586     12.80201780934657     10.32922923203363
  C    3.53586827879696     12.84344311301590     11.11571385516538
  H    4.36161536964043     12.17519686757848     10.90478983684435
  C    3.63202764657845     13.74224985890577     12.16862921753172
  H    4.52880637105400     13.76569878442338     12.77321073038705
  C    2.58258955410766     14.60546664263994     12.44116367219603
  H    2.65760336422070     15.30696348008193     13.26178001987665
  C    1.43406027104571     14.57204146432240     11.66035942359777
  H    0.61345349062854     15.24498796257429     11.87083877694220
  C    1.33539065131230     13.67647652533243     10.60897471964823
  H    0.43318212763347     13.65959132996186     10.01064467847019
```

C	5.92769364214062	13.00564901118268	6.64125890126327
C	6.83083706195479	12.76230120327469	5.61064092395865
H	6.59715266392273	12.04292477747035	4.83765573331911
C	8.04067746503897	13.44066889482332	5.56841501839069
H	8.73491187147698	13.24502989142037	4.76188620036664
C	8.35874053801826	14.36203963886319	6.55439462187152
H	9.30232996883703	14.89058928210528	6.51877695409784
C	7.46685115209978	14.60095735773431	7.59141519542220
H	7.71297471269750	15.31270375833339	8.36824923305766
C	6.26019081236451	13.92255908618342	7.63922992743647
H	5.58259867769240	14.10652964396148	8.46409542094257
C	4.04627918004209	11.30631079377448	5.18108815394732
C	3.95066965329558	9.91980529999130	5.09769546898784
H	4.09440697190855	9.31587375704969	5.98397650581704
C	3.68115817908624	9.30934845654721	3.88044342209657
H	3.60813684854879	8.23128581024706	3.82604422452479
C	3.50745182782724	10.07920730339876	2.74105998452066
H	3.29721987473218	9.60304177792745	1.79222811537944
C	3.60417022132279	11.46319067929744	2.81587763057866
H	3.47156911278153	12.06670584366724	1.92771976565828
C	3.87170215935098	12.07510698219774	4.02883106653027
H	3.95040261247037	13.15442055373707	4.07201255822097

TDDFT Calculation

```
! def2-TZVPP def2/J RIJCOSX TightSCF defgrid3
! MORead
%moinp "orbitals.gbw"

%tddft
nroots 50
triplets True
end

%pal
nprocs 8
end

%maxcore 3000

%method
method dft
functional HYB_GGA_XC_WB97X_D
end

%scf
MaxIter 100
end

%cpcm
epsilon 8.93
end

* xyzfile 0 1 Ni-dppe-N3_2_wB97XD.xyz
```

C.2.2. $Ni(dppe)_2(N_3)_2$ (S = 1)

Geometry Optimization

```
! UKS def2-TZVPP def2/J RIJCOSX VeryTightSCF VeryTightOpt Freq defgrid3
! MORead
%moinp "old_orbitals.gbw"

%pal
nprocs 8
end

%maxcore 3500

%method
method dft
functional HYB_GGA_XC_WB97X_D
end

%cpcm
epsilon 8.93
end

* xyzfile 0 3 start.xyz
```

Optimized Geometry

```
59
Coordinates from ORCA-job nidppen32_S1_wb97x-d_def2TZVPP
  Ni  -0.26855330307085      0.04001261233556     -1.34523051698324
  P    0.67565694685382      1.41771659353734      0.31207681920078
  P   -0.89200879751960     -1.42392857240415      0.38165801219473
  N    0.98394241224764     -0.54708644672915     -2.68746420250531
  N    2.12248402262628     -0.77571333642368     -2.92313639479870
  N    3.20964954241513     -1.01102546616868     -3.18619255438164
  N   -1.97840730889893      0.87231898250221     -1.80384421712414
  N   -2.80901105566103      1.46619786479412     -1.20017500406774
  N   -3.63220078379213      2.04418949851093     -0.65426159788380
  C    0.40369486736358      0.49502458886349      1.87781726620907
  C   -0.90045093334152     -0.30579856509326      1.83925891668855
  H    0.43450537696456      1.16085689344494      2.73884409047639
  H    1.25910926852628     -0.17668623076155      1.97329587184664
  H   -1.75735504410125      0.36184216320218      1.73466951304385
  H   -1.03617748321886     -0.87190273345842      2.76020274099830
  C    2.45974196295239      1.77360718050802      0.30083479487259
  C    2.97678729818172      3.03857431032844      0.56683113582573
  C    4.34868502874967      3.24813264892708      0.55244032723332
  C    5.21251758743968      2.19913851523397      0.27568201365653
  C    4.70331108403366      0.93517982368562      0.00963786572856
  C    3.33419692372367      0.72429093792069      0.01662921661150
  H    2.31394829513058      3.86526632092812      0.78467888789292
  H    4.74081814980932      4.23531180399314      0.75904093885939
  H    6.28167080599213      2.36599167721022      0.26343860779975
  H    5.37135310728367      0.11360113834495     -0.21258233061059
  H    2.94573363012096     -0.26365311155477     -0.20121578725672
  C    0.26370114905772     -2.75690462841148      0.81880123609151
  C    0.17165720340857     -3.42573076277829      2.04083541529762
  C    1.06608332900886     -4.43546218757410      2.35265633656907
  C    2.05893937217412     -4.79094140166086      1.44713725184570
  C    2.15353831743589     -4.13614971433142      0.22962981083292
  C    1.25888864438565     -3.12113625262433     -0.08358043639681
  H   -0.60349158264810     -3.16501080517442      2.75061085522449
  H    0.98809158263578     -4.94814696738535      3.30234085510394
  H    2.75683316698619     -5.58061161167957      1.69333346767196
  H    2.92279019130107     -4.41119563630632     -0.47969640262723
  H    1.33278829198705     -2.61233209468696     -1.03587775038758
```

C	-2.53498971807071	-2.20236686066176	0.32364734574154
C	-3.68505114170802	-1.43792960942466	0.52007723173326
C	-4.93911505578916	-2.01789920877762	0.40715502516719
C	-5.06075271178472	-3.36234769495918	0.08612355151025
C	-3.92169807300739	-4.12573859074795	-0.12303389684026
C	-2.66526080239467	-3.55053136753350	-0.00642801408821
H	-3.61627248864473	-0.38478522020589	0.75965644521063
H	-5.82245570282409	-1.41402502282427	0.56803870483303
H	-6.04061880822056	-3.81279658002944	-0.00284089281443
H	-4.00781180156877	-5.17406946601139	-0.37705293687819
H	-1.78618796885421	-4.15946436606908	-0.17142850686860
C	-0.15517805112124	3.02538529779042	0.45341791559368
C	-0.64030012384260	3.54263257365618	1.65138015664991
C	-1.26430129375162	4.78241081035862	1.67569524277409
C	-1.40231969470776	5.51686627325205	0.50806631221457
C	-0.92067998872489	5.00810198287470	-0.69080846388685
C	-0.30743025888397	3.76681096417487	-0.71946355673622
H	-0.53991110304626	2.99048229805315	2.57576712627811
H	-1.64187661412072	5.17233336870554	2.61170155980189
H	-1.88947798605970	6.48288762778404	0.52985689125876
H	-1.03061258627750	5.57404900313931	-1.60631148613287
H	0.05205470685993	3.36930675839161	-1.66113080727366

C.2.3. $Ni(dppe)_2(N_3)(N)$ ($S = 0$)

Geometry Optimization

```
! def2-TZVPP def2/J RIJCOSX VeryTightSCF VeryTightOpt Freq defgrid3
! MORead
%moinp "old_orbitals.gbw"

%pal
nprocs 8
end

%maxcore 3000

%scf
MaxIter 1000
end

%method
method dft
functional HYB_GGA_XC_WB97X_D
end

%cpcm
epsilon 8.93
end

* xyzfile 0 1 start.xyz
```

Optimized Geometry

```
57
Coordinates from ORCA-job nidppe-n3-n_S0_wb97xd-def2TZVPP
  Ni   0.02552435746094     -0.48244849466233     -1.74694716504688
  P   -0.49357559390277      1.83587202345904      0.16024965390353
  P    0.46490115419856     -1.41302189256609      0.11920257542528
  N    0.03721993208233      1.19052748922506     -1.16161553044019
  N   -0.03939651856163     -1.84765620868555     -3.02838502292216
  N    0.03128509209322     -3.03047642062930     -3.08649000571023
  N    0.09082070495118     -4.16622804812532     -3.20385896881058
  C    0.05200120818952      0.92600419805449      1.64968519896388
  H    1.12930203656628      1.07537848233733      1.74060100779604
  H   -0.41077885806283      1.35861639260052      2.53707300797435
  C   -0.28433260737188     -0.55951727262266      1.55793819700944
  H   -1.36276183018236     -0.70826475523201      1.47682350833853
  H    0.03841982660610     -1.07849456195585      2.46129618138508
  C    0.13052914009638      3.53073797216307      0.35709306318543
  C   -0.69834866121334      4.64844423982299      0.33421871203158
  H   -1.76911816181358      4.53161858811002      0.23669096961668
  C   -0.15936401053480      5.92476592259095      0.42846286936148
  H   -0.81420427337709      6.78595976493804      0.40572823631764
  C    1.21098173704133      6.09413423975952      0.54909562592589
  H    1.63002481440467      7.08914982113964      0.62466931860331
  C    2.04659254078353      4.98450317824944      0.56767160236218
  H    3.11754037579090      5.11162755243776      0.65636387422797
  C    1.51051302781811      3.71160062959600      0.46690029100906
  H    2.17282096455554      2.85469507839821      0.46328029244688
  C   -2.30833771785104      1.94389834996921      0.35078249114506
  C   -3.10856201035463      1.55480963122593     -0.71805683876385
  H   -2.63865136377060      1.21807717070595     -1.63373691101514
  C   -4.49272271464363      1.59207860684905     -0.61307000242094
  H   -5.10495995737371      1.28669199151718     -1.45155324213189
  C   -5.08660183181845      2.01731367992603      0.56528674200787
  H   -6.16527574846962      2.04487655331555      0.65021331020072
  C   -4.29567691347833      2.40788850531298      1.63904792361758
  H   -4.75629037536955      2.74061883305938      2.56008028511187
  C   -2.91465102266023      2.37239030358710      1.53261699004157
  H   -2.31182550568928      2.68749500424483      2.37566987042444
  C   -0.16051189427582     -3.11489009080076      0.26990828566712
  C    0.67196611845950     -4.21040348376947      0.47615412656382
```

H	1.74164242389468	-4.07705848298807	0.56188067950400
C	0.13514082955087	-5.48765539336682	0.56987735104276
H	0.79195858923368	-6.33253321137155	0.72950959255614
C	-1.23238564009425	-5.67975178134941	0.45556108384941
H	-1.64824292418081	-6.67618894283311	0.52747071698952
C	-2.06799004543855	-4.59172848171619	0.23776494955585
H	-3.13550993614322	-4.73653533727211	0.13717994996131
C	-1.53569559743395	-3.31740202055855	0.13975674848879
H	-2.19540998772756	-2.47858352548865	-0.04822719415149
C	2.24918322462813	-1.47008141749719	0.45636916216000
C	3.14689833522666	-1.20207376320509	-0.57411077911556
H	2.77606537724662	-0.96078995528225	-1.56244219949718
C	4.51421546509533	-1.23764377088061	-0.34124011393119
H	5.20157580393926	-1.02788797003012	-1.14993325679109
C	4.99438533345335	-1.53619311387652	0.92457573451312
H	6.06067341752165	-1.55999166030361	1.10798572727691
C	4.10640884005168	-1.80373140629719	1.95834576720297
H	4.47752961047360	-2.03796201477147	2.94732184052443
C	2.74090895445128	-1.77321512537473	1.72688862660108
H	2.06272874829222	-1.99265300368254	2.54156270336157

C.2.4. $Ni(dppe)_2(N_3)(N)$ $(S = 1)$

Geometry Optimization

```
! UKS def2-TZVPP def2/J RIJCOSX VeryTightSCF VeryTightOpt Freq defgrid3
! MORead
%moinp "old_orbitals.gbw"

%pal
nprocs 8
end

%maxcore 3500

%scf
MaxIter 1000
end

%method
method dft
functional HYB_GGA_XC_WB97X_D
end

%cpcm
epsilon 8.93
end

* xyzfile 0 3 start.xyz
```

Optimized Geometry

```
57
Coordinates from ORCA-job nidppe-n3-n_S1_wb97xd-def2TZVPP
  Ni  0.13966032898992     -0.11512282441844     -1.26073802647339
  P   0.89361302762645      1.43835484519672      0.22630639582895
  P   -0.67339763903297     -1.58623155730839      0.31032098381943
  N   1.65966010578090     -0.81483421438986     -1.16929679688637
  N   -1.38284829269750      0.50560924261599     -2.24145403409784
  N   -2.35937677953196      1.16782366476079     -2.18813631441341
  N   -3.32062968588006      1.79283889670258     -2.17974584422720
  C   0.77664493151300      0.38486631678962      1.73159228071239
  C   -0.50362579692276     -0.45975755846968      1.76440941838122
  H   0.85199944351180      0.99051208948561      2.63420407978423
  H   1.65673630954417     -0.25984734681079      1.71148970310879
  H   -1.38326870770954      0.18591787224209      1.74981633360761
  H   -0.55263164832674     -1.02872234378124      2.69207962987285
  C   2.58933643551648      2.10631473002971      0.27580615985606
  C   2.83345661027329      3.47799051761523      0.24837055125102
  C   4.13449471530780      3.96087032314787      0.25840849537776
  C   5.20565484411532      3.08183523071417      0.29826912816743
  C   4.97131888050914      1.71377910207382      0.32317585365040
  C   3.67399732311869      1.22729405180737      0.30674025761493
  H   2.01078718065888      4.17931178798994      0.22141117308611
  H   4.30688464644488      5.02902698582905      0.23791431455330
  H   6.21959338842799      3.45991039049176      0.30827270632134
  H   5.80141975988355      1.02010389282233      0.35108450381889
  H   3.50907154619433      0.15813583723978      0.30748684747448
  C   0.23810597855551     -3.10675367464528      0.71081837669721
  C   0.31631124972464     -3.61792726034588      2.00575867739270
  C   0.99563757341027     -4.80104990976841      2.25226775805821
  C   1.59546259103061     -5.49082349591148      1.20749483097357
  C   1.51566629736536     -4.99433369513257     -0.08509199188563
  C   0.84438119366517     -3.80576984001501     -0.33158619672865
  H   -0.15775080303184     -3.10407947915433      2.83154631963627
  H   1.05256423834932     -5.18615290237515      3.26191262031676
  H   2.12462709924310     -6.41465611004767      1.40201296111403
  H   1.98092042977898     -5.52789506208466     -0.90337354224870
  H   0.79508607017672     -3.41440726496630     -1.33923526909498
  C   -2.43357496771009     -2.05940714918140      0.33469482694472
  C   -3.40179469704264     -1.05697031796368      0.24957996499347
```

C	-4.74825325642737	-1.38042077698158	0.21664788511683
C	-5.14723466561945	-2.70984908035798	0.25538441736199
C	-4.19207771373918	-3.71194986869239	0.32796396210028
C	-2.84221780961145	-3.39070818967500	0.36646071590286
H	-3.11059532857038	-0.01470460788213	0.20558300198765
H	-5.48621789937525	-0.59147856773135	0.15401330354594
H	-6.19916884013816	-2.96212477030523	0.22618256015727
H	-4.49427710573155	-4.75072866703028	0.35658892536997
H	-2.11061680499686	-4.18523850153804	0.42371631670287
C	-0.18967503620084	2.87321525557078	0.50489639576902
C	-0.51724601455873	3.34312920823984	1.77629954211806
C	-1.32052618165500	4.46360274454353	1.92275816711079
C	-1.79672229600419	5.13186650530169	0.80317860833750
C	-1.47237993506749	4.67429033215519	-0.46523960587526
C	-0.67956276283694	3.54605129576778	-0.61340194012993
H	-0.14573991121654	2.84600127140464	2.66211172109202
H	-1.57161647809910	4.81656200778101	2.91441095764756
H	-2.42276079366995	6.00680388680874	0.92049495933360
H	-1.84407328687883	5.18806421388807	-1.34176643555489
H	-0.43870106043285	3.18519153794848	-1.60563359445209